Precursors of Prebiotic Molecules

from laboratory to space

Davide Alberton

München 2024

Precursors of Prebiotic Molecules
from laboratory to space

Davide Alberton

Dissertation
der Fakultät für Physik
der Ludwig-Maximilians-Universität
München

vorgelegt von
Davide Alberton
aus Cassola, Italien

München, den 29.02.2024

Erstgutachter: Prof. Dr. Paola Caselli
Zweitgutachter: Prof. Dr. Dieter Braun
Tag der mündlichen Prüfung: 12.04.2024

I have found that I always learn more from my mistakes than from my successes.
If you aren't making some mistakes, you aren't taking enough chances.

- John Sculley

Contents

List of Figures

List of Tables

Zusammenfassung

Der Himmel hat uns schon immer fasziniert, aber erst in jüngster Zeit hat der technische Fortschritt es uns ermöglicht, ihn genauer zu untersuchen. Im Laufe der Zeit haben wir die Vielfalt der Gebiete entdeckt, die er enthält, und insbesondere die Untersuchung der Sternentstehungsgebiete führt uns zu einem besseren Verständnis der Entstehung von Sternen und Planeten. So entstanden neue wissenschaftliche Disziplinen wie die Astrochemie und die Astrobiologie, die verstehen zu versuchen, wie sich die chemische Komplexität entwickelt hat und wie sie genutzt werden kann, um die Stadien der Sternentstehung nachzuvollziehen, und wie diese chemische Vielfalt schließlich zur Entstehung von Leben geführt hat.

In dieser Arbeit befassen wir uns mit den Wiegen der Sternentstehung, den Molekülwolken, und damit, wie sie im Laufe der Zeit mit den Bestandteilen angereichert wurden, die letztendlich zur Entstehung von Leben geführt haben könnten. Dies ist immer noch ein sehr umstrittenes und kontroverses Thema, aber die Astrochemie hilft uns, die physikalischen und chemischen Prozesse zu verstehen, die in solchen Gebieten Umgebungen ablaufen. Insbesondere die Rotationsspektroskopie bietet sich als unersetzliche Ergänzung zu diesem Verständnis an, da sie Beobachtungen mit genauen und zuverlässigen Informationen für die Suche nach präbiotischen Molekülen im Weltraum versorgt.

Nach einer anfänglichen Einführung in die theoretischen und experimentellen Konzepte, die dieser Arbeit zugrunde liegen, werden in den ersten beiden Kapiteln dieser Arbeit die Ergebnisse der hochauflösenden spektroskopischen Laboruntersuchung von Allylimin (CH_2=CHCH=NH) und Aminoacrylnitril (3-Amino-2- propennitril, H_2NCH=CHC≡N) vorgestellt, zwei vielversprechenden Imin- beziehungsweise. Cyanidkandidaten für die Bildung von Aminosäuren im Weltraum. Die experimentelle Charakterisierung der Rotationsspektren und die Erstellung sehr präziser Ruhefrequenzkataloge für die beiden Moleküle ermöglichten die Durchführung einer Spektrallinienuntersuchung in der Molekülwolke G+0,693-0,027 im galaktischen Zentrum, die zu einem vorläufigen Nachweis von Allylimin und zu einer oberen Grenzhäufigkeit von Aminoacrylnitril führte.

Der letzte Teil ist eine theoretische Studie von NH_2CHCO, einem Iminoacetaldehyd-Molekül, das als Schlüsselschritt bei der Bildung des kürzlich entdeckten Ethanolamins ($NH_2CH_2CH_2OH$) vorgeschlagen wird, das in den Phospholipiden biologischer Zellen vorhanden ist. Mit modernsten quantenchemischen Berechnungen untersuchen wir die relativen Energien seiner Isomere, identifizieren die energetisch günstigsten und erhalten ihre Rotations- und Dehnungskonstanten, um ihre Suche im Labor und im Weltraum zu erleichtern.

Abstract

We have always been fascinated by the sky, but it is only recently that technological advances have allowed us to study it in greater depth. Over time we have discovered the variety of environments it contains, and in particular the study of stellar formation regions is leading us to understand how stars and planets are formed. But while some questions have been answered, many more have been raised, leading to new scientific disciplines such as astrochemistry and astrobiology, which seek to understand how chemical complexity evolved and how it can be used to trace the stages of star formation, and how this chemical diversity ultimately led to the emergence of life.

In this thesis, we look at the cradles of star formation, molecular clouds, and how they have been enriched over time with the components that may ultimately have led to the emergence of life. This is still a highly debated and controversial topic, but astrochemistry is helping us to understand the physical and chemical processes that take place in such environments. In particular, rotational spectroscopy offers itself as an irreplaceable companion to this understanding, providing the observational search with accurate and reliable information to search for prebiotic molecules in space.

After an initial introduction to the theoretical and experimental concepts underlying this work, the first two chapters of this thesis present the results of the laboratory high-resolution spectroscopic study of allylimine (CH_2=CHCH=NH) and aminoacrylonitrile (3-amino-2- propenenitrile, H_2NCH=CHC≡N), two promising iminic and cyanide candidates, respectively, for the formation of amino acids in space. The experimental characterisation of the rotational spectra and the creation of very precise rest frequency catalogues for the two molecules allowed to perform a spectral line survey in the G+0.693-0.027 molecular cloud at the Galactic Centre, leading to a preliminary detection of allylimine and to an upper limit abundance of aminoacrylonitrile.

The last part is a theoretical study of NH_2CHCO, an iminoacetaldehyde molecule proposed to be a key step in the formation of the recently detected ethanolamine ($NH_2CH_2CH_2OH$), present in the phospholipids of biological cells. With state-of-the-art quantum chemical calculations, we investigate the relative energies of its isomers, identifying the most energetically favoured ones, and obtain their rotational and distortion constants to aid their search in the laboratory and in space.

Chapter 1

Introduction

1.1 A molecular journey

For abiogenesis (from the Greek α- a- 'not' + $\beta\acute{\iota}o\varsigma$ bios 'life' + $\gamma\acute{\varepsilon}\nu\varepsilon\sigma\iota\varsigma$ genesis 'origin') we mean the process by which life emerged from non-living matter. The Greek philosopher Empedocles (~ 494-434 BC) long ago distinguished the concept of *life* from that of *non-life*, and after him Democritus (~ 460-370 BC), who introduced the idea of *atomism*, opened the way to the consequent theory of *materialism* (Decartes, 1596-1650) and its implications for the animal machinary. The idea of self generation though, was first tackled by Aristotle (~ 384-322 BC), and his concept of *spontaneous generation*. In the Middle Ages, this gave rise to the idea of the infusion of *vital heat* into *abiotic* material, an idea that only died when Louis Pasteur (1822-1895) demonstrated in his famous experiment that spontaneous generation did not actually take place. But while his experiment undoubtedly disproved continuous generation on Earth, it was not enough to disprove the idea that it must have happened once.

Today, the concept of life fulfils a number of requirements, namely the capacity for homeostasis, organisation, metabolism, growth, adaptation, response to stimuli and reproduction. NASA fellow Gerald Joyce defined it as "a self-sustaining chemical system capable of Darwinian evolution", implying the need for an interdisciplinary approach. Among the various branches of science working on this topic, geneticists have added another piece to the puzzle, identifying in LUCA the Last Universal Common Ancestor. This progenitor could have been the last unicellular entity to share the same minimum number of genes to be defined as an organism. Since it lived about 4 billion years ago, it should have had the same identical genetic traits that are now shared by bacteria, archaea and eukaryotes, the three domains to which living organisms belong.

LUCA had to have a cellular machinery capable of sustaining the above requirements, which can be summarised as self-replication, self-assembly and autocatalysis. These functions are carried out by four main classes of molecules: lipids, proteins (i.e. amino acids), nucleic acids (RNA and DNA) and sugars. These are the molecular pillars of every living cell, from you to the sponges on the volcanic cones of the Atlantic Ocean. So how are these molecules made?

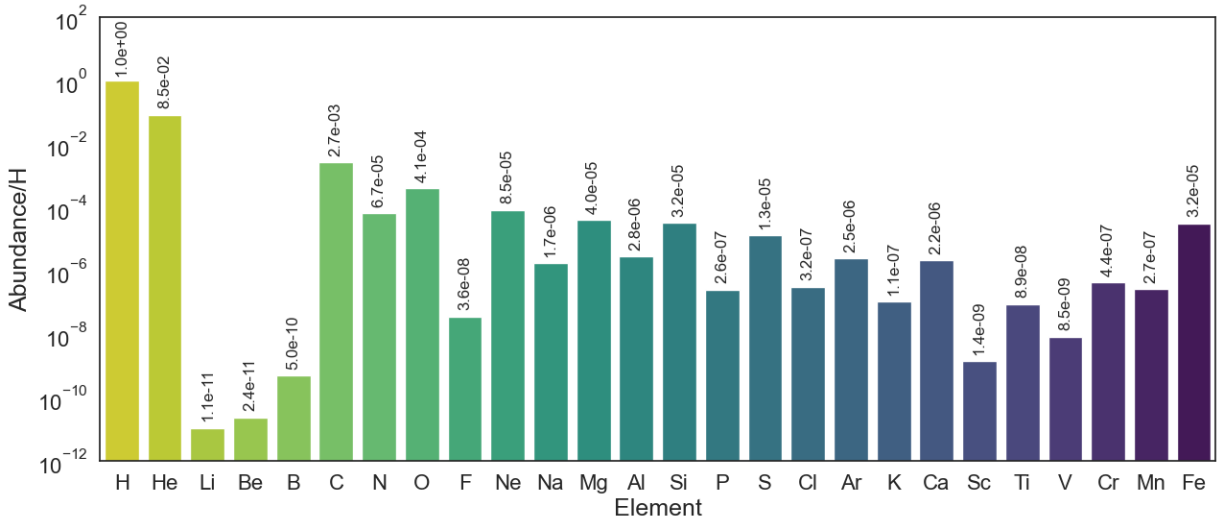

Figure 1.1: Cosmic element abundances relative to H.

From the ink on this page to the retina of an eye, matter is made up of atoms. Millennia have passed to agree with Democritus [1] and billions of years have passed to return to the first moments of the process of their formation. Every molecule is made up of atoms that were created as a byproduct of the Big Bang in a process known as nucleosynthesis. According to this widely accepted theory, primordial nucleons were formed when a quark-gluon plasma cooled to a temperature of the order of trillions of degrees Kelvin some 13.8 billion years ago. Hydrogen, helium, lithium and beryllium were mainly produced, leaving the stars to synthesise the remaining elements through to iron. Instead, the heavier elements were produced in the final moments of life of supermassive stars which, exploding, bridged the energy gap that self-sustaining fusion could not.

But it was a long time before space gave birth to the first molecule. The ions of the light elements, such as hydrogen, helium, deuterium and traces of lithium, recombined when the universe was below ~3000 K. At this temperature, the mean free path of a photon was much smaller than the horizon size of the universe, about $3x10^5$ years after the Big Bang. After its formation, helium first combined with three electrons, causing it to take an additional proton from the ionised medium by radiative association, forming the first molecule of the Universe, HeH^+, recently detected under different conditions (Güsten et al. 2019). As a consequence, the reaction of this molecule with neutral hydrogen led to the formation of molecular hydrogen and the beginning of the modern universe with its physics and chemistry.

Molecules now permeate the Universe, from diffuse and dense clouds in the Interstellar Medium (ISM) to the atmospheres of cool stars; from Hot Cores and Hot Corinos to Protoplanetary Disks. Molecules are ubiquitous, and a great deal of information can be derived from where they are found (Tielens 2021).

[1] The idea of atoms did not actually originate with Democritus. Some believe that it was suggested by Leucippus, but it is generally believed that the concept arose from a dialogue between the student and the master.

When we talk about molecules in space, we have to start with H_2. This molecule has played and continues to play a central role in our understanding of the Universe. Depending on its state of ionisation, it allows us to trace the evolution of spiral galaxies (HI) to massive stars (HII), forming the reservoir that will eventually give rise to molecular clouds and, consequently, planets. First predicted by Van de Hulst in 1944 and directly observed in 1951 by E. M. Purcell and his student H. E. Ewen, the HI transition at 21.1 cm has allowed us to better understand our own and other galaxies. Although this transition is not very intense, the amount of hydrogen present overcomes this inconvenience: of the approximately 5% of the baryonic mass[2] of the Universe, 75% is hydrogen. Helium makes up about 24%, and all the heavier elements make up between 1 and 2%. In our Galaxy, 90% of the baryonic mass is in stars, while the rest is in the ISM, i.e. the material between stars. Since the total mass of the Milky Way is 10^{11} $M_\odot$ [3], the mass of the ISM is 10^{10} $M_\odot$ and consists of gas and dust (Yamamoto 2017). The dust is composed of silicates and carbonaceous compounds with diameters of ~ 0.01 μm and an average mass ratio of 0.01 with respect to the gaseous counterpart[4]. The cosmic abundances of the elements in Figure 1.1 show that, after hydrogen and helium, the most abundant elements are carbon, oxygen and nitrogen. Excluding the noble gases, the same is true for sulphur, iron, magnesium and silicon, but since heavier elements tend to be refractory, these elements are mostly found in dust grains.

1.2 The ISM

The ISM is not a homogeneous environment, but is made up of different heterogeneous phases, mainly as a consequence of temperature and density. It is therefore necessary to imagine the ISM as a dynamic coexistence of distinct phases where different chemical and physical phenomena occur. In this section we will try to give a brief introduction on how these elements influence this environment. Table 1.1 attempts to cover all ISM phases, which vary enormously in thermal and ionisation complexity.

Before commenting on the various stages of Table 1.1, it is useful to clarify that temperature is nothing more than the result of thermal processes in the gaseous phase, which are mainly caused by the following factors

- Heating: Depending on the environmental conditions, atoms or molecules usually absorb photons and eject electrons that thermalise their kinetic energy through elastic collisions. In the diffuse ISM this is mostly due to photoionisation from UV, X and cosmic rays of gas and dust. Note that there are about 100 more electrons from dust than from gas, a factor of primary importance for the subsequent formation of molecules. The *thermalisation timescale* is the time required for this kinetic energy to be redistributed to the environment until equilibrium is reached.

[2] A baryon is a non-elementary subatomic particle composed of quarks (usually three). Baryons belong to the Hadron family, participate in the strong interaction and make up most of the mass of visible matter in the universe.

[3] $M_\odot$ stays for *solar mass*. $1M_\odot = 1,989 \times 10^{30}$ kg.

[4] Metallicity influences the density and hence the dust-to-gas mass ratio.

- Cooling: This is mainly due to collisional de-excitation between small masses such as protons and electrons and heavier bodies, and can result in fine structure, electron recombination, resonance and masers, for example.

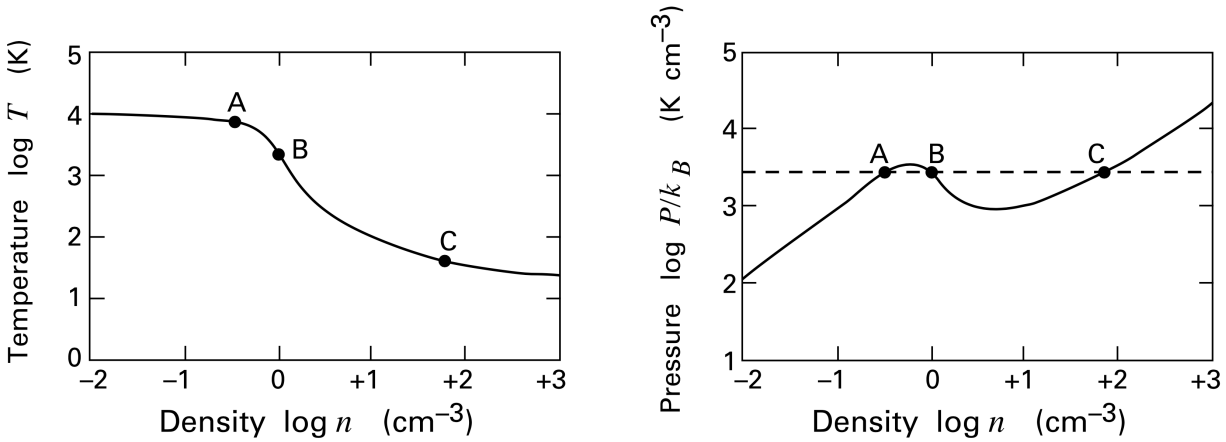

Figure 1.2: (left) Theoretical prediction for the equilibrium temperature of interstellar gas, displayed as a function of the number density n. (Right) Equilibrium pressure nT as a function of number density. The horizontal dashed line indicates the empirical nT-value for the interstellar medium.

Roughly speaking, equilibrium is reached at constant volume when the heating rate equals the cooling rate. This allows us, assuming there is one, to calculate the equilibrium temperature of a gas as a function of its density.

Figure 1.2 shows this trend for a cold neutral and a warm neutral cloud, the parameters of which are briefly summarised in Table 1.1. In the left panel we see how an increase in density leads to a decrease in temperature mainly due to CII emission at 158 μm. Conversely, for the same heating yield but higher densities, the temperature increase is balanced by H's Lyα emission. Multiplying the same curve by n gives the one in the right panel, showing that there are indeed multiple equilibria. Assuming a thermal pressure equilibrium with non-thermal contributions such as magnetic fields, if a packet of gas is compressed at point B, it will cool until it reaches the state of a cold neutral medium (point C). On the other hand, if it expands, it will heat up until it enters the warm neutral medium regime (point A). Figure 1.2 uses cold and warm neutral media as examples, but we can now look at the phases in the Table 1.1 in more detail.

Starting at the bottom of Table 1.1, HII regions owe their name to the large ionisation generated by UV radiation coming from massive stars. These systems vary enormously in size, ranging from so-called *ultra-compact* HII (UCHII) and *ultra-dense* HII (UDHII) regions to giant HII regions. These range in size from less than a light-year to several hundreds light-years across, respectively (Anderson et al. 2009), with densities ranging from over a million to just a few particles per cm^3 in the ultra-compact HII regions and the largest and most extended regions, respectively. As a result, an HII region can contain several thousand stars, making the description of these environments more difficult than the single central ionising source of planetary nebulae.

Table 1.1: Phases of the ISM

Phase	n [cm^{-3}]	T [K]	M [$10^9 M_\odot$]	ISM volume fraction	Pressure [$\sim$ nT]
molecular	>300	10	2	0.01	3000
cold neutral	50	80	3	0.04	4000
warm neutral	0.5	8x10^3	4	0.3	4000
warm ionised	0.3	8x10^3	1	0.15	2400
hot ionised	3x10^{-3}	5x10^5	tiny	0.5	1800
HII regions	1-10^6	10^5	tiny	tiny	10^5-10^{11}

The hot ionised medium (Table 1.1), identified by UV spectral lines of highly ionised heavy elements (i.e. OVI, OVII, OVIII), is the only clue to the likely expansion of bubbles produced by supernovae explosions (McKee & Ostriker 1977). Hot ionised phases can also be caused by the birth of massive stars, as in NGC 604 (Tüllmann et al. 2008), and they occupy half the volume of the ISM, with temperatures on the order of millions of K and densities of < 0.003 particles per cm^3. Such bubbles, described by the three-phase model introduced by Field et al. 1969, would have two inner layers which, approaching the centre, are formed by the warm ionised medium (WIM) and the warm neutral medium (WNM). The WIM is characterised by temperatures between 6000 and 12000 K, photo- and collisional ionisation due to shocks and densities of $\sim$ 0.1 particles per cm^3. It contains 90% of the protonated hydrogen in the galaxy and is therefore easily detected by Hα λ = 6563 Å emission. The WNM has a temperature of $\sim$ 8000K and a density of $\sim$ 0.5 particles per cm^3, making up a large volume fraction of the ISM, i.e. 30%. These regions are traced using the HI 21 cm emission line and are also found in the vicinity of molecular clouds, which will be discussed later.

Cooler temperatures in the ISM are found in the Cold Neutral Medium (CNM) and in molecular clouds. CNMs have temperatures that are typically $\sim 80 - 100$ K and densities of $\sim$ 50 particles per cm^3, mostly forming sheets and filaments (up to 4% of the ISM volume) that can feed protostars. These systems are in rough pressure equilibrium with their surroundings and can be detected by a variety of methods, including UV and optical absorption lines. Molecular clouds (the first entry of Table 1.1) can be traced with mm-wavelength molecular radiation and are the coolest and densest regions of the ISM, with values that usually range from 10 to 20 K and typically higher than 300 particles per cm^3, respectively. See the table 1.2 for a more detailed description of the different categories of molecular clouds. These conditions allow for the formation of different chemical species, making it possible to trace the kinetics and dynamics of these environments employing a plethora of molecules as astrochemical tools. Due to these high densities, molecular clouds occupy only $\sim 1 - 5\%$ of ISM volume but almost $\sim$ 30% of its mass, causing these objects to be gravitationally bounded as long as the surrounding environment is not perturbed by astronomical events (such as supernovae explosions) that might disperse or ignite

the collapse of these clouds.

Table 1.2: Molecular clouds

Type	A_V mag	$n_{\rm TOT}$ [cm^{-3}]	L [pc]	T [K]	M [$M_\odot$]
Diffuse	1	30	3	50	50
Giant Molecular Clouds	2	100	50	15	10^5
Dark Clouds					
Complexes	5	500	10	10	10^4
Individual	10	10^3	2	10	30
Dense Cores/Bok Globules	10	10^4	0.1	10	10

1.3 Molecular clouds

Molecular clouds are the cradles of star formation. As mentioned earlier, the fact that these objects account for 30% of the mass of the ISM, condensed into 1-5% of its volume, leads to instabilities that trigger runaway contraction processes. To understand this phenomenon, concepts such as *free fall time* $t_{\rm ff}$, *Jeans mass* $M_{\rm J}$ and *Jeans length* $\lambda_{\rm J}$ are widely used and will be briefly introduced in this section (Stahler & Palla 2004). The collapse of these objects will eventually lead to the formation of planetary systems that will inherit, if not completely at least partially, what has been formed in the previous evolutionary steps. The planetesimals will eventually undergo physical and chemical rearrangement processes that may alter the chemical heritage. Nevertheless, some will be retained and, together with what has been newly formed, will provide the basis for the development of the complexity that we see. The detection of the molecular species formed from these initial stages of molecular complexity throughout the process of planetary system formation provides the narrative link to the physics and chemistry that ultimately led to the emergence of life on Earth.

1.3.1 Gravitational binding energy $\langle U \rangle$

Assuming that the cloud has a spherical symmetry in which viscous effects are negligible, if the density ρ is constant, the infinitesimal element of mass δm at a distance r from the centre of the sphere is given by:

$$\delta m = \rho 4\pi r^2 \delta r \,. \tag{1.1}$$

Since the gravitational force dF experienced by the same element of infinitesimal mass due to the innermost mass M can be expressed by Newton's law of gravitation:

$$dF = -\frac{GM\delta m}{r^2} \,, \tag{1.2}$$

and the infinitesimal work dU required to move the infinitesimal mass element from r to R is given by:

$$U = -\int_{r=0}^{r=R} dF dr \tag{1.3}$$

$$= -\frac{GM\delta m}{r}\,, \tag{1.4}$$

integration over the space interval r to R gives the total gravitational energy U:

$$U = -G\int_{r=0}^{r=R}\left(\frac{4}{3}\pi r^3\rho\right)\left(4\pi r^2\rho\right)\frac{1}{r}\,dr \tag{1.5}$$

$$= -G\frac{16}{3}\pi^2\rho^2\int_{r=0}^{r=R} r^4\,dr \tag{1.6}$$

$$= -G\frac{16}{15}\pi^2\rho^2R^5\,. \tag{1.7}$$

Substituting for ρ we get the gravitational binding energy U:

$$U = -\frac{3}{5}\frac{GM^2}{R}\,, \tag{1.8}$$

which sets the limit that the system's energy must not exceed in order to remain self-bounded.

1.3.2 Jeans' mass and length

To understand the conditions of a self-gravitating system, we can use the *virial theorem*. This is particularly useful for molecular clouds because, unlike the other phases of the ISM, these objects are not in pressure equilibrium with their surroundings. When hydrostatic equilibrium is maintained, the virial theorem relates the time variation of the moment of inertia I to the time-averaged kinetic energy of the system $2\langle T\rangle$ and its time-averaged gravitational potential energy $\langle U\rangle$ as follows:

$$\frac{1}{2}\frac{d^2I}{dt^2} = 2\langle T\rangle + \langle U\rangle\,. \tag{1.9}$$

Assuming a uniform density, if the system is in equilibrium, equation 1.9 must sum to zero:

$$2\langle T\rangle + \langle U\rangle = 0\,. \tag{1.10}$$

As we have seen, the gravitational binding energy U of a gas cloud is often related to its density ρ by the equation 1.1. The Jeans mass M_J, named after the British physicist Sir James Jeans, is the mass of a hydrostatic equilibrium system beyond which it begins to collapse, i.e. the mass that must be exceeded in order to break the equilibrium between the gas pressure and the gravitational force. It can be derived by considering the balance between the gravitational potential energy and the total kinetic energy of the system. The total kinetic energy T is expressed as:

$$\langle T\rangle = \frac{3}{2}Nk_BT\,, \tag{1.11}$$

where N is the total number of particles in the system and is equal to the total mass over the mean mass for the particles, k_B is the Boltzmann constant and T is its temperature. For a stable hydrodynamic equilibrium system such as a cloud, once the mass exceeds M_J, it begins a runaway contraction process that can lead to star formation. Starting from the equation 1.10 at equilibrium, we obtain:

$$\frac{3}{5}\frac{GM^2}{R} = 3Nk_BT\,. \tag{1.12}$$

Solving for M, we have:

$$M > \sqrt{\frac{5Nk_BT}{G}}\,. \tag{1.13}$$

Since:

$$\begin{cases} N &= M/\bar{m} \\ R &= (3M/4\pi\rho)^{1/3}\,, \end{cases} \tag{1.14}$$

where $\bar{m}$ is the mean molecular weight of the particles, after some manipulation it is possible to express the mass the cloud must exceed to start collapsing as:

$$M > \left(\frac{5k_BT}{G}\right)^{3/2}\left(\frac{3}{4\pi\rho}\right)^{1/2}\,. \tag{1.15}$$

Recalling the radius relationship in equation 1.14, it is possible to derive the characteristic dimension of a molecular cloud, known as *Jeans length* R_J:

$$R_J = \sqrt{\left(\frac{15k_B}{4G\pi\bar{m}}\right)\left(\frac{T}{\rho}\right)}\,. \tag{1.16}$$

As the equation 1.15 shows, the colder and denser the cloud, the smaller the Jeans' mass M_J. As a result, cooler clouds are more prone to contraction and, at constant temperature, higher densities speed up the whole process. We can say that for a typical dense core with T $\approx$ 10 K, $n(H)$ = 10^4 cm^{-3} and a chemical composition consisting mostly of molecular hydrogen, M_J is of the order of $5M\odot$. Cooler clouds tend to be denser and smaller, so intuitively the higher the density, the faster the free-fall contraction process. The time it takes for a cloud to collapse is expressed as the *free-fall time* t_{ff}, given by:

$$\tau_{ff} = \left(\frac{3\pi}{32\rho}\right)^{1/2} \tag{1.17}$$

$$\approx \sqrt{\frac{1}{G\rho}}\,, \tag{1.18}$$

The very last equation shows how higher densities lead to faster collapses. The theoretical t_{ff} for giant molecular clouds agrees with the observed lifetimes of $\sim 10^6$ years within an order of magnitude. In fact, the current star formation rate in the Milky Way is 1 $M_\odot$/yr, which is 10 times

lower than that predicted by the t_{ff} of a typical molecular cloud (Robitaille & Whitney 2010). This may be due to the fact that in reality the assumptions made for this derivation are not entirely close to reality. The boundary conditions used to calculate the gravitational potential energy did not take into account that the density is far from homogeneous. Observations have shown that the density does indeed depend on the radius, leading to fractional collapses that give rise to filament and cluster structures. Moreover, the derivation just presented does not take into account all the contributions made by the magnetic field, which further complicates the analysis. Nevertheless, the virial theorem well describes the lifetime of such objects and gives a satisfactory description of the phenomenon. The whole process is nothing more than the result of turbulence, magnetic fields and thermal pressure overcoming the gravitational balance.

1.3.3 Low-mass star formation

The collapse of a molecular cloud occurs when the above M_J of a molecular cloud is exceeded. For clouds with masses below 8 $M_\odot$, the typical low-mass star formation process takes place. For higher masses, the star formation process is slightly different due to shorter timescales and the ignition of hydrogen fusion during the envelope collapse. Although high-mass formation processes are not addressed in this work, the result is usually the formation of binary systems or star clusters.

Figure 1.3 shows the main steps of a low-mass star formation process. The collapse proceeds isothermally as long as the thermal energy produced is dissipated by absorption and re-emission by the grains and by radiative decay or collisional de-excitation, mostly CO mediated. This isothermality is lost as the density of the cloud increases until it becomes optically thick. This causes the temperature of the so-called initial hydrostatic core to rise, remaining stable until it exceeds T $\sim$ 100K and R_J of $\sim$ 5 AU. At this point, H_2 dissociation is triggered, causing a sudden rise in temperature, which in turn leads to the formation of a protostar.

The evolutionary process of a protostar can be monitored using the infrared spectral index α, whose equation is briefly given below:

$$\alpha = \frac{d \log(\lambda S_\lambda)}{d \log \lambda}, \tag{1.19}$$

where S_λ is the flux density at wavelength λ in terms of the relative Spectral Energy Distribution (SED) (Lada 1987). Depending on α, there are four classes[5] of protostars are historically identified (Dunham et al. 2014). Class 0 objects, added later (Andre et al. 1993), are protostars too deeply embedded to be detected in the near-infrared. A protostellar envelope surrounds the central object, absorbing and re-emitting radiation from the infalling material in the far-infrared, revealing outflow structures. Class I objects have $\alpha \geq 0.3$ and are defined as such when the accretion phenomenon of the central object can be considered almost complete. At this stage, a tick circumstellar disc also appears, detectable in the mid-infrared. The latter emits in this spectral region also in Class II objects, where $-1.6 \leq \alpha < -0.3$, but its thinning around the central

[5]To avoid confusion, the use of *Stage* is used when referring to the physical or evolutionary status of an object, and the use of *Class* only when referring to observations Robitaille et al. (2006).

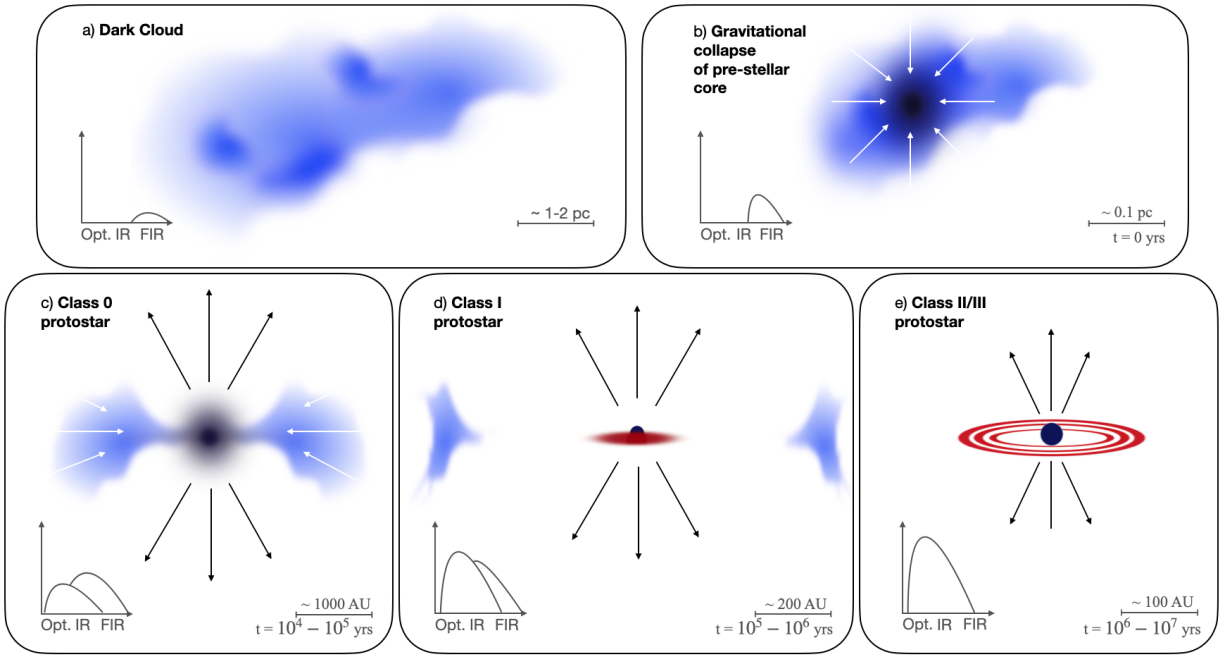

Figure 1.3: Main phases of low-mass star formation.

object proceeds inexorably. The protostar has now entered the pre-main sequence and deuterium fusion makes it visible in the optical. At the same time, only the outer parts of the envelope remain, while the inner parts are almost completely dissipated. The transition between Class 1 and 2 is indicated by the Flat SED phase, whose name refers to the flattening of the SED curve due to increased emission from the stellar object in the optical and decreased emission from the circumstellar disk in the IR. The flattening of the SED curve is observed at $-0.3 \leq \alpha < 0.3$. The final step is represented by Class III objects, which see the star entering the main sequence as hydrogen fusion begins. The star is now surrounded by a debris disk and is indicated by $\alpha < -1.6$.

1.3.4 The chemical evolution

To date, approximately 300 molecules have been detected in the ISM, and this number will inevitably increase (McGuire 2022). Figure 1.4 shows how the rate of molecular detection has increased significantly over time, especially with the introduction of newer telescopes. The detection rate passed from less than 4 molecules per year in the past decades to almost 20 in the last lustre, a five-fold increase. In the last five years, a third of all the molecules observed in space since 1940 was detected, i.e. 100 molecules in 5 years compared to 200 in 80 years.

The discovery of so many molecules has certainly changed the idea that the ISM is an inhospitable environment for chemical complexity. The message about molecular variety that emerges from Figure 1.4 is self-explanatory, but the importance is not limited to the mare number. These molecules have been found in a wide variety of sources of different ages and chemical-physical

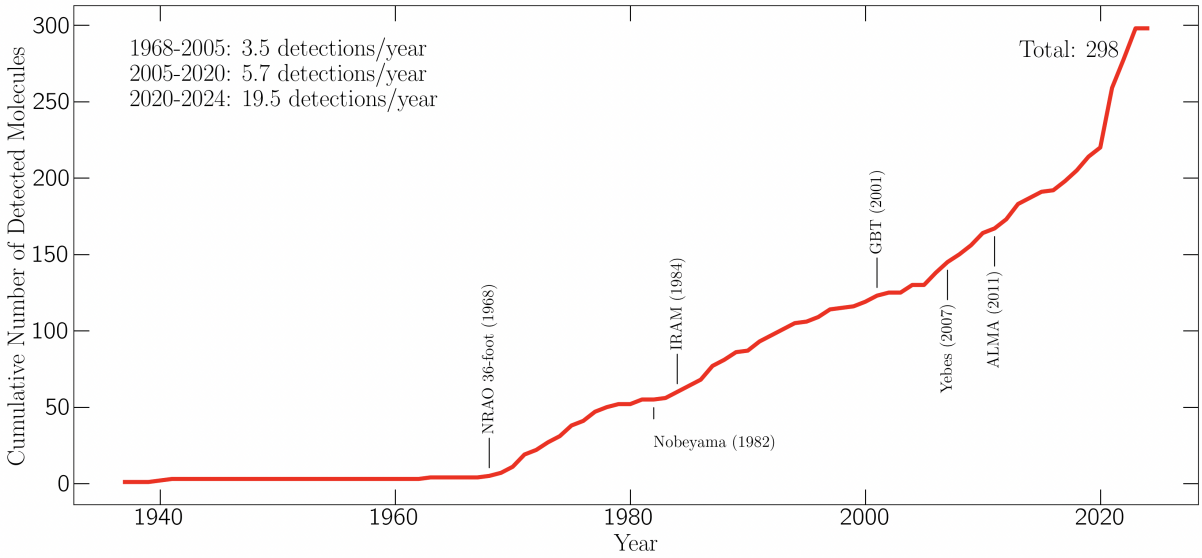

Figure 1.4: Cumulative number of molecules detected in recent years. This figure was obtained using the astromol package by McGuire & mcguiregroup 2021.

properties, shifting their relevance from their detection to their use as diagnostic tools. Information such as temperature, kinetics and dynamics can be derived by using the molecules as thermometers (Crapsi et al. 2007) or their absorption lines as instruments to characterise astronomical objects, like in Pineda et al. 2020. The fact that there are so many molecules available opens the way to a much deeper understanding of the radio universe. The chemical evolution that leads to their formation extends from diffuse molecular clouds to protoplanetary systems, and then on to the planetary scale. But molecular evolution does not follow a straight line: although some molecules are formed during stellar evolution, others are destroyed by antagonistic chemical processes. Molecules are not uniformly distributed in space or time, but their abundances change as interstellar clouds physically evolve into stars and planets. As a result, molecules not only help both astronomers and astrochemists to understand astrophysical objects, but it also helps them to expand their knowledge of the chemical evolution occurring along star formation processes.

Although these processes occur in very different physical stages, we can identify three main drivers of chemical evolution: the conversion of C to CO, the depletion of molecules on dust grains and the evaporation of grain envelopes due to protostar birth. In this section we'll give a brief, simplified general overview of these main aspects.

Figure 1.3 resumes the phases of low-mass star formation. Dark clouds form, as we saw earlier, from diffuse clouds. Here, UV radiation effectively penetrates to the densest layers, easily dissociating atoms and the few molecules that are formed. Carbon atoms are mostly ionised in the C^+ form and the chemistry quickly reaches a steady state as photodissociation blocks chemical evolution. When the free-fall process is initiated, the density increases sufficiently to shield interstellar UV radiation, and C+ ions recombine with electrons to form C atoms and

many new molecules. This vibrancy of molecular production is controlled by the negative feedback of the reaction between carbon and oxygen: the formation of CO, a process that usually takes $10^5 - 10^6$ years, leads to a decrease in carbon reservoirs and a consequent reduction in molecular formation. Nevertheless, the carbon not used in the CO continues to react to form highly stable unsaturated molecules. In contrast, neutral-neutral reactions leading to N_2 take place slowly, paving the way for simple nitrogen-bearing species such as NH_3 and N_2H^+. As the density increases, molecules begin to deplete on gas grains and CO freezes out, further increasing the gaseous abundance of N_2H^+ and prolonging the lifetime of H_3^+ and H_2D^+, leading to strong deuterium fractionation. Molecules depleted on dust grains continue to react, but unlike gas-phase reactions, hydrogenation reactions lead to many saturated organic molecules. Hydrogenation of CO gives HCO, H_2CO, CH_3O and CH_3OH, and hydrogenation of C atoms gives CH, CH_2, CH_3 and CH_4. More complex molecules are also formed by condensation of heavier atoms and molecules, but the kinetics are moderate. Hydrogenation is generally inefficient, but heavy atoms and molecules (radicals) can move along the ice surface to find reaction partners. The result is an increase in the production rate of Complex Organic Molecules (COMs, Herbst & van Dishoeck 2009). These molecules are rarely released from dust grains into the gas phase at low temperatures. A small fraction is released into the gas phase by non-thermal processes such as cosmic ray and UV-induced photodesorption and desorption due to excess reaction energy, paving the way for molecular detection. The same occurs in cold starless cores as well, but the majority of solid phase molecules are mostly liberated after the protostar birth. The temperature increment and the outflow and accretion shocks further contribute to the liberation of molecules. At 20 K, CO is firstly liberated into the gas phase, followed by CH_4 and H_2CO. Above 100 K, the major constituent of grain mantles, H_2O ice, sublimates, and most complex organic molecules such as $HCOOCH_3$ and C_2H_5CN are also released into the gas phase. Whether saturated complex organic molecules are dominant, so-called Hot corino chemistry and Warm Carbon-Chain Chemistry (WCCC) appears. The chemical history contained within grain mantles appears in protostellar cores. Thus, it is very interesting to study how the chemical diversity starting from molecular clouds eventually ends up in planets. Although fundamental species such as CO, HCO^+, HCN, and H_2CO have been observed toward various initial stellar formation phases, observing less abundant COMs might help to trace and reconstruct the chemical evolution of the ISM. The idea that these molecules are inherited from the primordial stage of star formation of our Sun is supported by the correlation existing among CHO-, N-, and S-bearing prebiotic molecules detected in the low-mass protostar IRAS 16293-2422 and the bulk composition of the comet 67P/Churyumov-Gerasimenko (Drozdovskaya et al. 2019). The chemical complexity found in the Murchison and other meteorites (Burton et al. 2012; Pizzarello et al. 2006; Oba et al. 2022), fossils of the solar system formation process, also supports the formation of prebiotic molecules in space, but does not prove causation. As asteroids and planetesimals, from which meteorites originate, grew in size, they underwent secondary alteration events. Also known as post-accretion events, these latter provide additional opportunities for chemical reactions, either directly from thermal energy (thermal metamorphism, Huss et al. 2006) or from liquid water (aqueous alteration, Brearley 2006) resulting from melting water ices. The alteration of these bodies makes it therefore difficult to understand at what point the prebiotic molecules were actually formed in the ISM, making direct detection the only effective way to determine their actual

presence in space.

1.4 Fundamental concepts in radio astronomy

In order to understand what information is carried from space to the detector of the telescope sensitive to the wavelength of interest, it is necessary to understand how electromagnetic radiation propagates in the interstellar medium. We will also introduce the concepts of absorption and column density, and discuss the technical devices used to detect this information. In the following section, these points will be briefly discussed, opening the way for the actual topic of this thesis: rotational spectroscopy.

1.4.1 Radiative transfer

The fact that the ISM is permeated by baryons causes the radiation to interact with atoms and molecules, especially where their presence becomes noticeable, as in the case of molecular clouds. For simplicity, if we consider some photons in the frequency interval $(\nu, \nu + d\nu)$ passing through a surface element dA at an angle $d\omega$ with respect to the surface norm, we can express their energy per surface in the time interval dt as:

$$dE_\nu = I_\nu(s, \hat{n}, \nu, t)\hat{n} \cdot \hat{k} dA d\nu d\omega dt \,, \tag{1.20}$$

where I_ν is the specific intensity (also known as monochromatic intensity) of radiation of frequency ν, $\hat{n}$ is the direction of the intensity and $\hat{k}$ is the direction of the observer. The main effects involving a photon in the ISM are absorption, spontaneous emission, stimulated emission, scattering and collisional excitation/de-excitation. These effects can be considered by introducing two concepts: opacity and emissivity.

If we consider a column of area A and length s filled with particles, the radiation passing through can be attenuated either by absorption or scattering. The intensity of this radiation can be expressed by:

$$dI_\nu = -\kappa_\nu I_\nu ds \,, \tag{1.21}$$

where κ_ν [m^{-1}] stands for the *opacity* of the medium, i.e. a parameter that describes the effective cross section that matter exerts on the passage of radiation. A more intuitive way is to think in terms of the reciprocal of the opacity, namely the *mean-free path* of the radiation, for a given frequency. Opacity is mainly the result of bound-bound transitions, bound-free absorption, free-free absorption, electron scattering and macroscopic absorption/scattering. The first is due to the promotion of the electron of an atom to a higher energy state; the second is due to the loss of an electron by an atom following the absorption of a photon (ionisation); the third is due to the acceleration of a free electron following the absorption of a photon, but implies the presence of a nearby ion to conserve momentum and energy; the fourth is due to Thomson scattering, i.e. a photon scattered by a free electron; and the fifth is basically due to dust, which acts by extinction (absorption) and reddening. Thus, by rearranging the equation 1.21 and taking the integral, we

obtain:

$$\int \frac{dI_\nu}{I_\nu} = lnI_\nu = -\int_0^s \kappa_\nu ds + c \tag{1.22}$$

$$I_\nu = I_{\nu,0} e^{-\int_0^s \kappa_\nu ds} \tag{1.23}$$

$$I_\nu = I_{\nu,0} e^{-\tau_\nu}\,, \tag{1.24}$$

where $\tau_\nu = -\int_0^s \kappa_\nu ds$ is known as *optical depth*.

On the other hand, the same particles in the column of area A and length s, emit photons due to spontaneous/stimulated emission, scattering and de-excitation. This change in intensity can be expressed as:

$$dI_\nu = (\epsilon_{\nu,therm} + \epsilon_{\nu,scat} + ...)ds = \tag{1.25}$$

$$= \epsilon_\nu ds\,, \tag{1.26}$$

where ϵ_ν is defined as the *emission coefficient*. If we now consider both opacity and emissivity, the infinitesimal change in intensity I_ν [W/m^2/sr/Hz] of a parallel beam of photons now takes the form:

$$dI_\nu = -\kappa_\nu I_\nu ds + \epsilon_\nu ds\,, \tag{1.27}$$

where the two terms from left to right are the absorption and emission contributions respectively. The general *Time-independent radiative transfer equation* can be obtained by dividing by $d\tau_\nu$.

$$\frac{dI_\nu}{d\tau_\nu} + I_\nu = \frac{\epsilon_\nu}{\kappa_\nu} \equiv S_\nu \tag{1.28}$$

$$\frac{dI_\nu}{d\tau_\nu} = S_\nu - I_\nu\,, \tag{1.29}$$

where S_ν takes into account the effects of both opacity and emission, and is defined as *source function*. Multiplying both sides of the equation 1.29 by the integration factor e^{τ_ν} and integrating from $\tau_\nu = 0$ and $I_\nu = I_\nu(0)$ we get:

$$I_\nu = I_\nu(0)e^{-\tau_\nu} + \int_{\tau'_\nu=0}^{\tau_\nu} S_\nu e^{-(\tau_\nu - \tau')} d\tau'\,, \tag{1.30}$$

also known as the *general integral solution*. If changes in pressure, temperature and chemistry are considered negligible with respect to the photon mean free path, then it is possible to consider the system in *Local Thermodynamic Equilibrium* (LTE). Under this condition, the kinetic temperature ($T_{\rm kin}$), the excitation temperature ($T_{\rm ex}$) and the radiation temperature ($T_{\rm rad}$) can be assumed to have the same value. $T_{\rm kin}$ is the average kinetic energy of the particles in a system; it describes the temperature at which the particles are moving. $T_{\rm ex}$ is the average energy level of atoms or molecules within a given quantum state; it's relevant in systems with non-thermal excitation. $T_{\rm rad}$ reflects the temperature of the electromagnetic radiation emitted by a body; it's related to the intensity of the radiation emitted by an object. When these temperatures coincide, it implies a specific equilibrium condition within the system, where a thermal equilibrium is

reached between the kinetic, excitation and radiation temperatures. This simplifies the analysis and interpretation of the physical processes taking place in the system.

The intensity of the radiation can be assumed to be homogeneous and can be approximated by a black-body radiation $B_\nu(T)$ with a constant temperature T_{ex} along the line of sight. The equation 1.30 can then be expressed as:

$$I_\nu = I_\nu(0)e^{-\tau_\nu} + B_\nu(T_{ex})\left[1 - e^{-\tau_\nu}\right] . \tag{1.31}$$

Depending on the conditions of the ISM, two main cases can arise: the background radiation dominates the emission from the medium, or vice versa. Both scenarios have two sub-categories, depending on the optical depth of the cloud, which strongly influences the observed spectral lines. Let us look at these two borderline cases:

1. Background intensity dominates over emission from the medium:

– Optically thin ($\tau_\nu \ll 1$): $I_\nu = I_{\nu(0)} - \tau_\nu(I_\nu(0) - B_\nu(T_{ex}))$.
  This leads to two further sub-cases:

  – If $I_\nu(0) < B_\nu(T_{ex})$, emission lines are observed.
  – If $I_\nu(0) > B_\nu(T_{ex})$, absorption lines are observed.

– Optically thick ($\tau_\nu \gg 1$): $I_\nu = B_\nu(T_{ex})$

2. The emission of the medium dominates over the intensity of the background:

– Optically thin ($\tau_\nu \ll 1$): $I_\nu = \tau_\nu B_\nu(T_{ex})$

– Optically thick ($\tau_\nu \gg 1$): $I_\nu = B_\nu(T_{ex})$

If we want to study line intensities in a more quantitative way, we have to subtract from the I_ν line intensity the background intensity, which in the case of the Cosmic Background Radiation (CMB) has a temperature of $T_b = 2.73$ K. The line intensity is then given by:

$$\begin{aligned} \Delta I_\nu &= I_\nu - I_\nu(0) && (1.32)\\ &= I_\nu(0)e^{-\tau_\nu} + B_\nu(T_{ex})(1 - e^{-\tau_\nu}) - I_\nu(0) && (1.33)\\ &= \Big(B_\nu(T_{ex}) - B_\nu(T_{bg})\Big)(1 - e^{-\tau_\nu}) , && (1.34) \end{aligned}$$

with T_{bg} the background temperature. In radio astronomy, the intensity is expressed in terms of the temperature that a black-body would emit at that temperature. In this way, the Planck function relates the latter to the frequency of the transition. Using the concept of *brightness temperature* T_B[6]:

$$T_B = \frac{c^2}{2k_B\nu^2}\Delta I_\nu , \tag{1.35}$$

[6]The brightness temperature T_B represents the temperature of an hypothetical black-body that emits radiation with the same intensity as the observed source at a particular frequency. Essentially, it provides a convenient way to characterise the intensity of radiation from celestial bodies, irrespective of their actual temperatures.

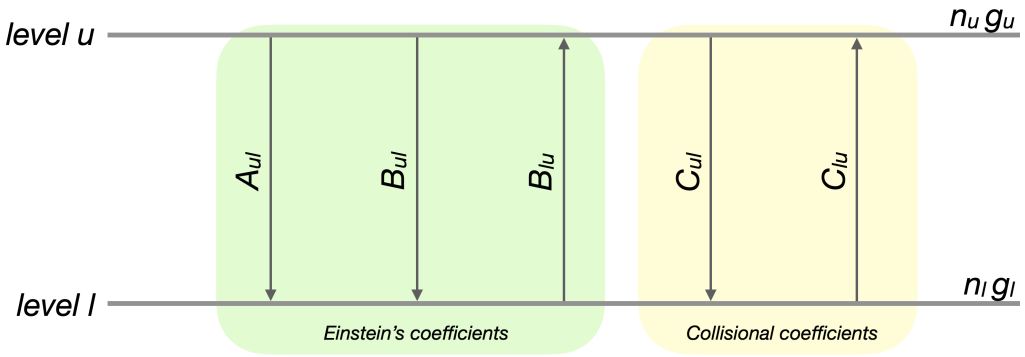

Figure 1.5: Two-level population system. n_u and n_l correspond to the upper and lower population level, respectively; g_u and g_l to degeneracies; from left to right, A_{ij} and B_{ij} stay for spontaneous emission, stimulated emission and absorption Einstein's coefficients, respectively; C_{ij} stay for collisional excitation and de-excitation coefficients, respectively.

and introducing the function $J_\nu(T)$[7] :

$$J_\nu(T) = \frac{h\nu}{k_B}\left(\frac{1}{e^{\frac{h\nu}{k_B T}} - 1}\right), \tag{1.36}$$

it is then possible to rewrite equation 1.34 as:

$$T_B = \Big(J_\nu(T_{ex}) - J_\nu(T_{bg})\Big)(1 - e^{-\tau_\nu}) \,. \tag{1.37}$$

1.4.2 Absorption coefficient and column density

Understanding the chemistry of the ISM, which ultimately leads to the formation of molecules of prebiotic interest, goes hand in hand with the ability to uniquely identify their presence in space. These molecules provide many clues to the physical state of the system to which they belong, such as density, temperature, the kinetics of the reactions involved and the molecular abundances themselves. But whether such quantities are derived depends on what is hidden in the signal observed by the telescope. In radio astronomy, the measurement is simply the photon energy required for the target molecule to move between two energy levels. To better explain this concept, in Figure 1.5 we introduce the two-level system. Defining two energy levels u and l, we are interested in finding the population levels n_u and n_l as a function of temperature T and density n_{tot}.

For a given energy level, $B_{ij}J_\nu$ describes the probability of absorption in the unit time given B_{ij} the Einstein coefficient between the two levels and J_ν the mean intensity of the molecule,

[7]The Rayleigh-Jeans temperature $J_\nu(T)$ is a concept used to describe the intensity of radiation at a specific frequency ν. It is derived from the classical Rayleigh-Jeans law, which approximates the spectral radiance of black-body radiation at low frequencies and high temperatures. This approximation breaks down at high frequencies or low temperatures, where the quantum mechanical effects become significant.

given by:

$$J_\nu = \frac{1}{4\pi}\int I_\nu d\Omega\,, \tag{1.38}$$

with $d\Omega$ the solid angle. We can express the energy of an electromagnetic wave as:

$$-dI_\nu d\nu d\Omega dr dS = \frac{h\nu}{4\pi}\phi\nu(n_{nl}B_{lu} - n_u B_{ul})I_\nu d\nu d\Omega dt dV\,, \tag{1.39}$$

where n_i is the number of molecules in the given energy level and $\phi(\nu)$ is the normalised function of the profile. Since $dV = dS\,dx$, by analogy with the left side of the equation 1.21, the absorption coefficient can be written as α_ν:

$$\alpha_\nu = \frac{h\nu}{4\pi}\phi(\nu)(n_{nl}B_{lu} - n_u B_{ul})\,. \tag{1.40}$$

Considering that the absorption and emission coefficients are related according to:

$$g_l B_{lu} = g_u B_{ul} \tag{1.41}$$

$$B_{ul} = \frac{c^2}{2h\nu_{ul}^3}A_{ul}\,, \tag{1.42}$$

where g_i stands for the degeneracy of the level i and nu_{ul} for the resonance frequency, the equation 1.40 can be expressed as:

$$\alpha_{ul} = \frac{c^2 n_u}{8\pi\nu_{ul}^2\Delta_\nu}\left\{e^{\frac{h\nu_{ul}}{k_B T}} - 1\right\}A_{ul}\,. \tag{1.43}$$

Assuming a temperature with a Boltzmann distribution, the equation 1.43 relates the absorption coefficient to the population distribution for an upper state N_u. Since the column density of molecules in the upper energy state u is given by integrating the volume density n_u over the path length ds:

$$N_u = \int n_u ds\,, \tag{1.44}$$

the number of molecules in the upper energy level u (N_u) of a molecule can be related to the total population of all energy levels in the molecule N_{tot} as:

$$\frac{N_u}{N_{tot}} = \frac{g_u}{Q}e^{-\frac{h\nu_u}{k_B T_{ex}}}\,, \tag{1.45}$$

where Q stays for the partition function. It represents the sum of the statistical weights of all possible states accessible to the system, accounting for both the degeneracy of the energy levels and the Boltzmann factors associated with them. As shown in Mangum & Shirley 2015, combining the absorption coefficient, the Boltzmann statistical equilibrium equation, the spontaneous emission coefficient A_{ul} and our definition of the column density in equation 1.44, it is possible to relate the optical depth τ_ν to the number of molecules in the upper energy state N_u as:

$$N_u = \frac{3h}{8\pi|\mu_{lu}|^2}\frac{1}{e^{\frac{h\nu}{k_B T_{ex}}} - 1}\int \tau_\nu d\nu\,, \tag{1.46}$$

The equation 1.46 can now be used to obtain the total molecular column density N_{tot}:

$$N_u = \frac{3h}{8\pi|\mu_{lu}|^2}\frac{Q}{g_u}e^{-\frac{h\nu}{k_B T_{ex}}} \times \frac{1}{e^{\frac{h\nu}{k_B T_{ex}}} - 1}\int \tau_\nu d\nu \,. \tag{1.47}$$

where $|\mu_{lu}|^2$ is the dipole matrix element associated with the line strength S and the dipole moment μ, such that $|\mu_{jk}|^2 \equiv S\mu^2$ (for a more detailed explanation of the dipole moment, see section 1.5.7). T_{ex} is generally not known, but assuming LTE conditions, the excitation temperature is equivalent to the temperature of gas, allowing the corresponding column density to be derived. The equation 1.47 allows us to understand the amount of the molecule of interest along the line of sight, which is essential for estimating the abundance of a molecular species in the ISM medium. In the astrochemical context, this has important implications as it allows us to elucidate the chemical pathways involved, and ultimately helps us to understand how the building blocks of life are formed in the ISM.

1.4.3 Elements of radioastronomy

Since the aim of this work is to study the presence of new COMs in the ISM, it is necessary to consider the physical conditions of the interstellar objects that have the highest number of these molecular species, i.e. molecular clouds. As mentioned in section 1.3.4, these environments are among the coldest regions of the ISM, with temperatures typically in the range of a few tens of K. In general, each object emits a range of electromagnetic radiation that follows the typical black-body profile, such as:

$$B_\nu(\nu, T) = \frac{2h\nu^3}{c^2}\frac{1}{\exp\left(\frac{h\nu}{k_B T}\right) - 1} \tag{1.48}$$

The equation 1.48, also known as *Planck's law*, relates the thermal energy to the frequency of a particular transition, be it electronic, vibrational or rotational. In the case of molecular clouds, their low temperatures are mostly rotational/vibrational molecular states, which are in the millimetre and sub-millimetre range. From Figure 1.6, which shows a schematic view of atmospheric opacity as a function of wavelength, it can be seen that the 1 cm-10 m range (30-0.3 GHz) appears to be almost transparent at the Earth's surface. This makes it possible to build large ground-based radio facilities (antenna diameter D $\sim 10 - 100$ m), eliminating all the costs associated with sending space-observing instruments into orbit. The main limitation affecting the signal is the presence of water molecules[8], which, being vibrationally sensitive at 100-1000 GHz (0.3-0.03 cm^{-1}), absorb and limit the arrival of such radiation at the Earth's surface. This problem is partially overcome limiting the construction of radio telescopes to high altitudes, making them the perfect tools to probe the cold universe at frequencies invisible to optical and high-energy telescopes. In this way, we can see not only interstellar molecules, but also cosmic dust and forming stars in the interior of molecular clouds.

[8]Other molecules like O_2 and O_3 play an important, albeit minor role. More information can be found in (Pardo et al. 2001)

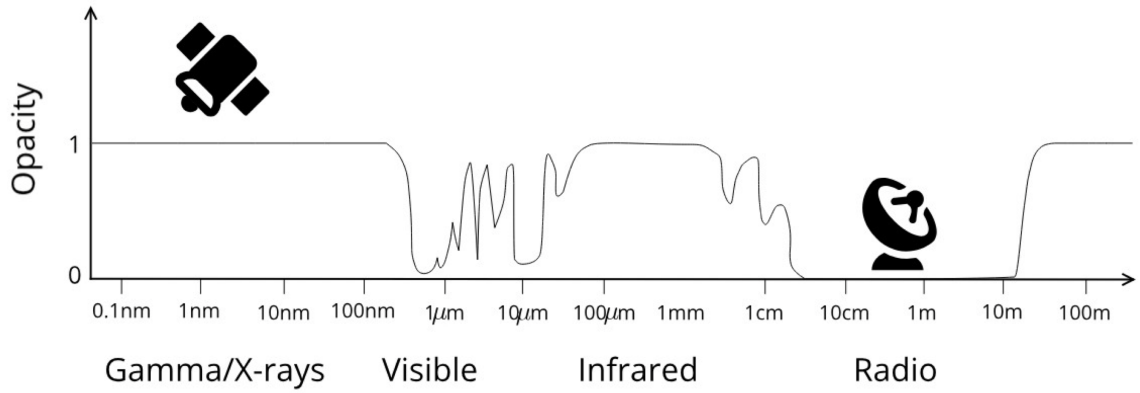

Figure 1.6: Atmospheric opacity as a function of wavelength. The figure is a courtesy of Redaelli (2020).

The resolution of a telescope is proportional to the diameter of its antenna and the frequency of the observed radiation according to $\sim \lambda/D$. Since we are interested in radio wavelengths, to increase the resolution we can only work on the D parameter.

We can think of two strategies: either we go for larger and larger telescopes (single dish), or we combine them together to have very wide base lines (interferometry). For example, by combining the antennas in different configurations, with interferometry we can achieve a resolving power equivalent to that of a single telescope several kilometres in diameter: 1.7 km for NOEMA (IRAM 2024) and 16 km for ALMA (ALMA 2021). Nevertheless, each technique has advantages and disadvantages and must be used to address specific questions. While interferometry's main goal is to resolve the large-scale structure at a high level of detail (generally mapping circumscribed regions of the sky), a single dish has the advantage of being able to probe a much larger region of the sky. Specifically, for first detection measurements the single dish technique is preferred, as it can achieve a sufficient level of sensitivity while probing a larger area. Very often it happens the two techniques are both employed to study the same source, but single dish measurements are always conducted at first, to better capture the nature of the overall source. For the scope of this thesis it is therefore more important to access larger regions of the sky than to be able to characterise its details very well. As we saw in section 1.3.4, after the heavy chemical elements are formed and ejected when stars die, we still do not know exactly how these elements group together to form complex prebiotic molecules. Understanding this missing link is crucial to understand how stars are born and die, and how they eventually form new planets around them.

In the works later presented we have used a classic single dish parabolic antenna, employing the IRAM 30 m telescope at Pico Veleta (2850 m a.s.l.) in Sierra Nevada (ESP) and the Yebes 40 m (931 m a.s.l.) in Guadalajara (ESP). Both telescopes are equipped with a suite of highly sensitive large bandwidth high resolution spectrometers capable of producing wide-area radio images, allowing the study of faint sources over a large portion of the sky. The IRAM 30-metre telescope covers the frequency range from 80 to 370 GHz (3 to 0.8 mm) and the Yebes 40-metre telescope covers the frequency ranges from 2 GHz to 90 GHz (150 to 3 mm).

In Figure 1.7 is shown the typical *Cassagrain configuration* telescope. The antenna collects

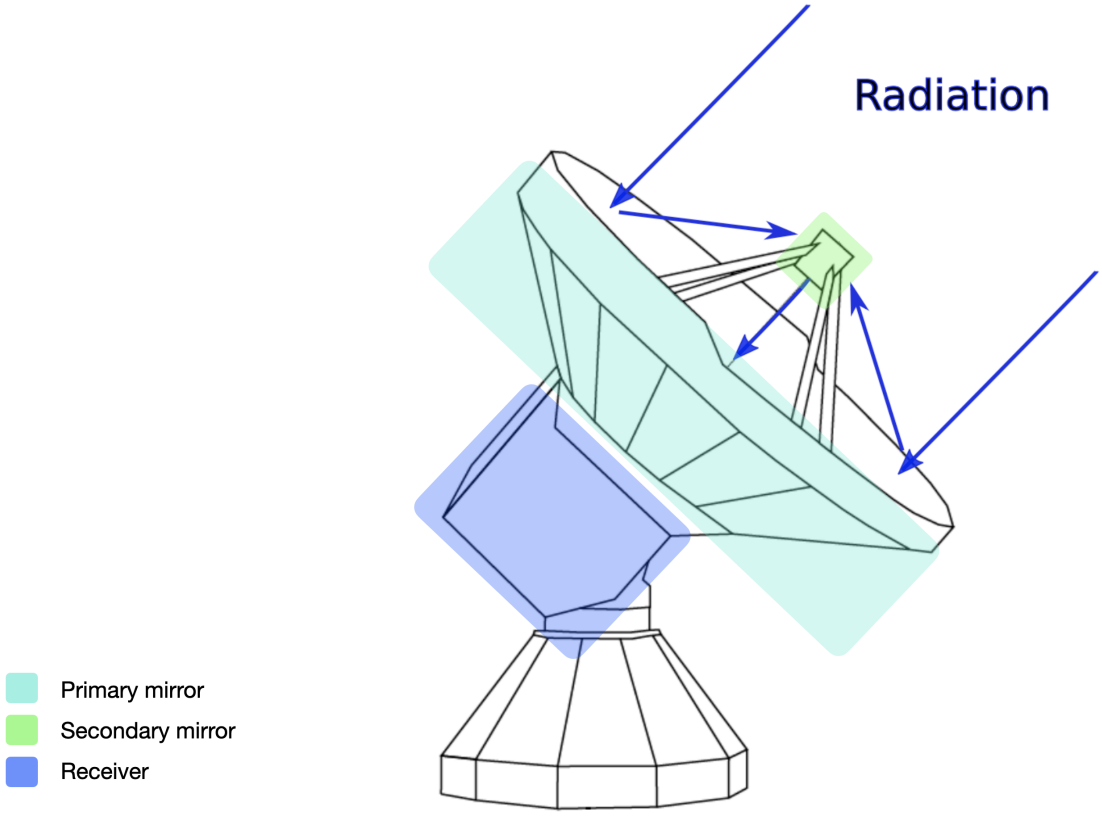

Figure 1.7: Main components of the single dish radio telescope. The image has been taken from Chantzos (2020) and modified.

the radiation from the primary reflector (or parabolic dish), focuses it on a secondary mirror (or sub-reflector) and sends it through a series of optical devices to the receivers (or detectors). The latter are known as the back-end part of the telescope, while all the former make up the front-end section. The shape of the signal collected by the primary reflector appears to have a *main lobe* and several axisymmetric *side lobes*. These axisymmetric lobes are the result of the diffraction of the primary beam and have the effect of reducing the power collected by the first lobe. Calculating the Half Power Beam Width (HPBW) of the main lobe gives the angular resolution of the telescope, which, as previously anticipated, for a given wavelength λ and telescope diameter D is given by HPBW $\sim \lambda/D$.

To get a clean signal, we need to calibrate the telescope according to the wavelengths we are interested in. We can distinguish between the cm-wavelength regime and the mm-wavelength regime. For the former, calibration is done by comparing artificially noise-induced signals (with noise diodes on) with natural noise signals (with noise diodes off). For the latter, the calibration is done by comparing on-source measurements with cold sky and with a room temperature load measurements. An atmospheric model then allows the on-source signal to be calibrated, a method also known as the *chopper wheel method*. (Kutner & Ulich 1981).

The efficiency of the antenna can be summarised by two important parameters: the *beam*

efficiency (η_{MB}) and the *forward efficiency* F_{eff}. The former estimates the fraction of the power concentrated in the main lobe relative to the power scattered in the side lobes; the latter relates the radiation coming from the front of the antenna to the total power coming from the entire solid angle. This makes it possible to express spectroscopic data in terms of *antenna temperature* T_A, i.e. the temperature at which a resistor would have to emit the same power detected by the receiver, analogous to the source brightness of the equation 1.35. Correcting the antenna temperature for line-of-sight opacity τ_ν^{atm}:

$$T'_A = T_A e^{\tau_\nu^{atm}} , \tag{1.49}$$

and taking into account η_{MB} and F_{eff}, the *main beam temperature* can be expressed as:

$$T_{MB} = \frac{F_{eff}}{\eta_{MB}} T'_A , \tag{1.50}$$

Assuming a source angular size comparable to the beam resolution, i.e. $T_{MB} \approx T_B$, we can consider the main beam temperature to be equal to the source brightness temperature.

1.5 Rotational spectroscopy

As mentioned earlier, this chapter is the core upon which this thesis is built. Most of the molecules detected in space owe their discovery to rotational spectroscopy. This discipline describes how a quantum object interacting with an incident electromagnetic radiation in the radio frequency range gives rise to a rotational spectrum. Its characterisation will make it possible to identify molecules that have not yet been identified in the ISM, their characteristics and the features of the same environment in which these molecules are detected. In the following pages, the reader will find the minimum theoretical background to understand the physical reasons behind this work.

As everyone writes according to their own culture, so quantum mechanics adopts different notations according to the use to be made of the Schrödinger's equation. For this reason, it has been decided to make the notation used in this chapter unambiguous. Examples are given in brackets, the meaning will become clear later on. Vectors and vector operators are written in bold italics (**J**); vector and tensor components are written in italics with subscripts (J_z, $S_{\alpha,i}$); quantum numbers, parameters and other quantities are written in light italics (j, B_v) or Greek letters (α). Some vector operations are summarised by removing the subscripts in matrix notation (α goes as ${S_{\alpha i}}^{-1}$ to become S^{-1}). H, J^2 and J correspond to the Hamiltonian, the scalar operator and its square. This chapter echoes some of the many concepts expressed in the exquisite Kroto (1992).

1.5.1 The bare minimum to introduce quantum mechanics

Like any physical system, we can define a molecular object p in motion as consisting of the sum of the total kinetic energy T and the total potential energy V as:

$$E = T + V\,. \tag{1.51}$$

The factors in this expression can be expressed in terms of the momentum of nuclei P_n and electrons P_e, respectively:

$$T = \sum_n \frac{\mathbf{P_n^2}}{2m_n} + \sum_e \frac{\mathbf{P_e^2}}{2m_e}\,, \tag{1.52}$$

and the potential energies:

$$V = V_{nm} + V_{ee} + V_{ne}\,. \tag{1.53}$$

The observable $\bar{p}_i$, the moment of inertia of object i, and its position q_i, are related by $\bar{p}_i = -i\hbar\partial/\partial q_i$, with the reduced Planck constant $\hbar \equiv h/2\pi$. In this thesis $p_i = -i\partial/\partial q_i$ will imply $p_i = \bar{p}_i$.

The link between the classical and quantum realms is built on the relationship between these two quantities, as:

$$[\bar{q}_i, \bar{p}_j] = i\hbar\delta_{ij} \equiv [q_i, p_j] = i\delta_{ij}\,. \tag{1.54}$$

In equation 1.54, $\bar{q}_i$ and $\bar{p}_j$ are the quantum operators corresponding to the conjugate variables in classical mechanics, q_i and p_j; $[A, B]$ stays for the commutator of the operators A and B, defined

as $AB - BA$; δ_{ij} is the Kronecker delta, which is 1 if $i = j$ and 0 otherwise. This represents the fundamental uncertainty between simultaneous measurements of position and momentum in quantum mechanics: position and momentum do not commute, their order of measurement does affect the result. Another important relation is:

$$[\bar{J}_i, \bar{J}_j] = i\hbar e_{ijk}\bar{J}_k \equiv [J_i, J_j] = ie_{ijk}J_k \,. \tag{1.55}$$

In equation 1.55, $\bar{J}_i$ are the quantum operators associated with the classical counterparts J_i; e_{ijk} is the antisymmetric Levi-Civita symbol, whose values are +1, -1, or 0 depending on permutations of i, j, k. Non-orthogonal components cannot be simultaneously measured unless a certain indeterminacy, a direct manifestation of Heisenberg's uncertainty principle.

With this in mind, we can then express the Hamiltonian that takes into account what has been introduced as:

$$H = -\sum_n \frac{\nabla_n^2}{2m_n} - \sum_e \frac{\nabla_e^2}{2m_e} + V_{nn} + V_{ee} + V_{ne} \,, \tag{1.56}$$

1.5.2 The harmonic oscillator

Lets assume we can describe the energy of an object as it was a spring. Hooke's helps us to express the force acting on a mass m in acceleration as:

$$m\ddot{x} = -kx \,. \tag{1.57}$$

The classical Hamiltonian describes the behaviour of the object as:

$$H = \frac{p_x^2}{2m} + \frac{k}{2}x^2 \,, \tag{1.58}$$

with $p_x = \partial T/\partial \dot{x} = m\dot{x}$. Remembering equation 1.54, we can express the Hamiltonian in the quantum form. This exercise returns the equation:

$$H = \alpha p^2 + \beta q^2 \,, \tag{1.59}$$

for which these two solutions can be found:

$$H = \frac{1}{2}(P^2 + \omega^2 Q^2) \tag{1.60}$$

$$H = \frac{1}{2}\omega(p^2 + q^2) \,. \tag{1.61}$$

Solving the system allow us to express equation 1.58 with respect to p rather than q. In our case we will take the former, but the resolution with respect to the latter makes just as much physical sense. In both of these approaches, ω takes the meaning of classical motion frequency.

Due to the probabilistic nature of the object we are dealing with, we need to imagine a vector space formed by all those spaces that, orthogonal to each other, return a correspondence in the scalar space. This latter represents the actual value of the observable, to which in turn is associated the probability distribution embedded in the vector space. The mathematical object that

fulfil this requirement is none other than an eigenvalues equation. Enforcing bounding conditions, we solve the partial differential equations of the Hamiltonian on a finite domain, obtaining a discrete set of solutions. When employed to describe an energy, it assumes the form:

$$H\left|E_n\right\rangle = E\left|E_n\right\rangle \,, \tag{1.62}$$

where E stays for the scalar associated with the energy E_n of the system. Whether our operators satisfy the commutativity requirements and the possibility of auto-adjoined operators, summarised respectively as:

$$[\mathbf{A}, \mathbf{B}] = 0 \tag{1.63}$$

$$[\mathbf{A}, \mathbf{B}] = k\mathbf{B}\,, \tag{1.64}$$

it is possible to define the mathematical object that describe the observables above mentioned. While equation 1.63 define the commutator between two operators acting on a Hilbert space quantifying how well the two observables described by these operators can be measured simultaneously, equation 1.64 allows us to define the so called *ladder* operators. This same equation takes the form:

$$F^{\pm} = q \pm ip\,, \tag{1.65}$$

Equation 1.64 helps us to imagine the true nature of these operators: a mathematical object that generates a new eigenfunction A with eigenvalues $(\mathbf{A}' + \mathbf{k})$. Applying equation 1.65 to equation 1.62 returns:

$$H(F^{\pm}\left|E_n\right\rangle) = (E_n \mp \omega)(F^{\pm}\left|E_n\right\rangle)\,. \tag{1.66}$$

As we continue to apply $F^{\pm}$ to the space vector $|E_n\rangle$, we obtain the energy level values, all equispaced by ω, until we reach the energy maximum $|E_{\uparrow}\rangle$ /minimum $|E_{\downarrow}\rangle$. If we consider F^{+}:

$$F^{+}\left|E_{\downarrow}\right\rangle = \frac{1}{2}\omega\left|E_{\downarrow}\right\rangle \,, \tag{1.67}$$

the energy values are:

$$E(\upsilon) = \omega\Big(\upsilon + \frac{1}{2}\Big). \tag{1.68}$$

We can then visualise the matrix of the object $\langle\upsilon|\,H\,|\upsilon\rangle = E(\upsilon)$ looking at Table 1.3.
In essence, the ladder operators allow us to move along the $\langle\upsilon|\,H\,|\upsilon\rangle$'s diagonal elements. With equation 1.65, we can reconstruct the matrix form of p and q as:

$$\alpha\begin{bmatrix} 0 & \sqrt{1} & 0 & . & . \\ \sqrt{1} & 0 & \sqrt{2} & . & . \\ 0 & \sqrt{2} & 0 & \sqrt{3} & . \\ 0 & . & \sqrt{3} & . & . \\ . & . & . & . & . \end{bmatrix}_{\mathbf{p}} \qquad i\alpha\begin{bmatrix} 0 & -\sqrt{1} & 0 & . & . \\ \sqrt{1} & 0 & -\sqrt{2} & . & . \\ 0 & \sqrt{2} & 0 & -\sqrt{3} & . \\ 0 & . & \sqrt{3} & . & . \\ . & . & . & . & . \end{bmatrix}_{\mathbf{q}} \tag{1.69}$$

where $\alpha = 1/\sqrt{2}$. Even if non-diagonal, these matrices keep the Hermitian flavour ($A^{\dagger}$ = A).

Table 1.3: Energy elements of $\langle \upsilon | H | \upsilon \rangle = E(\upsilon)$

H	$\|0\rangle$	$\|1\rangle$	$\|2\rangle$	$\|3\rangle$	...
$\langle 0 \|$	$\frac{1}{2}\omega$	0	0	0	0
$\langle 1 \|$	0	$\frac{3}{2}\omega$	0	0	0
$\langle 2 \|$	0	0	$\frac{5}{2}\omega$	0	0
$\langle 3 \|$	0	0	0	$\frac{7}{2}\omega$	0
...	0	0	0	0	...

1.5.3 The perturbed harmonic oscillator

As the harmonic oscillators we will be dealing with are mostly perturbed, we have to consider non-diagonal matrices. To solve these matrices though, what one does is brought back to the diagonal case. In practice, the strategy is to imagine the overall Hamiltonian as the sum of two contributions:

$$H = H^0 + H' \,. \tag{1.70}$$

The total Hamiltonian H is defined on the harmonic oscillator basis defined by H^0. In general, this approach works as long as $H^{'}$ contributions are one order of magnitude smaller than H^0 contributions [9]. To determine the matrix elements we can assume that an equation of the form exists:

$$\mathbf{HU} = \mathbf{UE} \,, \tag{1.71}$$

where $\mathbf{U}$ obeys the similarity transformation $\mathbf{U^{-1}HU}$, and $\mathbf{E}$ is the diagonal eigenvalue matrix of equation 1.62. Solving the secular equation:

$$|\mathbf{H} - \mathbf{EI}| = 0 \,, \tag{1.72}$$

with $\mathbf{I}$ standing for the unit matrix, we can obtain the new eigenfunctions related to the $\mathbf{E}$ eigenvalues. Since in respect of the equation 1.62, H^0 of equation 1.70 can also be expressed as:

$$H^0 \, |\upsilon\rangle = E^0_\upsilon \, |\upsilon\rangle \ , \tag{1.73}$$

the resolution of the relation 1.72 leads to a new basis functions representation:

$$|\tilde{\upsilon}\rangle = \sum_\upsilon c^{\tilde{\upsilon}}_\upsilon \, |\upsilon\rangle \ , \tag{1.74}$$

that is nothing but a linear combination of the original basis functions $|\upsilon\rangle$ weighted by $c^{\tilde{\upsilon}}_\upsilon$ coefficients. The space of basis functions of $H^{'}$ is thus built on the space of basis functions of H^0,

[9] The difference between the mn^{th} and mn^{th} diagonal element has to be minor (or comparable) than (to) an order of magnitude.

allowing one to always deal with diagonal matrices. For two states $|m\rangle$ and $|n\rangle$ we have that for the H^0 Hamiltonian:

$$H^0 |m\rangle = E_m^0 |m\rangle \tag{1.75}$$

$$H^0 |n\rangle = E_n^0 |n\rangle \ . \tag{1.76}$$

Finding the roots of the secular determinant:

$$\begin{vmatrix} E_m^0 - E & \langle m| H |n\rangle \\ \langle m| H |n\rangle^* & E_n^0 - E \end{vmatrix} , \tag{1.77}$$

and applying the transformation matrix:

$$\mathbf{U} = \begin{bmatrix} cos\theta & sin\theta \\ -sin\theta & cos\theta \end{bmatrix} , \tag{1.78}$$

to equation 1.77, we obtain the new basis functions space for which $E^{'}$ is diagonal. In this case, the new vector spaces are:

$$|\tilde{m}\rangle = cos\theta |m\rangle + sin\theta |n\rangle \tag{1.79}$$

$$|\tilde{n}\rangle = -sin\theta |m\rangle + cos\theta |n\rangle \ . \tag{1.80}$$

Further transformations allow to determine all off-diagonal degenerate matrix elements, or to associate to these energy values functions that allow to describe them.

A similar result can be obtained through perturbation theory. Assuming distinct states ($m \neq n$) and a non zero energy difference that separates them, we can associate to the equation 1.62 the energies of the form:

$$E = E^0 + E^1 + E^2 + ... , \tag{1.81}$$

where $H^0 |m\rangle = E_m^0 |m\rangle$. H' stays for the corrective term to which corresponds the energies E^1, E^2, ... The individual contributions are given by:

$$E_m^0 = \langle m| H^0 |m\rangle \tag{1.82}$$

$$E_m^1 = \langle m| H^{'} |m\rangle \tag{1.83}$$

$$E_m^2 = \sum_n^{'} \frac{\langle m| H^{'} |n\rangle \langle n| H^{'} |m\rangle}{E_m^0 - E_n^0} \ . \tag{1.84}$$

This alternative is often used in computational chemistry and, as we see later on, is widely used in the works herein presented.

1.5.4 The rotational Hamiltonian

A clever way to solve equation 1.56 takes the name of *Born-Oppenheimer approximation*. Introducing the expansive parameter $\kappa = (m_e/m_p)^{1/4}$,where m_e and m_p are respectively the electron

and proton masses, the devises of this idea repeatedly employed perturbation theory to expand equation 1.56 to many order of contributions. Neglecting higher orders[10] and truncating the expansion to fourth-order contribution, we get the energies of the system: $E_r \sim \kappa^2 E_\upsilon \sim \kappa^4 E_e$. These place the rotational energy E_r two orders of magnitude below the vibrational energy E_υ that, in turn, lays two orders of magnitude below the electronic energy E_e. Equation 1.56 can then be split into an electronic and a nuclear part:

$$H = \underbrace{-\frac{1}{2m_e}\sum_e \nabla_e^2 + V_{ee} + V_{ne} + V_{nn})}_{\text{electron part}} \underbrace{-\sum_n \frac{1}{2m_n}\nabla_n^2}_{\text{nuclear part}}, \tag{1.85}$$

which assumes a wave function of the type:

$$\psi(\mathbf{q_e q_n}) = \psi_\mathbf{e}(\mathbf{q_e q_n})\psi_\mathbf{n}(\mathbf{q_n})\,. \tag{1.86}$$

The Schrödinger equation for a specific internuclear configuration q_n then becomes:

$$H_e(\mathbf{q_e q_n})\psi_\mathbf{e}(\mathbf{q_e q_n}) = E_e(\mathbf{q_n})\psi_\mathbf{e}(\mathbf{q_e q_n})\,, \tag{1.87}$$

and retains its validity as long as electronic states do not interact, i.e. when the term $\nabla_n^2\Psi_e(\mathbf{q_e q_n})$ begins to make non-negligible contributions.

Now that we have decoupled the nuclear wave function from the electronic one, we want to consider the average displacements of the nuclei with respect to their equilibrium positions. A convenient way is to change the centre of mass of the molecule and the reference system from a *space-fixed* to a *molecule-fixed axis system*, through:

$$\rho_\mathbf{n} = \mathbf{R} + \mathbf{S^{-1}}(\mathbf{r_n^e} + \mathbf{d_n}) \tag{1.88}$$

where $\rho_\mathbf{n}$ stands for the position vector, $\mathbf{R}$ for the three-dimensional vector describing the molecular mass centre, $\mathbf{S^{-1}}$ the inverse of the matrix $\mathbf{S}$ which in turn allows us to move from space-fixed to molecular-fixed orientation, $\mathbf{r^e}$ the equilibrium coordinate and $\mathbf{d_n}$ the displacement relative to the nucleus n. To note, the left side of equation 1.87 has 3N degrees of freedom but on the right one both $\mathbf{R}$ and $\mathbf{S}$ have 3, which results in a total of 6 degrees of freedom for d_n. Considering the constrains imposed by Eckart's conditions[11], there are therefore only 3N-6 degrees of freedom allowed for d_n.

Since the kinetic energy of the system can be expressed as:

$$T = \frac{1}{2}\sum_n m_n \dot{\rho_\mathbf{n}}\cdot\dot{\rho}_\mathbf{n} \tag{1.89}$$

the derivative of the position vector ρ:

$$\dot{\rho_\mathbf{n}} = \dot{\mathbf{R}} + \dot{\mathbf{S}}^{-1}(\mathbf{r_n^e} + \mathbf{d_n}) + \dot{\mathbf{S}}^{-1}\dot{\mathbf{d}}_\mathbf{n} \tag{1.90}$$

[10] Higher order contributions are relevant to take into account vibro-rotational relations.

[11] Eckart's conditions are two: the first implies that d_n does not constitute a translation, so that the centre of mass does not change; the second that it does not correspond to rotations.

leads to 9 terms which, forcing Eckart's conditions, reduced to 3. These remaining terms are the vibrational kinetic energy T_υ:

$$T_\upsilon = \frac{1}{2}\sum_n m_n \dot{\mathbf{d}}_\mathbf{n}\dot{\mathbf{d}}_\mathbf{n}\,, \tag{1.91}$$

the roto-vibrational kinetic contribution:

$$T_{\upsilon r} = \sum_n m_n \omega_\alpha e_{\alpha\beta\gamma} d_{n\beta}\dot{d_{n\gamma}}\,, \tag{1.92}$$

with $e_{\alpha\beta\gamma}$ as the permutation symbol, and the pure rotational kinetic energy T_r[12]:

$$T_r = \frac{1}{2}\sum_n m_n e_{\epsilon\alpha\gamma} e_{\epsilon\beta\delta}\omega_\alpha\omega_\beta r_{n\gamma} r_{n\delta}\,. \tag{1.93}$$

The last equation is the one on which this thesis work is built. If we do not consider the classical motion frequency ω, we can rewrite equation 1.93 in its tensor form as:

$$I_{\alpha\beta} = \sum_n m_n e_{\epsilon\alpha\gamma} e_{\epsilon\beta\delta} r_{n\gamma} r_{n\delta} \tag{1.94}$$

$$= \sum_n m_n(\delta_{\alpha\beta} r_{n\gamma} r_{n\gamma} - r_{n\alpha} r_{n\beta})\,, \tag{1.95}$$

whose tensor elements are:

$$I_{aa} = \sum_n m_n[r_{nb}^2 + r_{nb}^2] \qquad I_{ab} = -\sum_n m_n[r_{na} + r_{nb}] \tag{1.96}$$

$$I_{bb} = \sum_n m_n[r_{na}^2 + r_{nc}^2] \qquad I_{bc} = -\sum_n m_n[r_{nb} + r_{nc}] \tag{1.97}$$

$$I_{cc} = \sum_n m_n[r_{na}^2 + r_{nb}^2] \qquad I_{ca} = -\sum_n m_n[r_{nc} + r_{nb}]\,. \tag{1.98}$$

The pure rotational kinetic energy T_r can then be written as:

$$T_r = \frac{1}{2} I_{\alpha\beta}\omega_\alpha\omega_\beta\,. \tag{1.99}$$

Therefore, including all contributions so far derived, we can express the total kinetic energy T as:

$$T = \frac{1}{2}\omega^\dagger \mathbf{I}\omega + \sum_n m_n \omega\cdot(\mathbf{d}_\mathbf{n}\times\dot{\mathbf{d}}_\mathbf{n}) + \frac{1}{2}\sum_n m_n \dot{\mathbf{d}}_\mathbf{n}\cdot\dot{\mathbf{d}}_\mathbf{n}\,. \tag{1.100}$$

Note how the terms correspond to the equations 1.99, 1.92, 1.91, respectively. Since we are only interested in the term for the pure rotational kinetic energy T_r, we can represent its Hamiltonian

[12] To do so, we have to define the instantaneous coordinate of the n$^{\text{th}}$ atom with respect to *a, b, c* axes as r_n, namely $\mathbf{r_n} = \mathbf{r_n^e} + \mathbf{d_n}$

with respect to the molecule-fixed axes a, b and c. The classical angular momentum J_α can therefore be expressed as:

$$J_\alpha = \frac{\partial T}{\partial \omega_\alpha} = I_{\alpha\beta}\omega_\beta \,, \tag{1.101}$$

which, using tensor notation $\mathbf{J} = \mathbf{I}\omega$, results in expressing the pure rotational kinetic energy as $T_r = \frac{1}{2}(\mathbf{I}\omega)^\dagger \mathbf{I}^{-1}(\mathbf{I}\omega) = \frac{1}{2}(\mathbf{J})^\dagger \mathbf{I}^{-1}\mathbf{J}$. This way we can express the corresponding Hamiltonian as:

$$H_r = \frac{1}{2}\mu_{\alpha\beta}J_\alpha J_\beta \,, \tag{1.102}$$

where $\mu_{\alpha\beta}$ corresponds to $\mu = \mathbf{I^{-1}}$. Since $\mathbf{I}$ is symmetric, it can be diagonalised after unitary transformations along a, b and c axes (3x3 matrices). Vanishing the cross-products of equations 1.99 and 1.102, only the corresponding diagonal elements of $\mathbf{I}$ are left. The latter are known as the *Principal moments of inertia*, and the a, b and c axes as the *Principal axes*. Equation 1.99 then becomes:

$$T_r = \frac{1}{2}(I_A\omega_A^2 + I_B\omega_B^2 + I_C\omega_C^2) \,. \tag{1.103}$$

which, remembering equation 1.101, can be re-expressed as the pure rotational Hamiltonian:

$$H_r = AJ_A{}^2 + BJ_B{}^2 + CJ_C{}^2 \,, \tag{1.104}$$

with A, B, C the *Principal rotational constants*, whose values are:

$$A = \frac{\mu_A}{2} = \frac{1}{2I_A} \tag{1.105}$$

$$B = \frac{\mu_B}{2} = \frac{1}{2I_B} \tag{1.106}$$

$$C = \frac{\mu_C}{2} = \frac{1}{2I_C} \,. \tag{1.107}$$

Now, it is possible to distinguish the problem according to the type of rotor to be analysed. By convention, $I_A \leq I_B \leq I_C$, so that $A \geq B \geq C$. We can therefore define four classes of rotors as:

Table 1.4: Rotor symmetry types.

Type	sub-type	Relation	Example
Spherical tops		$I_A = I_B = I_C$	CH_4
Linear molecules		$I_A = 0, I_B = I_C$	OCS
Symmetric top	prolate	$I_A < I_B = I_C$	CH_3Br
	oblate	$I_A = I_B < I_C$	NH_3
Asymmetric rotor		$I_A \leq I_B \leq I_C$	H_2O

1.5.5 Eigenvalues and eigenfunctions of the Angular momentum operators

It must be kept in mind that the $\boldsymbol{J}$ operator commutes with the angular momentum square operator $\boldsymbol{J}^2$, paving the way to a series of eigenfunctions that have eigenvalues for both of these operators. If we consider the z-axis, the relative basis set is denoted as $|J^2 J_z\rangle$. The relation between the latter and the other two axes is underlined by the equation 1.65, which takes the forms of the shift operators:

$$J_+ = J_x + iJ_y \qquad\qquad J_- = J_x - iJ_y\,. \tag{1.108}$$

Note that $(J_+)^\dagger = J_-$. As mentioned above, we can then generate all the eigenfunctions of the vector space $|\boldsymbol{J}^2 J_z\rangle$, provided that:

$$|\boldsymbol{J}_z| \leq \sqrt{\boldsymbol{J}^2}\,. \tag{1.109}$$

This condition defines the lower and upper bounds of our newly created space, according to:

$$J_- \,|\boldsymbol{J}^2 J_z^{\downarrow}\rangle = 0 \tag{1.110}$$

$$J_+ \,|\boldsymbol{J}^2 J_z^{\uparrow}\rangle = 0\,. \tag{1.111}$$

By multiplying the first and second equations by J_+ and J_-, respectively, and taking into account that $\boldsymbol{J}^2 - \boldsymbol{J}_z^2 = J_\pm J_\mp \mp J_z$, we obtain:

$$(\boldsymbol{J}^2 - (J_z^{\downarrow})^2 + J_z^{\downarrow})\,|\boldsymbol{J}^2 J_z^{\downarrow}\rangle = 0 \tag{1.112}$$

$$(\boldsymbol{J}^2 - (J_z^{\uparrow})^2 + J_z^{\uparrow})\,|\boldsymbol{J}^2 J_z^{\uparrow}\rangle = 0\,. \tag{1.113}$$

Since the two eigenfunctions are non-zero, the multipliers must be zero. By factoring and setting the difference between these two multipliers to zero, we obtain:

$$(J_z^{\uparrow} + J_z^{\downarrow})(J_z^{\uparrow} - J_z^{\downarrow} + 1) = 0\,. \tag{1.114}$$

As $J_z^{\downarrow} \leq J_z^{\uparrow}$, the left term vanishes. Hence, the second term must necessarily be positive:

$$J_z^{\uparrow} = -J_z^{\downarrow} \qquad\qquad \rightarrow \qquad\qquad J_z^{\uparrow} - J_z^{\downarrow} = 2j\,, \tag{1.115}$$

with $2j$ a positive integer. Summing the eigenvalues of equations 1.112 and 1.113 for a given $\boldsymbol{J}^{2'}$ operator gives:

$$\boldsymbol{J}^2 = j(j+1)\,. \tag{1.116}$$

As a consequence, j_z can only takes integer or half-integer values, i.e. $j_z = m$, with $m = j, j-1, ..., 1, 0, -1, ..., -j$ or $m = j, j-1, ..., \frac{1}{2}, -\frac{1}{2}, ..., -j$. The numbers j and m will then be the quantum numbers corresponding to the eigenfunctions $|\boldsymbol{J}^{2'} J_z'\rangle$. If we move from cartesian to polar coordinates, the operator expressions for a *single mass point* become:

$$J_\pm = e^{\pm i\varphi\left(i\cot\theta\frac{\partial}{\partial\varphi} \pm \frac{\partial}{\partial\theta}\right)} \tag{1.117}$$

$$J_z = -i\frac{\partial}{\partial\varphi} \tag{1.118}$$

$$\boldsymbol{J}^2 = -\Big[\frac{1}{\sin^2\theta}\frac{\partial^2}{\partial\varphi^2} + \frac{1}{\sin\theta}\frac{\partial}{\partial\theta}\Big(\sin\theta\frac{\partial}{\partial\theta}\Big)\Big], \tag{1.119}$$

where r is the radial distance from the origin to the point object, θ is the polar angle of r and φ is the azimuthal angle of r. The eigenfunction has the form given in Figure 1.8.

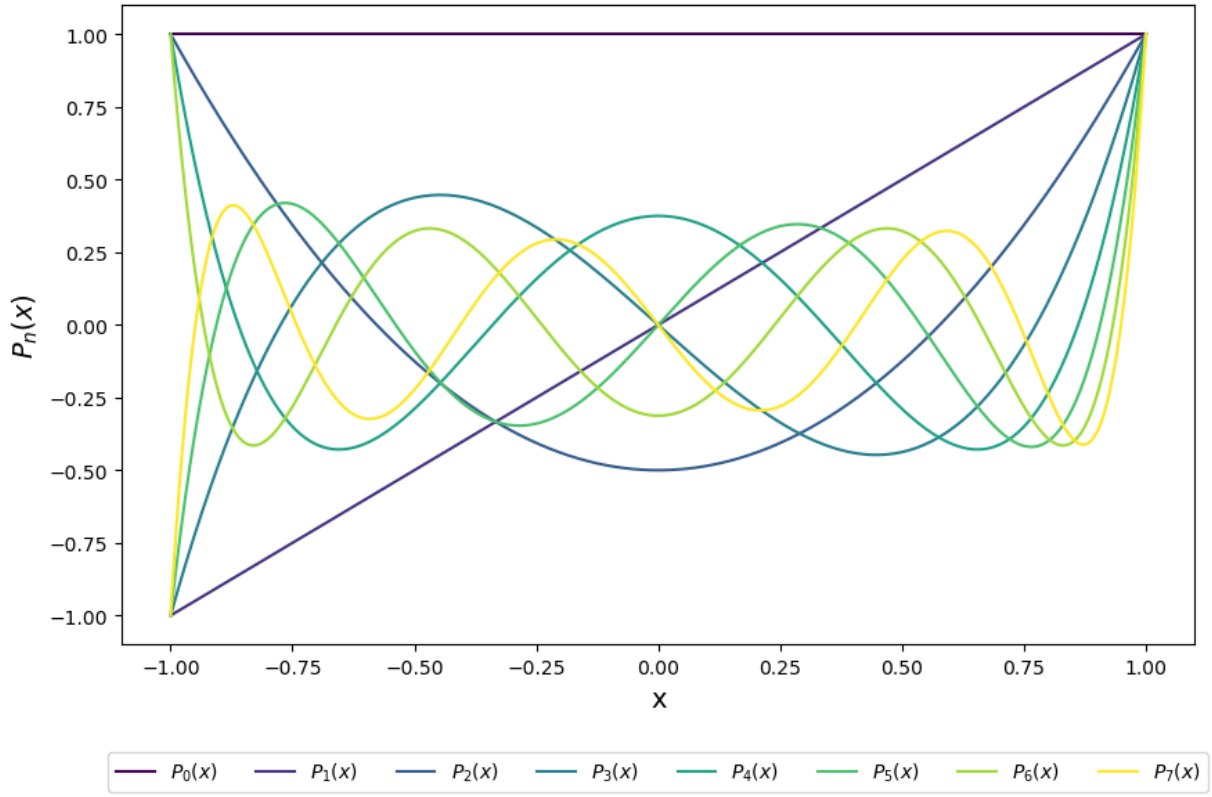

Figure 1.8: $P_n(x)$ Legendre polynomials, for n that goes from 0 to 7. Note how as n increases, the number of modes grow until it tends to the particle in a box case.

$$\Psi = \Theta_{jm}(\theta)\Phi_m(\varphi)\,, \tag{1.120}$$

which, when considering a system formed by several mass points, requires an additional term χ to address for a k dependence, so that $J_c = -i\,\partial/\partial\chi$. This generates a solvable *hypergeometric equation* of the general form:

$$\Psi = \Theta_{jkm}(\theta)\Phi_m(\varphi)e^{ik\chi}\,. \tag{1.121}$$

Let's focus on the simplest case tackled by equation 1.120. The relative eigenvalues are:

$$\boldsymbol{J}^2\,|\Theta_{jm}(\theta)\rangle = j(j+1)\,|\Theta_{jm}(\theta)\rangle \tag{1.122}$$

$$J_z\,|\Phi_m(\varphi)\rangle = m\,|\Phi_m(\varphi)\rangle\,. \tag{1.123}$$

The algebraic structure of $\Phi_m(\varphi)$ that allows the eigenvalues in equation 1.122 to exist is:

$$\Phi_m(\varphi) = \frac{1}{\sqrt{2\pi}}e^{im\varphi}\,, \tag{1.124}$$

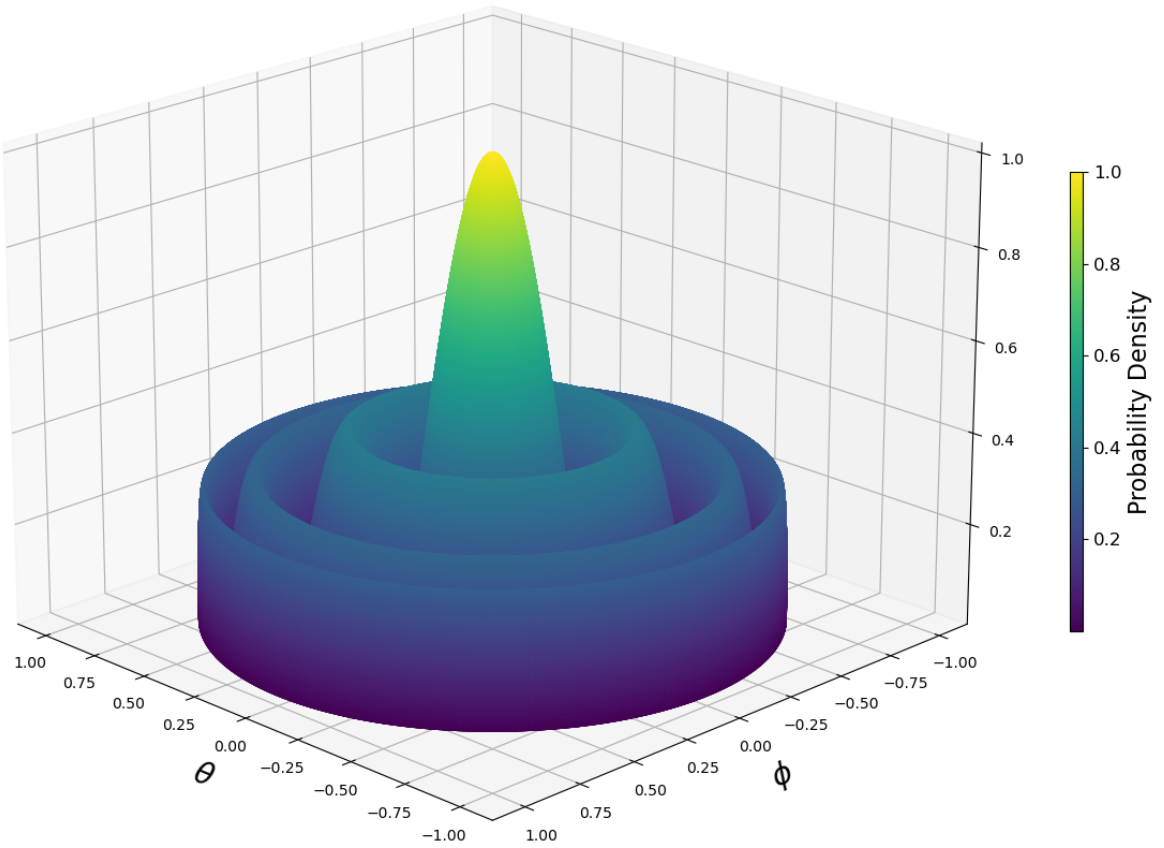

Figure 1.9: Probability density for $P_7(x)$ Legendre's associated polynomials equation with J = 7, m = 0 and k = 0 (refer to 1.120 and 1.126 equations).

while imposing $m = 0, k = 0$ and renaming $cos(\theta) = x$, we can express the $\Theta_{jm}(\theta)$ eigenfunctions of equation 1.123 in the form of the *Legendre polynomials*:

$$\left[(1-x^2)\frac{d^2}{dx^2} - 2x\frac{d}{dx} + j(j+1)\right]y = 0\,, \tag{1.125}$$

whose solutions are represented by the Rodriguez formula:

$$P_n(x) = \frac{1}{2^n n!}\frac{d^n}{dx^n}(x^2-1)^n\,, \tag{1.126}$$

If, for example, we take the equation 1.126 and compute the values for $P_7(x)$ we obtain Figure 1.8, where also other polynomials are displayed. Note how the potential well stands out as the polynomial degree increases. Using Legendre's associated polynomials for $P_7(x)$, we can subsequently visualise the angular probability density of equation 1.125 for $J = 7$, $m = 0$ and $k = 0$. The result is displayed in Figure 1.9.

Now we can think how to solve the rotational eigenvalue equation:

$$H_r\,|E_r\rangle = E_r\,|E_r\rangle\ , \tag{1.127}$$

where, for simplicity, H_r acts on the space $|JK\rangle$, a homogeneous space for which M is omitted. Once the matrix H_r and the corresponding elements on the complete basis sets $\langle JK' | H_r | JK'' \rangle$ are defined, we need to check if the matrix is diagonal. If there are non-diagonal elements, similar to what was done for the equation 1.70, we need to find those sets of eigenvectors for which the new basis function $|J\Gamma\rangle$ becomes diagonal. By linearly combining the original basis function as:

$$|J\Gamma\rangle = \sum_K a_K^J |JK\rangle \ , \tag{1.128}$$

we can finally satisfy the total rotational Hamiltonian:

$$H |J\Gamma\rangle = E(J\Gamma) |J\Gamma\rangle \ . \tag{1.129}$$

1.5.6 Spherical Top, Linear and Symmetric Top rotors

The simplest case among rotors is the spherical top rotor (for this and the following cases, refer to table 1.4). The Hamiltonian and the energy are:

$$H_r = B\boldsymbol{J}^2 \, , \tag{1.130}$$

that has energies:

$$E(JK) = BJ(J+1) \tag{1.131}$$

with each $2J+1$ degenerate level in K and M. Although the Hamiltonian is already diagonal, its spherical form does not admit dipole moments, not allowing transitions between rotational levels[13]. Nevertheless, Watson (1971) and Curl et al. (1973) showed that centrifugal distortions can introduce rotational transitions.

Linear molecules, on the other hand, need two degrees of freedom to be described, and the Hamiltonian takes the form:

$$H_r = B(J_B^2 + J_C^2) = B\boldsymbol{J}^2 \, , \tag{1.132}$$

with energies:

$$E(J) = BJ(J+1) \tag{1.133}$$

where $K = 0$ is non-degenerate for the $2J+1$ level, while it remains degenerate for M.

In symmetric top rotors instead, two moments of inertia are equal and one differ, leading to two different scenarios. The case in which $A > B = C$ is called *prolate*, due to the "cigar shape" of the molecule; the case in which $A = B > C$ is called *oblate*, because the molecule resembles a flattened sphere. In the prolate case, the Hamiltonian is:

$$H_r = AJ_A^2 + B(J_B^2 + J_C^2) \tag{1.134}$$

$$= B\boldsymbol{J}^2 + (A-B)J_A^2 \, , \tag{1.135}$$

and its energies:

$$E(J,K) = BJ(J+1) + (A-B)K^2 \, , \tag{1.136}$$

with each level having a value of $2J+1$, degenerate in M. In the oblate case, A is substituted by C, and J_A^2 by J_C^2.

[13] The physical reason is discussed in the next section.

1.5.7 The Asymmetric Top rotor

In the case of an asymmetric rotor, however, all different moments of inertia ($I_a \neq I_b \neq I_c$) lead to no analytical solution for the Schrödinger equation. The Hamiltonian cannot be formed only by $\boldsymbol{J}^2$ and $\boldsymbol{J}$, which have diagonal solutions in K, but it is anyway possible to expand it in terms of the symmetric top prolate (or oblate) eigenfunctions. The general Hamiltonian can be written as:

$$H_r = \tfrac{1}{2}(a+b)(J_a^2 + J_b^2) + cJ_c^2 + \tfrac{1}{2}(a-b)(J_a^2 - J_b^2) \tag{1.137}$$

$$= \alpha \boldsymbol{J}^2 + \beta J_c^2 + \gamma(J^{+2} + J^{-2}) \tag{1.138}$$

with

$$\alpha = \frac{1}{2}(a+b), \qquad \beta = c - \frac{1}{2}(a+b), \qquad \gamma = \frac{1}{4}(a-b)\,. \tag{1.139}$$

Replacing the indices a, b and c by the respective ordered values A, B and C for the desired molecule, the best suited Hamiltonian has the lowest ratio γ/β. Six different representations can be devised:

Table 1.5: The rotor representation system.

	I^r	I^l	II^r	II^l	III^r	III^l
a	B	C	C	A	A	B
b	C	B	A	C	B	A
c	A	A	B	B	C	C

which, playing with symmetry, substantially reduce to three. To note, as the molecules studied in this work are nearly prolate, only the prolate Hamiltonian with the sole I^r representation is shown.

In general, in order to understand whether an asymmetric rotor can be approximated to a prolate or to an oblate symmetric top, the κ parameter is used:

$$\kappa = \frac{2B - A - C}{A - C} \tag{1.140}$$

whose values span from +1 (when $A = B$, *oblate* case limit) to −1 (when $B = C$, *prolate* case limit). This way two opposite cases are distinguished, and the constant that discriminates among these two values is κ. The prolate Hamiltonian takes then the form:

$$H = \tfrac{1}{2}(A+B)\boldsymbol{J}^2 + \tfrac{1}{2}(A-C)H(\kappa)\,, \tag{1.141}$$

with

$$H(\kappa) = J_A^2 + \kappa J_B^2 + J_C^2\,, \tag{1.142}$$

which is essentially equivalent to $\beta/2\gamma$.

We have seen how a rotational transition depends on molecular geometry, but it is not due to geometry alone: the transition is the result of the radiation-matter interaction. To understand how this happens, we can imagine the energy of a system in an electric field according to the expansion:

$$U = U^0 + \left[\frac{\partial U}{\partial E_i}\right]^0 E_i + \frac{1}{2}\left[\frac{\partial^2 U}{\partial E_i \partial E_j}\right]^0 E_i E_j + \frac{1}{6}\left[\frac{\partial^3 U}{\partial E_i \partial E_j \partial E_k}\right]^0 E_i E_j E_k + ... \tag{1.143}$$

where U^0 is the energy of the molecule in free space given by the field-free Hamiltonian; the second term refers to a linear electric field contribution and the following to non-linear higher-orders. The change caused by the electric field in the molecular energy dU is expressed as:

$$dU = -m_i dE_i \tag{1.144}$$

that compared with equation 1.143 allow us to express the electric dipole moment m_i as:

$$m_i = \mu_i^0 + \alpha_{ij}^0 E_j + \tfrac{1}{2}\beta_{ijk}^0 E_j E_k + ... \tag{1.145}$$

where the permanent dipole moment is $\mu_i^0 = -(\partial U/\partial E_i)^0$, the linear polarisability is $\alpha_{ij}^0 = -(\partial^2 U/\partial E_i \partial E_j)^0$ and the higher orders correspond to higher order polarisabilities[14]. The permanent dipole moment is therefore the term that contributes most to the electric dipole moment and hence to the change in energy of the molecular system. In addition, if we consider that the intensity of a transition measured in absorption is $\propto |\mu|^2$, the importance of the dipole moment becomes even clearer.

If we consider the projection of the principal dipole moment μ_0 along the three inertia axes, we obtain μ_a, μ_b and μ_c, i.e. the dipole moments of an asymmetric top molecule. The absence of a dipole moment along a given axis means that the incident radiation does not produce any transition regarding that direction. Group theory allows us to extend this treatment to the symmetry of the overall wave function, defining what are better known as selection rules, i.e. the transitions allowed according to the system symmetry and its dipole moments. Table 1.6 summarises the transitions allowed along the different axes and introduces the pseudo-quantum numbers K_a and K_c. These two, while not true quantum numbers like $\boldsymbol{J}$ or K, serve as convenient labels for rotational energy levels in asymmetric rotor molecules, and are defined in the vector space τ. Specifically, as K is basically degenerate in an asymmetric rotor, they allow to express the characteristic resumed with the κ parameter: K_a corresponds to the component along the axis of maximum rotational inertia, K_c represents the component along the axis of minimum rotational inertia. Each rotational level is basically split and it is given by $K_a + K_c = J$ or $K_a + K_c = J + 1$. In Figure 1.10 one can see how for a single level J there are $2J + 1$ distinct energies leading to a non-crossing effect of the lines shown. The consequence is that the highest energy level for the prolate limit, $K_a = J$, correlates with the highest energy level of the oblate rotor with $K_c = 0$; conversely, $K_a = 0$ prolate correlates with the lowest energy of the oblate rotor with $K_c = J$.

[14]The same concepts can be extended to the interaction with the magnetic field, with the difference that the electric dipole operator is a *polar* vector, whereas the magnetic dipole operator is an *axial* vector.

Table 1.6: Selection rules for asymmetric top molecules.

Transition	Dipole moment component	ΔK_a	ΔK_c
a-type	$\mu_a \neq 0$	$0, (\pm 2, \pm 4, ...)$	$\pm 1, (\pm 3, \pm 5, ...)$
b-type	$\mu_b \neq 0$	$\pm 1, (\pm 3, \pm 5, ...)$	$\pm 1, (\pm 3, \pm 5, ...)$
c-type	$\mu_c \neq 0$	$\pm 1, (\pm 3, \pm 5, ...)$	$0, (\pm 2, \pm 4, ...)$

Notes. Transitions in brackets are much weaker than the main ones.

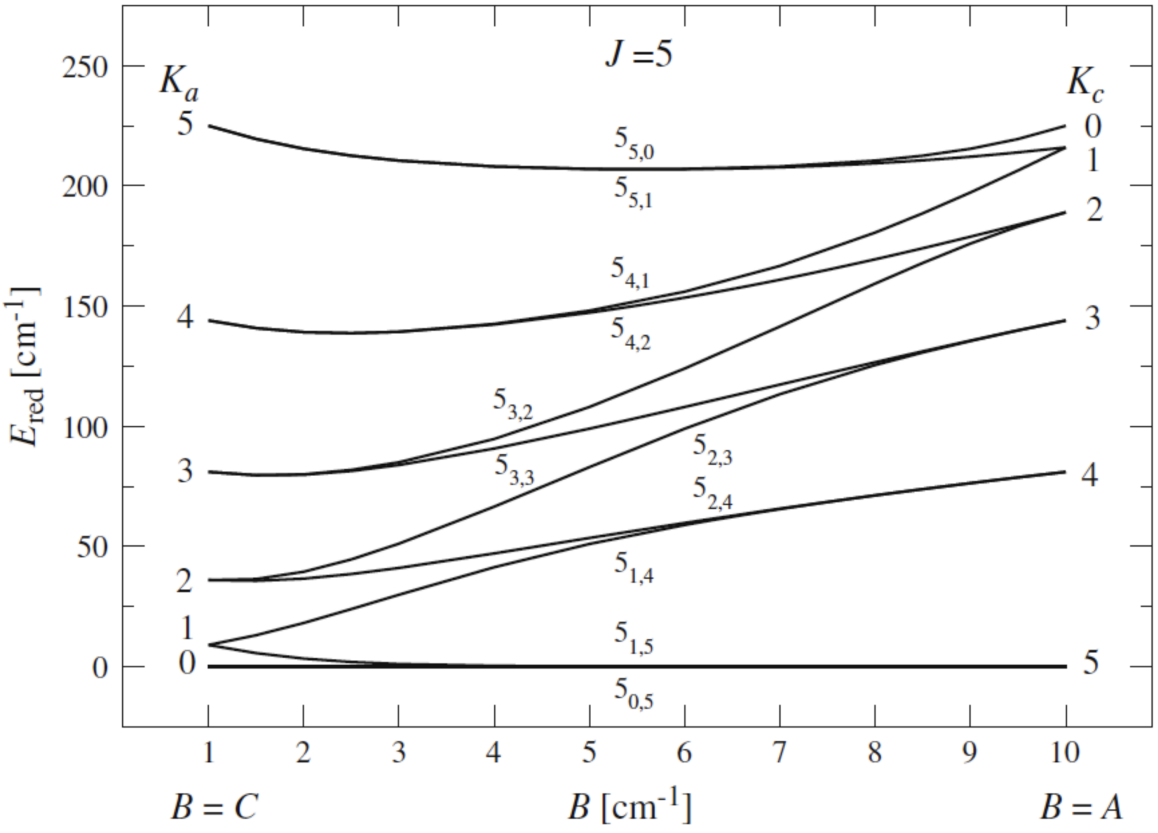

Figure 1.10: Energy levels of an asymmetric top molecule. For $J = 5$, B varies continuously from C (prolate case) to A (oblate case) (Yamada & Winnewisser 1975).

The typical asymmetric rotor energy values of the equation 1.141 can now be expressed in terms of J and τ as:

$$E(J\tau) = \tfrac{1}{2}(A + C)J(J + 1) + \tfrac{1}{2}(A - C)E_{J\tau}(\kappa)\,, \tag{1.146}$$

with $E_{J\tau} = \langle J\tau|\, H(\kappa)\, |J\tau\rangle$. These values can be shown to be:

$$\langle JK|\, H(\kappa)\, |JK\rangle = FJ(J+1) + (G-F)K^2 \tag{1.147}$$

$$\langle JK|\, H(\kappa)\, |JK\pm 2\rangle = H[f(JK\pm 1)]^{1/2} \tag{1.148}$$

$$f(Jk\pm 1) = \tfrac{1}{4}[J(J+1) - K(K\pm 1)][J(J+1) - (K\pm 1)(K\pm 2)] \tag{1.149}$$

where F, G and H are given, restricted to the case of the prolate rotor and the representation I^r, by $\frac{1}{2}(\kappa-1)$, 1, and $-\frac{1}{2}(\kappa+1)$ respectively. The subsequent factorisation of $H(\kappa)$ into four subsets allows the subsequent diagonalisation necessary to obtain the off-diagonal terms, which, if much smaller than the diagonal terms, can be obtained via perturbation theory.

To better understand the nature of the selection rules, see for example the case of the molecules SO_2 and H_2CO, represented in Figure 1.11. For both molecules, which are more or less planar, no transitions along the c-axis are observed, since the dipole moment μ_c does not exist. But in the same way SO_2 has no dipole moment μ_a and H_2CO has no μ_b. Consequently, only b- and a-type transitions are observed for SO_2 and H_2CO, respectively. Table 1.6 summarise this conditions, including the pseudo-quantum numbers K_a and K_c.

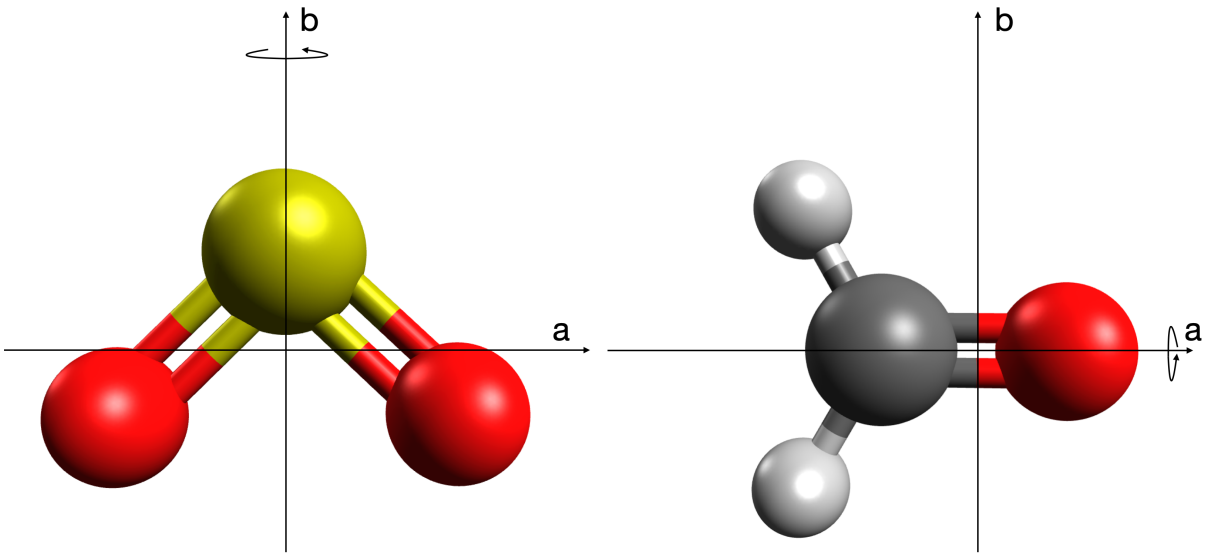

Figure 1.11: From left to right, SO_2 and H_2CO molecules and respective inertia axes. The absence of the μ_a and μ_b dipole moments leads to the appearance of only the b- and a-type transitions, respectively.

1.5.8 The distortable rotor

So far we have assumed that the energy of a rotor can be approximated to that of a rigid body, well described by an harmonic potential. In reality, the model used for the harmonic oscillator does not take into account the effects of bond breaking, non-zero transition probabilities for the

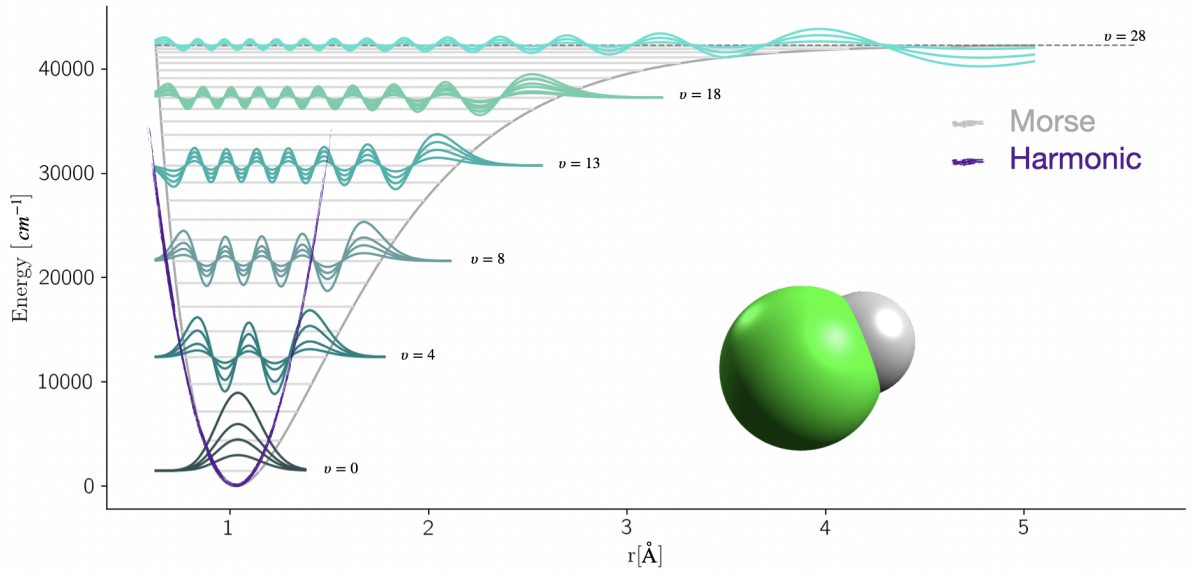

Figure 1.12: Comparison of harmonic and Morse potentials for the ground electronic state of $H^{35}Cl$ (equilibrium bond length $r_e = 1.27455$Å). The υ vibrational levels span from zero to the dissociation energy ($\upsilon \approx 30$). Figure obtained by modifying the code of Hill 2019.

overtone and combination bands, and the anharmonicity of real bonds. In particular, for a given vibrational state, rotation distorts the molecular inertia moments, changing the values of the rotational constants. For this reason, it would be preferable to use the Morse potential, an inter atomic interaction model for the molecular potential energy. The Morse function for a diatomic molecule is given by:

$$V(r) = D\left(1 - e^{-a(r-r_0)}\right)^2 , \tag{1.150}$$

where V is the potential energy at the point r, D is the dissociation energy, a is a parameter that affects the slope of the curve, and r_0 is the equilibrium position. In the figure 1.12 we can clearly see how the harmonic potential differs from the Morse potential. Nevertheless, for low vibrational states it is still preferable to use the harmonic potential, correcting it by introducing terms higher than the sole quadratic. In essence, this allows the potential to be computed in a reasonable amount of time while still obtaining results in agreement with experimental results. In particular, this approach is well suited to the work presented in this thesis, where although the energy of different vibrational levels has been calculated, more attention has been paid to the ground vibrational state.

These distortion effects can be taken into account by centrifugal distortion coefficients that can be relate to the vibrational potential constants, and can therefore be used to fit the experimental rotor data in a useful way (Watson 1967). It is convenient to think about the distorted

Hamiltonian as the sum of three contributions:

$$H = H_r + H_d^4 + H_d^6\,, \tag{1.151}$$

where H_r stays for the rigid rotor Hamiltonian, H^4 and H^6 to the Hamiltonians including the fourth and sixth power components of the angular momentum. These two latter are given respectively by:

$$H_d^4 = \frac{\hbar}{4}\sum_{\alpha\beta\gamma\delta}\tau_{\alpha\beta\gamma\delta}J_\alpha J_\beta J_\gamma J_\delta \tag{1.152}$$

$$H_d^6 = \hbar\sum_{\alpha\beta\gamma\delta\epsilon\eta}\tau_{\alpha\beta\gamma\delta\epsilon\eta}J_\alpha J_\beta J_\gamma J_\delta J_\epsilon J_\eta\,, \tag{1.153}$$

where α, β, γ, δ, ϵ, $\eta = x, y$ or z axes. τ_s are the centrifugal distortion constants, where the sum of the number of subscripts distinguishes between quartic and sextic coefficients. Further extensions include the addition of octic and dectic terms, but the concept remains the same.

For asymmetric rotors these τ constants give a total of 81 quartic and 729 sextic coefficients. However, by using unitary transformations like the one in equation 1.71, Watson (1977) was able to reduce τ coefficients to 105, describing the distorted Hamiltonian by distinguishing two cases.

In the first case, Watson employed a unitary transformation that imposing $R_6 = 0$ ($R_6 = \frac{\hbar^4}{64}\{\tau_{xxxx} + \tau_{yyyy} - 2(\tau_{xxyy} + 2\tau_{xyxy})\}$, extensively explained in Gordy & Cook (1984)) eliminated the matrix elements $K \pm 4$. The unitary matrix s_{111} in this case becomes:

$$s_{111} = -\frac{4R_6}{B - C}\,, \tag{1.154}$$

with B and C the rotational constants relative to the reduction employed (refer to Table 1.5). This approach is known as the *A-Watson reduction* and was the first reduction to be extensively used. The Hamiltonian 1.151 then takes the form:

$$H^{(A)} = H_r + H_d^4 + H_d^6\,, \tag{1.155}$$

with:

$$\begin{aligned} H_r &= B^{(A)}J_x^2 + C^{(A)}J_y^2 + A^{(A)}J_z^2 \\ &= \tfrac{1}{2}(B^{(A)} + C^{(A)})J^2 + [A^{(A)} - \tfrac{1}{2}(B^{(A)} + C^{(A)})]J_z^2 + \tfrac{1}{2}(B^{(A)} - C^{(A)})(J_x^2 - J_y^2) \end{aligned} \tag{1.156}$$

$$H_d^4 = \Delta_J J^4 - \Delta_{JK}J^2J_z^2 - \Delta_K J_z^4 - 2\delta_J J^2(J_x^2 - J_y^2) - \delta_K[J_z^2(J_x^2 - J_y^2) + (J_x^2 - J_y^2)J_z^2] \tag{1.157}$$

$$\begin{aligned} H_d^6 &= \Phi_J J^6 + \Phi_{JK}J^4J_z^2 + \Phi_{KJ}J^2J_z^4 + \Phi_K J_z^6 + 2\phi_J J^4(J_x^2 - J_y^2) \\ &\quad + \phi_{JK}J^2[J_z^2(Jx^2 - J_y^2) + (J_x^2 - J_y^2)J_z^2] + \phi_K[J_z^4(J_x^2 - J_y^2) + (J_x^2 - J_y^2)J_z^4]\,, \end{aligned} \tag{1.158}$$

where Δ_J, Δ_{JK}, Δ_K, δ_J and δ_K are the quartic and Φ_J, Φ_{JK}, Φ_{KJ}, Φ_K, ϕ_J, ϕ_{JK} and ϕ_K are the sextic distortion constants (octic and dectic constants along with all relations with τ_s can be found in Gordy & Cook 1984.)

The other reduction, known as the *S-Watson reduction*, was firstly derived due to the some difficulties in dealing with slightly asymmetric top rotors in the *A* formalism. In particular, when

B and C constants have similar values, the s_{111} unitary matrix get larger, undermining the initial assumptions that allowed off-diagonal matrix elements to be treated as small perturbations. The issue was overcame by imposing $R_5 = 0$ ($R_5 = -\frac{\hbar^4}{32}\{\tau_{xxxx} - \tau_{yyyy} - 2(\tau_{xxzz} + 2\tau_{xzxz}) + 2(\tau_{yyzz} + 2\tau_{yzyz})\}$, extensively explained in Gordy & Cook (1984)). In this case, the unitary matrix s_{111} becomes:

$$s_{111} = \frac{2R_5}{2A - B - C}\,, \tag{1.159}$$

leading to the formulation of the Hamiltonian in the S reduction as:

$$H^{(A)} = H_r + H_d^4 + H_d^6\,, \tag{1.160}$$

with:

$$\begin{aligned} H_r &= B^{(S)}J_x^2 + C^{(S)}J_y^2 + A^{(S)}J_z^2 \\ &= \tfrac{1}{2}(B^{(S)} + C^{(S)})J^2 + [A^{(S)} - \tfrac{1}{2}(B^{(S)} + C^{(S)})]J_z^2 + \tfrac{1}{4}(B^{(S)} - C^{(S)})(J_+^2 - J_-^2) \end{aligned} \tag{1.161}$$

$$H_d^4 = -D_J J^4 - D_{JK} J^2 J_z^2 - D_K J_z^4 - d_1 J^2(J_+^2 + J_-^2) - d_2(J_+^4 - J_-^4) \tag{1.162}$$

$$\begin{aligned} H_d^6 &= H_J J^6 + H_{JK} J^4 J_z^2 + H_{KJ} J^2 J_z^4 + H_K J_z^6 + h_1 J^4(J_+^2 + J_-^2) \\ &\quad + h_2 J^2(J_+^4 + J_-^4) + h_3(J_+^6 + J_-^6)\,, \end{aligned} \tag{1.163}$$

It should be noted that although these differences have to be taken into account, the advancement in computational power makes it possible to overcome some of the issues encounter in the fitting procedure. When the asymmetry is not that pronounced, it is today possible to obtain satisfactory results even when a different reduction would in principle be preferred. It must be stressed that, provided the mean square error deviations of the fits are kept congruent, the use of one reduction rather than another does not lead to incorrect results. What is important is to obtain a mathematical object that succeeds in describing the rotational behaviour of a molecule that might be of astrochemical interest. The goal is to generate a reliable catalogue of the molecular transitions to be able to guide the spectral analysis of ISM sources, despite the formalism employed.

1.5.9 Nuclear Quadrupole Hyperfine interactions

In order to be able to assign the spectra recorded in the experiments carried out for this thesis, it was necessary to take into account also the nitrogen atom spin angular momentum. Its nature, like that of all atoms having a nuclear spin ≥ 1, produces some peculiar line splitting which can facilitate the spectral line assignment. In order to grasp the nature of the *nuclear quadrupole hyperfine interaction* with the overall molecular rotation, a small theoretical introduction is provided below.

In general, an electric non-polarised charge having a distribution $\rho(r)$ interacts with an electric potential $V(r)$ according to:

$$H_Q = \int \rho(r)V(r)d\tau\,. \tag{1.164}$$

Expanding $V(r)$ in space-fixed coordinates, we can express it as:

$$V(r) = V^{(0)} + \sum_i r_i \left(\frac{\partial V}{\partial r_i}\right)_0 + \frac{1}{2!}\sum_{ij} r_i r_j \left(\frac{\partial^2 V}{\partial r_i \partial r_j}\right)_0 + ... \tag{1.165}$$

$$= V^{(0)} + \sum_i r_i V_i^{(1)} + \frac{1}{2!}\sum_{ij} r_i r_j V_{ij}^{(2)} + ..., \tag{1.166}$$

which leads to:

$$H_Q = V^{(0)} \int \rho(r) d\tau + \sum_i V_i^{(1)} \int \rho(r) r_i d\tau + \frac{1}{2!}\sum_{ij} V_{ij}^{(2)} \int \rho(r) r_i r_j d\tau + ... \tag{1.167}$$

Defining F_i as the i-rank tensor that describes the integral of the $\rho(r)$ distribution over space, we can rewrite the latter equation as:

$$H_Q = V^{(0)}F^{(0)} + V_i^{(1)}F_i^{(1)} + \frac{1}{2}V_{ij}^{(2)}F_{ij}^{(2)} + \frac{1}{6}V_{ijk}^{(3)}F_{ijk}^{(3)} + ... \tag{1.168}$$

where the first term refers to the energy of a charge q in a uniform potential, the second to the scalar product between the gradient of the potential field and its dipole moment μ_i (also known as the *Stark energy term*), and the third to the second-rank tensor $V_{ij}^{(2)}F_{ij}^{(2)}$ which describes the interaction between the electric quadrupole moment and the field gradient. It is possible to decompose $V_{ij}^{(2)}$ and $F_{ij}^{(2)}$[15] in zero, first and second-order tensors, but since we are interested in the interaction energy given by the scalar product between $V_{ij}^{(2)}$ and $F_{ij}^{(2)}$, we will look at the zero-rank tensor only.

The fact that the S electrons have a non-negligible spherically symmetric charge distribution and that the potential outside the nucleus is zero (Laplace equation, $\nabla^2 V = 0$) allows us to not consider the interaction energy given by the multiple combination of traces. As the same tensorial anti-symmetric components of $V_{ij}^{(2)}$ and $F_{ij}^{(2)}$ go to zero ($[r_i, r_j] = 0$ and $\partial^2 V/\partial r_i \partial r_j - \partial^2 V/\partial r_i \partial r_j = 0$), what remains is the orientation dependent interaction energy, given by the Hamiltonian:

$$H_Q = \frac{1}{2}\sum_{ij} V_{ij}^{(2)} F_{ij}^{(2)}, \tag{1.169}$$

where

$$F_{ij}^{(2)} = \int \rho(r)\left[\tfrac{1}{2}(r_i r_j + r_j r_i) - \tfrac{1}{3}\mathbf{r}^2\delta_{ij}\right] d\tau, \tag{1.170}$$

By defining $3F_{ij} = Q_{ij}$ and identifying in Q_{ij} the *quadrupole moment tensor*, we can re-express equation 1.169 as:

$$H_Q = \frac{1}{6}\sum_{ij} V_{ij}^{(2)} F_{ij}^{(2)}, \tag{1.171}$$

[15]The tensors $V_{ij}^{(2)}$ and $F_{ij}^{(2)}$ can be decomposed according to the general cartesian second-rank tensor $T_{ij} = \frac{1}{3}\delta_{ij}T^t + T_k^a + T_{ij}^s$, where T^t stands for the trace of T_{ij}, T_k^a for the asymmetric traceless second-rank tensor and T_{ij}^s for the traceless symmetric tensor.

for which

$$Q_{ij}^{(2)} = \int \rho(r)[3r_i r_j - \mathbf{r}^2\delta_{ij}]d\tau\,. \tag{1.172}$$

Defining the *total angular momentum* $\boldsymbol{F}$ as:

$$\boldsymbol{F} = \boldsymbol{I} + \boldsymbol{J}\,, \tag{1.173}$$

and applying the Wigner-Eckart theorem (Rose 1957), it is possible to rewrite the quadruple Hamiltonian to include the atomic spin tensor $\boldsymbol{I}$ and the angular momentum operator $\boldsymbol{J}$. H_Q then becomes:

$$H_Q = \tfrac{1}{6}C_I C_J[\tfrac{3}{2}(I_iI_j + I_jI_i) - \boldsymbol{I}^2\delta_{ij}][\tfrac{3}{2}(J_iJ_j + J_jJ_i) - \boldsymbol{J}^2\delta_{ij}]\,, \tag{1.174}$$

with $C_I = eQ/I(2I-1)$, $C_J = q_J/J(2J-1)$ and q_J the value of the molecular field gradient in the z-direction. Further adjusting equation 1.174, we can obtain the quadrupole Hamiltonian:

$$H_Q = \frac{1}{2}\frac{eQq_J}{I(2I-1)J(2J-1)}\left[3(\boldsymbol{I}\cdot\boldsymbol{I})^2 + \frac{3}{2}(\boldsymbol{I}\cdot\boldsymbol{I}) - (\boldsymbol{I}^2\boldsymbol{I}^2)\right], \tag{1.175}$$

whose relative energies are given by the general formula:

$$E_Q = \frac{Y(JIF)}{J(J+1)}\left[\chi_{aa}\left(J(J+1)+E(\kappa)-(\kappa+1)\frac{\partial E(\kappa)}{\partial\kappa}\right)+2\chi_{bb}\frac{\partial E(\kappa)}{\partial\kappa}+\chi_{cc}\left(J(J+1)-E(\kappa)+(\kappa-1)\frac{\partial E(\kappa)}{\partial\kappa}\right)\right], \tag{1.176}$$

where the traceless element $\chi_{xx} = eQq_x$, with x referring to a, b, c axes, and $Y(JIF)$ the Casimir's function:

$$Y(JIF) = \frac{\frac{3}{4}C(C+1) - I(I+1)J(J+1)}{2I(2I-I)(2J-1)(2J+3)} \tag{1.177}$$

whose values can be find in Townes & Schawlow (1975).

1.6 Experimental details

The experiments performed and described in this thesis have been carried out at the Center for Astrochemical Studies (CAS) of the Max Planck Institute für extraterrestrische Physik in Garching (Germany), employing the CASAC (CAS Absorption Cell) frequency modulation spectrometer[16]. In section 1.6.1 we give a brief introduction to the CASAC experiment, focusing on pyrolysis and DC discharge, operating principles behind the detector and pressure gauges. In section 1.6.2 the modulation technique is shortly addressed, in section 1.6.3 we introduce the major broadening effects and in section 1.6.4 we describe what lies behind the intensity of a molecular transition.

1.6.1 The CASAC experiment

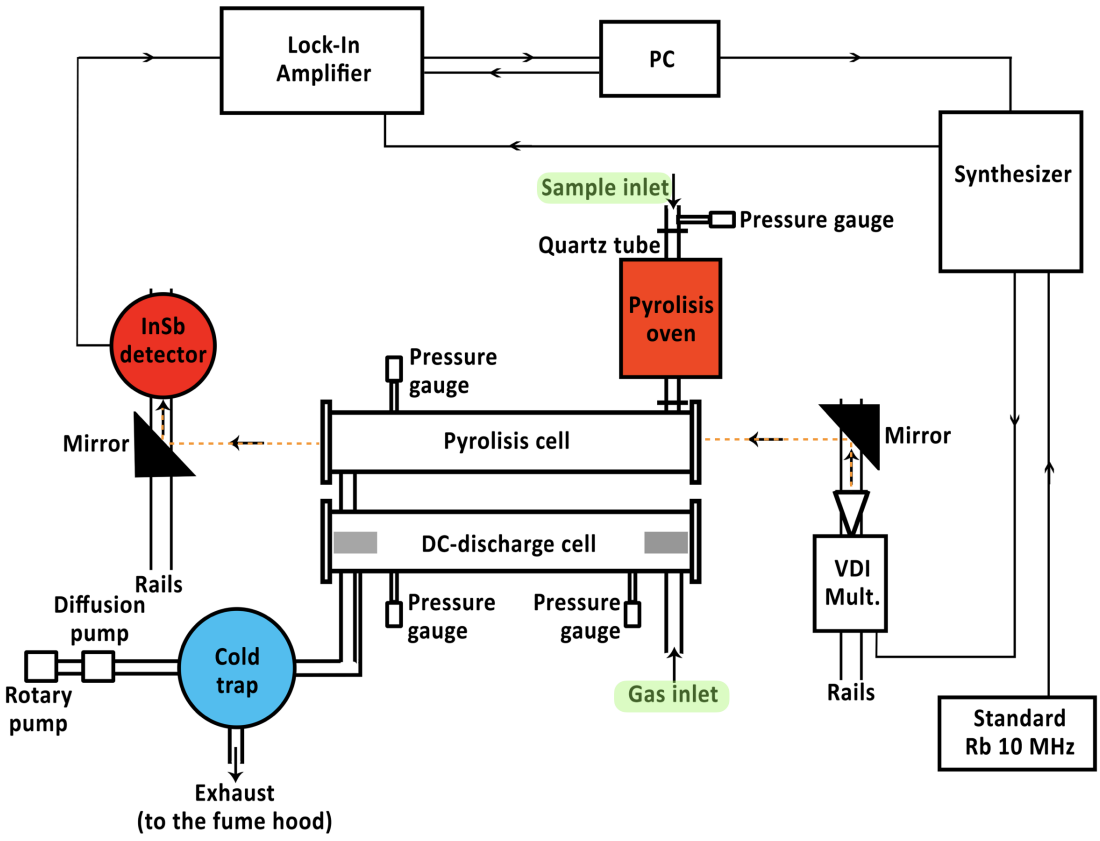

Figure 1.13: The CASAC Experiment, courtesy of Prudenzano 2020.

The CASAC experiment, schematically shown in Figure 1.13, is based on an absorption millimetre/sub-millimetre wave (mm/sub-mm) spectrometer. It is equipped with two Pyrex cells, each 3 m long

[16]For the work presented in the chapter 2, the information on the Bologna's frequency modulation mm/sub-mm wave spectrometer can be found in section 2.2.2 and in more detail in Melosso et al. 2019a,b.

and 5 cm in diameter, maintained at high-vacuum (down to 10^{-4} Torr) by a pumping station provided with rotary and diffusion pumps. Multiple valves allow the gas flow to be adjusted, to use the required cell or to isolate it from the pumping system. If needed, a cold trap can be filled with liquid nitrogen to effectively capture residual vapours.

The experiment begins when the vapours of the chemical species under investigation enter the cell, where light-matter interaction actually takes place. Most of the species of interstellar interest are unstable under room temperature conditions and have to be synthesised *in situ*. This is precisely why the experiment is carried out in flow conditions, so that a freshly synthesised sample is always available to be analysed. The choice of cell merely depends on the molecular species of interest, i.e. the production technique required to produce it: via *pyrolysis* or *DC-discharge*. A third investigation scenario comprise of neutral molecules that can simply be fed into the cell without further processing, and in this case the pyrolysis cell with the oven switched off is employed.

- Pyrolysis: the sample (or precursor) is loaded onto the free-end of a quartz tube and vapours are let through an electric furnace (*Carbolite Gero*) to produce the pyrolysed chemicals. The electric furnace can reach temperatures of up to 1600 °C and the temperature is tuned to maximise the production of the molecule of interest. The flow of precursor vapours can be adjusted by means of a pressure valve and the pressure can be measured at the entrance of the electric furnace by a manometer. The quartz tube connects the newly synthesised furnace products to the absorption cell (*Pyrolisis cell* in the figure 1.13). The routine pressure conditions are usually between 0.1 and 1 mTorr. This technique is mainly used for the production of semi-stable molecules, but for more exotic species such as radicals and ions it is not particularly suited and the DC-discharge technique is preferred.

- DC-discharge: as for the pyrolysis setup the sample is produced in situ, but here the products are generated by low-pressure Direct Current (DC) discharge. Few types of discharge regimes can be distinguished, briefly illustrated in Figure 1.14. A dark *Townsend* discharge is obtained when high voltage ($\sim 600V$) and resistance of ~ 1 MΩ accelerate the gas electrons causing ionisation and discharge current of a few μA. To increase the current to the mA range, the resistance must be reduced for the same voltage. *Sub-normal luminescence* (or glow) appears as secondary electrons, released by hitting cathode cations, increase the number of free electrons in the cell. Excessive resistance reduction lead to increase in the discharge current, entering in the *anomalous* discharge regime.

  The most commonly used regime, the *normal glow* one, is shown in Figure 1.15 and has a $\sim$ constant low voltage DC and currents between tenths of mA and $\sim$ 200 mA (circled area in the Figure 1.14). The cathode, also known as *Aston dark space*, sees secondary electrons generated through cation impacts with the cathode to be sufficiently excited to transfer this energy to other species without production of light. Moving away from the cathode (to the right in Figure 1.15), the electron density increases, resulting in a decreased electric field but an increased cation-electron recombination. As a consequence, the *negative glow* region appears to be the brightest area of the cell. Going even further right we come to

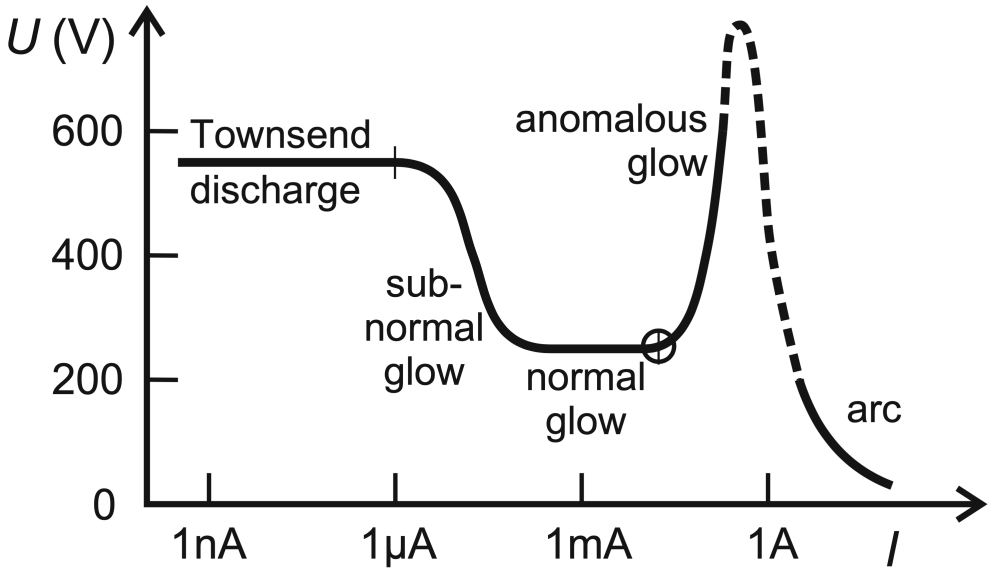

Figure 1.14: Self-sustaining discharge. The reduction in resistance generates three distinct discharge modes. To note, the arc discharge has a negative differential resistance (Piel 2017).

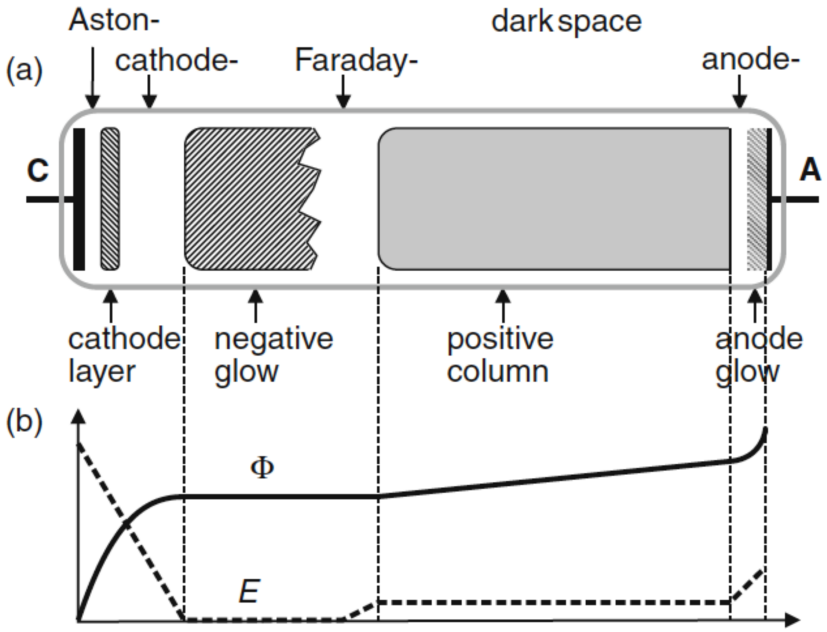

Figure 1.15: [a] Glow discharge in a cell tube with plane cathode (C) and anode (A). [b] Electric potential Φ and axial electric field E variation in the normal regime. (Piel 2017).

the anode, or *Faraday Dark Space*, where the the low density of electrons decrease the electron density increasing ion production, here the highest of the overall cell.

Once the molecular species are produced, additional pressure valves provides further adjustments to the pressure, generally kept between 0.5 mTorr and 10 mTorr (routine experiment conditions). In this experimental setup we employed *Full-range* and *Baratron* manometers. These pressure gauges differ mainly in the pressure range they can measure and in the associated sensitivities: while the former allow to monitor wider pressure ranges at lower sensitivity, the latter are very sensitive but can be used in specific pressure regimes.

Baratron manometers use two electrodes placed between a membrane, in contact with the environment to be measured, to create a capacitor. As the gas pressure increases (or decreases), the membrane slightly deforms, inducing changes in the distance between the electrodes and thus the electrical capacitance of the capacitor. A calibration curve then relates the *capacitance* (from which these methods owe their name) to the relative pressure.

Full-range pressure gauges, on the other hand, use two measuring systems that operate with different measuring approaches at certain pressure values: a *cold cathode* and a *Pirani* method.

- A cold cathode ionisation gauge consists of a cathode and an anode between which a high voltage is applied via a series resistor. Negatively charged electrons leave the cathode by field emission and travel at high speed from the cathode to the anode, ionising the neutral gas molecules and igniting a gas discharge. A calibration curve relates the measured gas discharge current to pressure.

- At pressures of $\sim 10^{-1}$ mbar (1 mbar = 0.75 Torr) the Pirani component comes into operation, measuring pressure generally down to 10^{-3} mbar or less. In this case, a heated filament is used to measure the thermal conductivity of the gas that, with a calibration curve, is related to the pressure.

With reference to Figure 1.13, the microwave signal, generated by a synthesizer (*Keysight E8257D*) operating in the cm-wave range (250 kHz to 67 GHz), is internally modulated employing an external 10 MHz reference provided by an atomic rubidium standard (*Stanford Research Systems*). The probing signal is multiplied through a *Virginia Diodes* VDI multiplier chain, extending the coverage from 82 to 1600 GHz. The generated (in-coming) beam is focused by a parabolic mirror and, passing through a transparent high density polyethylene window, enters the absorption cell and interacts with the flowing gas. Another parabolic mirror at the end of the cell focuses the out-coming signal to the compound parabolic concentrator (CPC, also known as *Winston-cone*) of a Dry InSb hot electron bolometer (*QMC Instruments Ltd*) kept at an operating temperature of 4 K. The working principle of the bolometer is based on the weak electron-phonon interactions that the mm/sub-mm wavelength radiation produces at the InSb lattice. Namely, the incident radiation drives the electrons out of thermal equilibrium of the semiconductor, increasing its temperature. With a calibration curve, the temperature is then correlated to the incident radiation and the signal can be detected and demodulated at twice the modulation frequency (2f, with f staying for the modulation frequency) by the lock-in amplifier. 1f modulation can also be performed, but while it allows to mainly remove the baseline, the 2f modulation further reduce baseline and other instrumental contributions that are linearly time dependent.

1.6.2 Frequency modulation principles

The main reason to employ the modulation technique is the need to reduce background noises, which significantly affect signal quality, especially when measuring weak rotational transitions. To note, detected signals can be of the order of hundreds nV: even the smallest amount of noise will not allow the transitions to be distinguished from the noise.

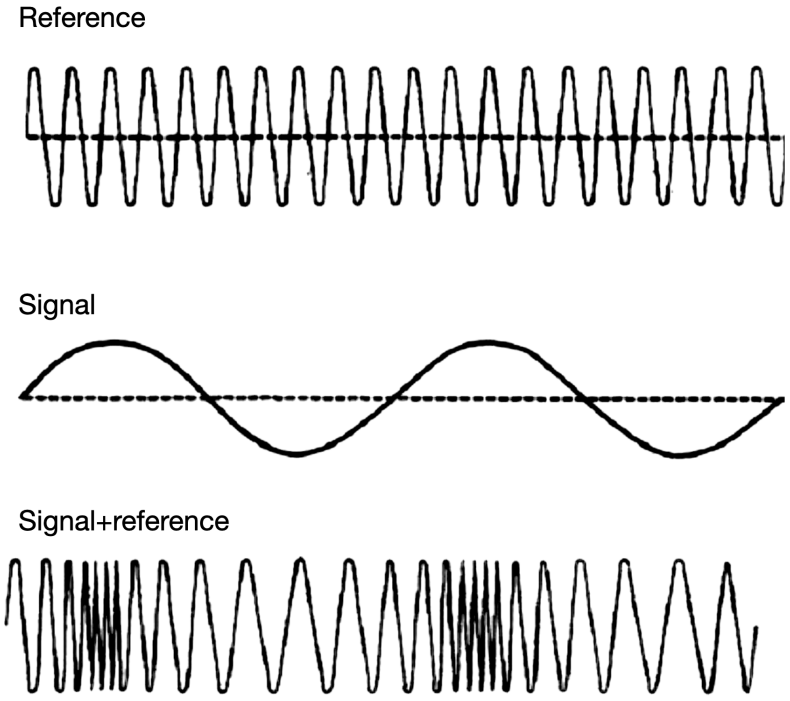

Figure 1.16: The principle behind the modulation technique. The sine *reference* and the *signal* waves are synthesizer generated. The in-coming radiation is the resultant of the sum of the two.

In general, lock-ins use the technique of phase-sensitive detection to distinguish signal components from those of a reference signal of fixed phase and frequency (herein provided by the synthesizer). The practical advantage is that by comparing the collected signal with the reference signal, it is possible to filter out all contributions that are not due to the signal itself, thus eliminating noise sources and significantly increasing sensitivity. Let's assume the synthesizer produces a *reference* sine wave $V_L sin(\omega_L t + \theta_{ref})$ and a *signal* sine wave $V_{sig} sin(\omega_r t + \theta_{sig})$. A representation is given in figure 1.16. The output signal from the detector is an AC signal given by the product of the two wave functions:

$$V = V_{sig} V_L sin(\omega_r t + \theta_{sig}) sin(\omega_L t + \theta_{ref}) \tag{1.178}$$

$$= \tfrac{1}{2} V_{sig} V_L cos([\omega_r - \omega_L]t + \theta_{sig} + \theta_{sig} - \theta_{ref}) - \tfrac{1}{2} V_{sig} V_L cos([\omega_r + \omega_L]t + \theta_{sig} + \theta_{ref}) \tag{1.179}$$

which gives two different signals, one given by the difference $(\omega_r - \omega_L)$ and the other by the sum $(\omega_r + \omega_L)$ of the frequencies. By using a low pass filter, the AC signal is completely removed and

the output signal equals to zero unless ω_L equals to ω_r. Only in this case a DC signal proportional to the signal amplitude is measured, whose relation is given by the equation:

$$V = \tfrac{1}{2} V_{sig} V_L cos(\theta_{sig} - \theta_{ref}) \,. \tag{1.180}$$

As a result, only the signal whose frequency is very close to the reference frequency is detected, eliminating most of noise contributions.

Concluding, the main advantage of the frequency modulation technique is the reduction of most of the noise contributions like the 1/f noise (also known as pink or flicker noise) that, filtered out, lead to very sensitive, low-noise spectra.

1.6.3 Line shapes and line widths

Since we mentioned the concept of line profile, we cannot avoid not dealing with the topic of line shapes and line widths. In this section we introduce the reader to the physical processes that lead to different line profile shapes.

We have seen that, as a result of the light-matter interaction in the microwave regime, molecules with a dipole moment exhibit rotational transitions that can be measured with our experimental apparatus. The time-dependent Schrödinger equation can be expressed as:

$$i\hbar \frac{\partial \Psi}{\partial t} = (H_0 + V)\Psi \,, \tag{1.181}$$

where H_0 is the time-independent Hamiltonian and V the time-dependent potential for the wave function:

$$\Psi = \sum_m a_m(t)\psi_m \,, \tag{1.182}$$

with:

$$i\hbar \frac{\partial}{\partial t}\psi_m = H_0\psi_m \qquad\qquad \psi_m \equiv |m\rangle \, e^{-(i/\hbar)/E_m t} \,. \tag{1.183}$$

This let us to define the coefficient $a_m(t)$ as the time-dependent population factor for the steady state $|m\rangle$. By imposing the frequency of the incident radiation to be equal to the radiation required to pass between the two states n and m (resonant radiation) as:

$$\bar{\omega} = \bar{\omega}_{nm} \,, \tag{1.184}$$

where $\bar{\omega}_{nm} = (E_n - E_m)/\hbar$, after some manipulation we can express the probability $|a_n(t)|^2$ that a system in the state $|n\rangle$ at time $t = 0$ passes at a time t to the state $|m\rangle$ as:

$$|a_n(t)|^2 = \hbar^{-2}|V^0_{nm}|^2 t\delta(\omega_{nm} - \omega) \,, \tag{1.185}$$

where V^0_{nm} is the field dependent energy component between the two states n and m, δ is the *Dirac function* associated to the two states (in the ideal case the resonance frequency) and ω is now in Hz (note the dropped bar). This assumes that we have a function of zero width and zero unit

area, which is physically unreal and better described by a line-shaped function associated to the spontaneous emission lifetime (whose width is better known as *natural line width*). Nevertheless, since the latter is of the order of 10^{-6} Hz for microwave radiation, we can safely approximate it to a Dirac's delta. Assuming the frequencies generated by the synthesizer and the lock-in are perfectly stable, the main processes leading to line profile broadening in experimental conditions are caused by *modulation*, *pressure*, *Doppler* and *saturation* effects.

Pressure, the result of molecular collisions within the cell, is the factor that most affects the line profile in microwave spectroscopy. The line-shape function affected by pressure broadening is given by:

$$S(\omega, \omega_0) = \frac{\omega}{\pi\omega_0}\left[\frac{\Delta\omega}{(\omega_0 - \omega)^2 + (\Delta\omega)^2} + \frac{\Delta\omega}{(\omega_0 + \omega)^2 + (\Delta\omega)^2}\right], \tag{1.186}$$

where $\Delta_\omega = 1/2\pi\tau$, with the average collision time τ between two molecules and ω_0 the resonance frequency. For microwave and IR regimes, where $\Delta_\omega \ll \omega$ and $\omega \sim \omega_0$, equation 1.186 reduces to:

$$S(\omega, \omega_0) = \frac{1}{\pi}\left[\frac{\Delta\omega}{(\omega_0 - \omega)^2 + (\Delta\omega)^2}\right], \tag{1.187}$$

i.e. a *Lorentzian function*, where Δ_ω is the FWHM. In general, for transitions where spontaneous emission can be neglected and with energy less than kT, we can express the intensity of the transition as:

$$\gamma(\omega) = \gamma(\omega_{nm}) S(\omega, \omega_0) \tag{1.188}$$

$$= \frac{8\pi^3}{3ckT}\frac{N f_m \omega^2}{g_m} |\langle n|\boldsymbol{\mu}|m\rangle|^2 S(\omega, \omega_0), \tag{1.189}$$

where

$$f_m = \frac{N_m}{N} = g_m \frac{e^{-\beta E_m}}{Q} \qquad Q = \sum_m g_m e^{-\beta E_m}, \tag{1.190}$$

with f_m the fractional population of the m^{th} state (analogously to equation 1.45), E_m the energy of the m^{th} above the ground state, $\beta = 1/kT$, h/kT or hc/kT depending on whether ω is in energy units, Hz or cm^{-1}, and g_m the m state degeneracy and Q the partition function[17]. We can therefore see how, by reducing the pressure, the line width is reduced to the point where it is the relative speeds between the radiation and the molecules that cause the line to broaden. The latter case is better known as the Doppler broadening effect.

Under standing wave conditions, a broadened Doppler line centred on the frequency ω_0 will cause all molecules moving perpendicular to the standing wave to absorb the energy with frequency ω_0. However, for those moving parallel to the standing wave (say along the υ_z direction) if there is enough power available, there will be an absorption for each passage of the radiation until the line reaches saturation. This technique is called *Lamb dip*, and allows to pass from a Doppler regime to a *sub-Doppler* regime, a phenomenon that induces the appearance of a dip

[17]For a wave function comprising of an electronic, vibrational, rotational, and nuclear spin contribution $\Psi_m = \Psi_e\Psi_\upsilon\Psi_r\Psi_{ns}$, the total fractional population is $f_m = f_e f_\upsilon f_r f_{ns}$.

on the line profile at the resonance frequency ω_0. This technique was also used in chapter 3 to resolve several components that in the routine Doppler regime were unresolved.

Finally, high-power pumping techniques that overpopulate excited energy levels in such a way that they do not relax via collisions, give rise to saturation broadening. This scenario, which is a problem for the works shortly presented because it increases the uncertainty in the determination of the central absorption frequency, can however provide information on intermolecular collision forces and intermolecular mechanisms.

1.6.4 Line intensity

Each molecular transition, now that we have understood why it lies at a specific frequency, has an associated intensity. This section summaries the reasons behind the value a given intensity assumes.

In absorption measurements, be these microwave or IR experiments, the measured intensity corresponds to that which is detected when the frequency of the in-coming beam equals the resonance frequency, i.e. $\omega = \omega_0$. This intensity, assumed to be the maximum transition intensity measured in the experiment, is denoted by $\gamma(\omega_0)$. Consider the fundamental rotational transition $J \rightarrow J+1$ of the OCS, for which $g_m = 2J+1$. Using the high temperature approximation $E_r \ll kT$ and employing the rotational population factor $f_r = \beta B(2J+1)e^{-\beta B(J+1)}$, for a linear molecule we can express the vibrational population factor as:

$$\frac{f_m}{g_m} = f_\upsilon \frac{g_I(J)}{G_I} \frac{B}{T}\left[\frac{h}{k}\right], \tag{1.191}$$

where $G_I = \frac{1}{3}(2I+1)(4I^2+I+1)$ is the overall spin weight factor and for linear molecules $g_I(J) = 1$, it is possible to obtain the element of the dipole moment matrix summed over all components:

$$|\langle J+1|\boldsymbol{\mu}|J\rangle|^2 = \mu^2(J+1) \tag{1.192}$$

After a bit of manipulation, we can now rewrite the equation 1.189 as a function of the intensity associated with the resonance frequency as:

$$\gamma(\omega_0) \equiv \omega_{max} = \left[\frac{8\pi^2}{3ck}\right]\left[\frac{h}{k}\right] a f_\upsilon \frac{N}{\Delta\omega_0} \frac{\omega_0^2 B}{T^2} \frac{g_I(J)}{G_I} \mu^2(J+1)\,, \tag{1.193}$$

where a is an isotopic abundance factor. Note the dependence on the square of the temperature in the denominator and the square of the dipole moment in the nominator. After computing the fundamental constants, converting the frequency factor to MHz, expressing the dipole in Debye and substituting $\frac{N}{\Delta\omega_0} = \frac{3.219\times10^{16}}{\Delta\omega_0^s}$ (with ω^s the standard half width measured at 1mm Hg pressure and 300 K), we can write:

$$\gamma(\omega_0) \equiv \omega_{max} = 4.912\times10^{-12} a f_\upsilon \frac{\omega_0^3}{\Delta\omega_0^s T^2} \frac{g_I(J)}{G_I} \mu^2\,. \tag{1.194}$$

For $^{16}O^{12}C^{32}S$, B_0 = 6081.5 MHz, $\Delta\omega^s$ = 6.27 MHz and $\mu = 0.715D$, which leads to:

$$\gamma(\omega_0) = 0.706\frac{(J+1)^3}{T^2}f_v a. \tag{1.195}$$

The analogue of equation 1.195 for the asymmetric maximum intensity $\gamma(\omega_0)$ is given by:

$$\gamma(\omega_0) = 3.840\times10^{-14} a f_v \frac{\omega_0^2}{\Delta\omega_0^s}\frac{(ABC)^{1/2}}{T^{5/2}}\frac{g_I(JK_AK_C)}{G_I}\mu_\alpha^2\lambda_\alpha(J'\tau', J''\tau'') \tag{1.196}$$

where λ_α factors are tabulated in Hagan 1974. In this way it is possible to determine directly from a spectrum the α-axes dipole moments of a molecule.

1.7 This thesis

Now that we have presented the main theoretical concepts underlying the works presented in this thesis, we will briefly introduce what is contained in the following chapters.

Chapter 2 presents the results of the laboratory study of the rotational ground state spectrum of allylimine (CH_2=CH−CH=NH). As an imine, it is considered to be a promising player in the chemical pathways leading to the formation of amino acids in space. The study led to the creation of a rotational and distortion constants catalogue for the two isomers observed in the laboratory, Ta and Ts. These new data allowed us to obtain a tentative detection of these isomers in the G+0.693-0.027 molecular cloud located at the Galactic Centre, leading to the derivation of the column densities $N = (1.5\pm0.6)\times10^{13}$ cm^{-2} for Ta and $N \sim 0.5\times10^{13}$ cm^{-2} for Ts. We then compared these new results with the isomeric abundances of cyanomethanimine and propargylimine, other crucial imines, confirming the abundance trend we expected to observe.

Chapter 3 deals with the rotational study of aminoacrylonitrile (3-amino-2-propenenitrile, H_2N−CH=CH−C≡N). As a cyanide-bearing molecule, it is also considered to play a key role in the pathways leading to the formation of amino acids in space. The rotation and distortion constants of the isomer observed in the laboratory, Z-APN, were herein measured also employing the Lamb dip technique, allowing to resolve blended components and therefore further increasing the precision of the spectroscopic results. The search for Z-APN in the G+0.693-0.027 molecular cloud led to the identification of the upper limit of $N < 6.6\times10^{12}$ cm^{-2}, leading us to compare this molecular abundance with other cyanide-bearing molecules. We found that the increase in molecular complexity associated with additional carbon and nitrogen atoms lead to a drop in ISM molecular abundances of at least one order of magnitude.

Chapter 4 presents the theoretical study of the NH_2CHCO isomer family, an iminoacetaldehyde molecule proposed to be a crucial step in the formation of ethanolamine ($NH_2CH_2CH_2OH$), recently detected in molecular cloud G+0.693-0.027 and present in the phospholipids of all biological cells. In this work we found that the isomer that in previous studies was considered

to be the most energetically favoured is instead only the ninth most energetic out of 15 structural and conformational isomers that might be present in the gas-phase of the ISM. Specifically, the most energetically favourable isomer of NH_2CHCO is not in the amine but rather the imine form of HNCHCHO. The latter includes three minima, two of which exhibit the lowest isomer or conformational energies, for which we obtained the rotational and distortion constants at the state-of-the-art quantum level of theory, predicting the most intense frequencies and spectral regions to be used to detect these new isomers in the laboratory and in ISM.

In Chapter 5 a summary of the main results presented in the present thesis and an outlook concerning future lab measurements are provided.

Chapter 2

Laboratory spectroscopy of allylimine and tentative detection towards the G+0.693-0.027 molecular cloud

The contents of this chapter were published in the *Astronomy & Astrophysics* Journal.
Credit: Alberton et al., A&A, 669, A93, 2023.

Abstract

Substituted methanimines and ethylenes have been identified in the interstellar medium. Therefore, allylimine (CH_2=CH−CH=NH) represents a promising candidate for a new interstellar detection. The goal of the present work is to perform a comprehensive laboratory investigation of the rotational spectrum of allylimine in its ground vibrational state in order to obtain a highly precise set of rest frequencies to assist its search for astronomical sources. The rotational spectra of the two most stable *trans-anti* and *trans-syn* geometrical isomers of allylimine were recorded in the laboratory in the 84–300 GHz frequency interval. Measurements were performed using a source-modulation millimetre-wave spectrometer equipped with a pyrolysis system for the production of unstable species. High-level ab initio calculations were performed to assist the analysis and to obtain reliable estimates for an extended set of spectroscopic parameters. Guided by new laboratory data, allylimine was searched for in space using a sensitive spectral survey of the G+0.693-0.027 molecular cloud, located at the Galactic centre. Almost 1000 rotational transitions have been recorded for *trans-anti* and *trans-syn* allylimine. These new data have enabled the determination of a very accurate set of spectroscopic parameters including rotational, quartic and sextic centrifugal distortion constants, as well as nuclear quadrupole coupling constants. The improved spectral data allowed us to report a tentative detection for both allylimine isomers in the G+0.693-0.027 molecular cloud, located at the Galactic centre.

2.1 Introduction

To date, about 300 molecules have been detected in the interstellar medium (ISM) in a wide variety of environments, spanning from molecular clouds to late-type stars (see e.g. Endres et al. 2016).[1] In recent years, the number of comparatively large species increased, and complex organic molecules (COMs, Herbst & van Dishoeck 2009) have generated a substantial amount of interest because their presence in the ISM suggests that chemical complexity starts already in the earliest stages of star formation. Furthermore, the discovery of many amino acids in carbonaceous chondrites (Snyder et al. 2005; Aponte et al. 2020) and the identification of glycine, the simplest member of this molecular family, through in situ measurements in the 67P/Churyumov–Gerasimenko comet (Altwegg et al. 2016a), has triggered an intense debate on their chemical origin, with many hypotheses on possible formation pathways, precursors, and intermediates (e.g. Theule, P. et al. 2011; Koch et al. 2008; Woon 2002; Aponte et al. 2017).

Laboratory studies on interstellar ice analogues indicate that amino acids can form via hydration of an aminonitrile compound ($H_2N-CHR-CN$, Koch et al. 2008), which in turn may be generated under astrophysical conditions in two ways. One pathway, driven by photochemistry, consists in the addition of ammonia to the corresponding nitrile (R−CN, Danger et al. 2011); alternatively, the formation can proceed through the Strecker synthesis, a reaction scheme that has been demonstrated to take place not only in solution, but also in the solid phase (Bossa et al. 2009). This process starts from the condensation of ammonia with an aldehyde (R−CHO, see Rimola et al. 2010) and involves imines (RCH=NH) as reactive intermediates (Walch et al. 2001).

Imines are a class of nitrogen-bearing molecules that have a good record of detection in the ISM. Methanimine (CH_2=NH), the simplest member, was revealed in the ISM in 1973 by Godfrey et al.. Subsequently, other more complex species were identified: ethanimine (CH_3CH=NH, Loomis et al. 2013a), *C*-cyanomethanimine (NC−CH=NH, Zaleski et al. 2013a; Rivilla et al. 2019), and propargylimine (HC≡C−CH=NH, Bizzocchi et al. 2020). More recently, ketenimine (CH_2=C=NH, Lovas et al. 2006) has been tentatively detected and an upper limit has been reported for propanimine (CH_3CH_2CHNH, Margulès et al. 2022).

Formation routes of imines via tautomerisation (Lovas et al. 2006) or partial hydrogenation on the dust grain surface (Theule, P. et al. 2011; Krim et al. 2019) of nitriles have been put forth in the past. More recently, a promising hypothesis points to the role of methanimine as the progenitor of complex imines upon the addition or elimination of reactive radicals. Theoretical studies showed that gas-phase reactions of the CN and CCH radicals with CH_2=NH are exothermic and barrierless, leading to *C*-cyanomethanimine (Vazart et al. 2015) and propargylimine (Lupi et al. 2020), respectively. Generalising this idea, we can speculate that more complex members of the same chemical family are produced in the cold ISM through the process Puzzarini (2022)

$$R^{\cdot} + CH_2{=}NH \longrightarrow R{-}CH{=}NH + H^{\cdot}\ , \tag{2.1}$$

where $R^{\cdot}$ is a generic small radical. Following this scheme, the species allylimine (CH_2=CH−CH=NH, also known as 1-aza-1,3-butadiene) is an interesting candidate for generation through the above

[1] See also the updated list presented at this URL: `http://www.astrochymist.org/astrochymist_ism.html`

reaction with R˙ being the vinyl radical (CH_2=CH˙), which is likely to be abundant in the interstellar gas. Many vinyl-containing compounds have been detected so far: CH_2=CHCN, (Gardner 1975), CH_2=CHOH (Agúndez et al. 2021), CH_2=CHCHO (Hollis et al. 2004), CH_2=$CHNH_2$ Zeng et al. 2021, CH_2=CH−CCH (Cernicharo et al. 2021), and CH_2=CH−C_3N (Lee et al. 2021b).

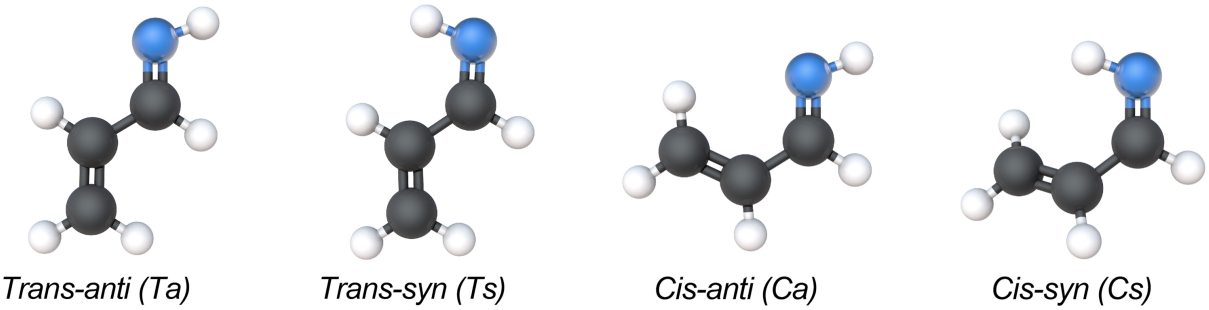

Figure 2.1: Isomers of allylamine.

To date, allylimine has not been effectively searched for in space as it lacked a satisfactory spectroscopic characterisation. To the best of our knowledge, only two earlier and rather outdated studies are present in the literature. The first laboratory investigation was published by Penn (1978), who recorded the microwave spectra of two structural isomers of this molecule in the 8–26 GHz frequency range using a Stark-modulation spectrometer. A few years later, Brown et al. (1981) investigated a few rotational transitions at centimetre (cm) wavelengths and determined the ^{14}N-quadrupole coupling constants. Both of these studies are based on a very limited data set; the spectroscopic analyses are thus incomplete and lack an accurate treatment of the centrifugal distortion effects.

For the reasons above, we carried out a detailed laboratory investigation of the rotational spectra of the most stable isomers of allylimine extending the frequency coverage well into the millimetre (mm) domain. The goal is to obtain an accurate centrifugal distortion analysis and to generate an improved line catalogue for radio astronomical purposes. Guided by the new laboratory data, we performed a search for allylimine towards the quiescent G+0.693-0.027 molecular clouds (hereafter G+0.693), located at the central molecular zone (CMZ) in the inner $\sim$ 500 pc of our Galaxy. In this object, methanimine, cyanomethanimine, and propargylimine have recently been detected (Zeng et al. 2018; Rivilla et al. 2019; Bizzocchi et al. 2020), together with many other molecular species, including several first detections in the ISM (Jiménez-Serra et al. 2020; Rivilla et al. 2020b, 2021a,c, 2022a,b,c; Rodríguez-Almeida et al. 2021a,b; Zeng et al. 2021; Jiménez-Serra et al. 2022a; Colzi et al. 2022).

The experimental procedure is described in Sect.2.2. A concise account of the molecular properties of allylimine and the theoretical calculations performed to support the data analysis is given in Sect.2.3. The spectral analysis is described in Sect.2.4, and the astronomical observations in Sect. 2.5. In Sec. 2.6 we discuss the results, and in Sect. 2.7 we draw our conclusions.

2.2 Experimental details

The rotational spectrum of allylimine has been investigated using two millimetre-wave spectrometers located at the Center for Astrochemical Studies at the Max-Planck-Institut für extraterrestrische Physik in Garching (Germany) and at the Department of Chemistry of the University of Bologna (Italy). In the following we provide a brief description of the two experimental set-ups.

2.2.1 CASAC spectrometer

The Center for Astrochemical Studies Absorption Cell (CASAC) was employed to record the spectrum of allylimine in the 80-240 GHz range. The instrument has been described comprehensively in the introduction and only a few details relevant for the present study are reported here. The instrument uses an active multiplier chain (Virginia Diodes) as the primary source of millimetre radiation in the 82–125 GHz band. This device is fed by a 9–15 GHz synthesizer locked to a Rb atomic clock for accurate frequency and phase stabilisation. Further multiplier stages, applied in cascade, allow a frequency coverage up to ∼1.1 THz. A dry InSb hot electron bolometer operating at 4 K is used as a detector. The frequency-modulation technique is employed to improve the signal-to-noise ratio (S/N): the source is sine-wave modulated at 50 kHz and the detector output is demodulated at twice this frequency ($2f$ detection) by a lock-in amplifier, so that the second derivative of the actual absorption profile is recorded by the computer-controlled acquisition system.

The same absorption cell and pyrolysis system used to study propargylimine (Bizzocchi et al. 2020) were adopted for this experiment. Allylimine was produced as described by Penn (1978). Diallylamine vapours were flowed through a 1 cm diameter quartz tube heated to 800°C with a typical pressure of 180 mTorr (24 Pa). The pyrolysis products were directly flowed through the absorption cell, which was continuously pumped and kept at a pressure of about 4 mTorr (0.5 Pa).

2.2.2 Bologna millimetre spectrometer

Rotational spectra between 240 and 310 GHz were recorded using the frequency-modulation millimetre/submillimetre-wave spectrometer located in Bologna (Melosso et al. 2019a,b). A Gunn diode working in the W band (80–115 GHz) coupled to a passive frequency multiplier (WR3.4x3, Virginia Diodes Inc.) was used as the main radiation source, whose frequency is stabilised and controlled through a phase-lock-loop (PLL). A frequency-modulated 75 MHz signal, coming from a centimetre-wave synthesizer (HP8642A), was used as intermediate frequency in the PLL. All the electronics are referenced to a Rb atomic clock. The detection system is composed of a zero-bias detector (WR3.4ZBD, Virginia Diodes Inc.) operating in the 220–330 GHz range and a lock-in amplifier. The latter has the twofold purpose of demodulating the output signal using the $2f$ detection scheme and filtering out some background noise as a resistor-capacitor circuit.

The measurements were performed in a quartz absorption cell surrounded by a 90 cm long tubular oven, using the same set-up recently described by Jiang et al. (2021). The optical elements of the spectrometer were arranged in a double-pass configuration (for further details, see

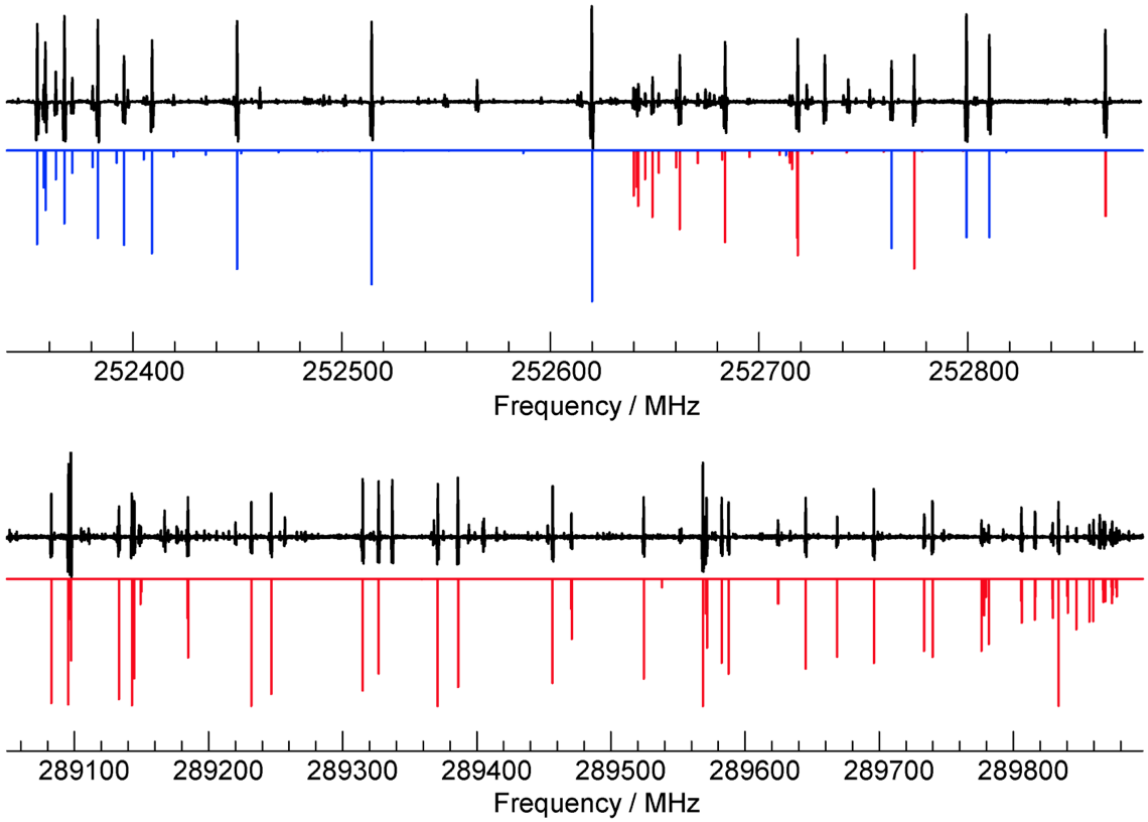

Figure 2.2: Portions of the experimental spectrum (in black) showing both *a*- and *b*-type spectral features (blue lines for *Ts*-allylimine and red lines for *Ta*-allylimine). Intensity is in arbitrary units.

e.g. Melosso et al. 2020a,b) in order to reach an absorption path-length of ~ 3 m. Allylimine was produced directly inside the absorption cell by heating diallylamine vapours at a temperature of 500°C. Differently from what was observed in the past for other imines, for which the flash vacuum pyrolysis was performed externally to the absorption cell (Melosso et al. 2018; Melli et al. 2018, 2020), good signals of allylimine were already obtained at 100°C. The working temperature of 500°C was chosen with the unique purpose of obtaining stable experimental conditions since the ON/OFF control of the oven causes some oscillation at lower temperatures.

2.3 Molecular properties

Allylimine can be conveniently thought as an iminic moiety −CH=NH connected to a vinyl group CH_2=CH– by a single C−C bond. Depending on the relative orientation of these two subunits, four geometrical isomers can be defined. The prefixes *cis*- (*C*) and *trans*- (*T*) are used to identify the position of the two constituents with respect to the central C-C bond, respectively on

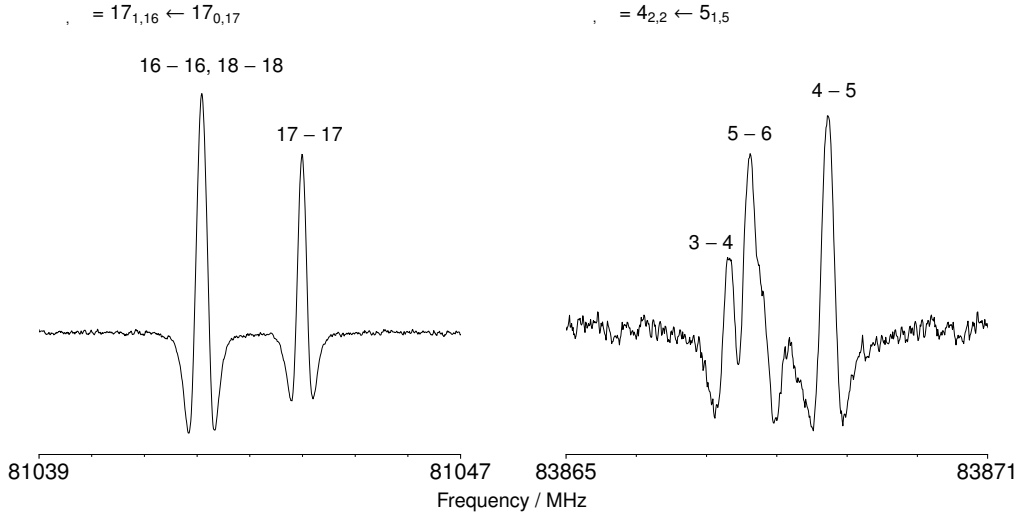

Figure 2.3: Recordings of two b-type transitions of *Ta*-allylamine. The nitrogen quadrupole coupling splitting is evident (each hyperfine component has a $F' - F$ label). Left panel: $J_{Ka,Kc} = 17_{1,16} \leftarrow 17_{0,17}$; right panel: $J_{Ka,Kc} = 4_{2,2} \leftarrow 5_{1,5}$.

the same and on the opposite side; the labels *syn*- (s) and *anti*- (a) define the position of the iminic H with respect to C=C. The resulting four geometric isomers are depicted in Figure 2.1 and are denoted *Ta*, *Ts*, *Ca*, and *Cs*. All forms but *Cs* have a planar structure with C_s symmetry. In the *Cs* form, owing to the repulsion between the iminic H and one terminal vinyl H, the molecular backbone is tilted and the molecular symmetry is C_1, in analogy to trans-butadiene (Baraban et al. 2018) and azabutadiene (Jiang et al. 2022).

The molecular and spectroscopic properties of the four allylimine isomers were evaluated by means of state-of-the-art computational methodologies. Equilibrium structures (and their corresponding energies), which straightforwardly provide equilibrium rotational constants, were computed by exploiting the so-called CCSD(T)/CBS+CV composite scheme (Heckert et al. 2005, 2006). This approach is based on the CCSD(T) method (i.e. coupled cluster singles and doubles approximation augmented by a perturbative treatment of triple excitations; Raghavachari et al. 2013) and accounts for the extrapolation to the complete basis set (CBS) limit and core-valence (CV) correlation effects. Vibrational corrections to equilibrium rotational constants, evaluated at a lower level of theory, were incorporated to predict ground-state rotational constants. Quartic and sextic centrifugal distortion parameters as well as first-order molecular properties (dipole moments and nuclear quadrupole coupling constants) were accurately predicted by exploiting CCSD(T) calculations. For nuclear quadrupole coupling constants, vibrational corrections to the equilibrium values were also considered. A detailed account on the quantum-chemical calculations performed is provided in Appendix A.1.

The relative energies and the electric dipole moments of the four allylimine isomers are reported in Table 2.1. Our calculations indicate that the *Ta* isomer is the most stable, *Ts* is relatively close at $\Delta E = 403.5$ K, while the *Ca* and *Cs* species have higher energies, $\Delta E > 1400\,K$. In the

Table 2.1: Computed relative energies[a] of the four allylimine isomers and their dipole moment components[b].

	unit	*Ta*	*Ts*	*Ca*	*Cs*
E	K	0.0	282.4	955.2	1200.4
		0.0	403.49	1364.78	1715.12
μ_a	D	1.14	2.44	-0.02	2.40
μ_b	D	-1.70	0.79	-1.68	0.44
μ_c	D	0.0	0.0	0.0	0.19
μ	D	2.05	2.56	1.68	2.44

Notes. [a] CCSD(T)/CBS+CV level of theory. [b] ae-CCSD(T)/cc-pCVQZ level of theory.

present investigation, we focus on the *Ta* and *Ts* isomers, which are the only two species detected in our laboratory experiments. Both are nearly prolate asymmetric top rotors ($\kappa \sim -0.98$); their dipole moments are rather similar ($|\mu| \approx 2\,\mathrm{D}$), but they differ in the corresponding principal axis projections. As Table 2.1 shows, the spectrum of the *Ts* isomer is dominated by *a*-type transitions, whereas the *Ta* species has almost equally strong *a*- and *b*-type spectra.

2.4 Spectral analysis and results

The rotational spectra of the *Ta* and *Ts* allylimine isomers have been recorded in selected frequency regions from 84 to 307 GHz. Two portions exhibiting typical *a*- and *b*-type patterns are shown in Figure 2.2. In line with a nearly prolate rotor and the dipole components of Table 2.1, the *Ts* spectrum presents strong ${}^aR_{0,1}{}^2$ branch transitions spaced by $\Delta\nu \approx (B+C)$. For the *Ta* isomer, instead, ${}^bQ_{1,-1}$ branch band heads spaced by $\Delta\nu \approx 2A - B - C$ dominate the spectrum, leading to a more complicated pattern.

From the computed relative energy (see Table 2.1), a relative [*Ta*]/[*Ts*] isomer abundance of 3.8 can be estimated at 300 K (4.4×10^{17} at 10 K). From the relative intensity comparison of two closely spaced *Ta* and *Ts* lines recorded under the same experimental conditions (source power, sample pressure, temperature, and modulation depth) we derived [*Ta*]/[*Ts*] = 3.3 ± 0.8, in good agreement with the theoretical findings. Therefore, regarding the CASAC experiment, although allylimine is generated at high temperatures, a complete thermalisation is readily achieved in the room temperature absorption cell. On the contrary, the same does not apply to the Bologna experiment, which is characterised by a different set-up.

Owing to the presence of the ^{14}N nucleus with spin $I = 1$ in the molecule, its non-zero

[2]The symbol ${}^xM_{\delta K_a,\delta K_c}$ is used to identify the transition type of an asymmetric rotor: x stands for the dipole moment component involved; $M = P, Q, R$ for the transitions with $\Delta J = -1, 0, +1$, respectively; δK_a and δK_c for the (signed) change of the K_a and K_c pseudo quantum numbers (Gordy & Cook 1984).

nuclear quadrupole moment interacts with the molecular electric field gradient at the nucleus, giving rise to the hyperfine structure of the rotational spectrum. The interaction between the rotational angular momentum $\mathbf{J}$ and the nitrogen nuclear spin $\mathbf{I}_N$ is described by the standard vector coupling scheme:

$$\mathbf{J} + \mathbf{I}_N = \mathbf{F} \,. \tag{2.2}$$

As a result, each rotational level with $J > 0$ splits into three hyperfine sub-levels labelled with the total angular quantum number F, where $F = J - 1, J, J + 1$. Therefore, the corresponding transitions are split into several components according to the $\Delta F = 0, \pm 1$ selection rules, with the strongest features having $\Delta F = \Delta J$. An example of these hyperfine patterns is given in Fig. 2.3.

A total of 617 and 470 lines were recorded for *Ta*- and *Ts*-allylimine, respectively, of which 293 and 65 exhibited resolvable hyperfine features that allowed their components to be assigned. For transitions with unresolved hyperfine structure, the intensity-averaged calculated frequency was instead compared with the recorded line. A few transitions (22 and 10 for *Ta* and *Ts*, respectively) taken from the literature (Penn 1978) were also included in the final data sets. To account for the different measurement precision (σ) of the two experimental sub-sets of data recorded with the CASAC and Bologna spectrometer, distinct statistical weights $w = 1/\sigma^2$ were assigned. The corresponding values are σ = 15 kHz and σ = 25–30 kHz (depending on experimental conditions).

The analysis was performed using a Hamiltonian composed of a purely rotational and a hyperfine term:

$$\hat{H} = \hat{H}_{\rm rot} + \hat{H}_{\rm HFS} \,. \tag{2.3}$$

Here $\hat{H}_{\rm rot}$ is the S-reduced Watson-type rotational Hamiltonian in its I^r representation (Watson 1977) including the centrifugal distortion up to sextic terms, whereas the hyperfine-structure Hamiltonian $\hat{H}_{\rm HFS}$ describes the ^{14}N-quadrupole interaction making use of the traceless tensor χ, which has χ_{aa} and $\chi_{bb} - \chi_{cc}$ as determinable coefficients. No ^{14}N or H spin-rotation coupling effects were revealed; therefore, the corresponding interaction terms have been neglected in the present analysis.

The spectral analyses were carried out using the `CALPGM` program suite (Pickett 1991). Transitions with the J quantum number as high as 52 and 46 are included for the *Ta* and *Ts* species, respectively, whereas the maximum K_a value reached is 18 and 22, respectively. The spectroscopic constants determined from the fits are collected in Table 2.2, together with the corresponding computed values. The quality of the fits is expressed by the weighted root mean square $\sigma_{\rm rms}$:

$$\sigma_{\rm rms} = \sqrt{\frac{1}{N} \sum_{i=1}^{N} \left(\frac{x_i^{obs} - x_i^{calc}}{\sigma_i} \right)^2} \,, \tag{2.4}$$

where x_i denotes the N data, and σ_i the corresponding assumed uncertainties. For *Ta*- and *Ts*-allylimine, values of 1.03 and 1.00 were obtained for σ_{rms}, respectively, thus indicating that, on average, the data sets have been reproduced within the experimental uncertainties.

Owing to the new extensive data set, the spectroscopic characterisation of allylimine is considerably improved. Compared to the previous results reported by Penn (1978), the uncertainty

Table 2.2: Spectroscopic constants determined for the *Ta* and *Ts* isomers of allylimine[a].

		Ta-allylimine		*Ts*-allylimine	
constant	unit	experiment	ab initio[b]	experiment	ab initio[b]
A	/ MHz	45773.64504(81)	45797.91440	43755.655(17)	43766.134
B	/ MHz	4560.931313(62)	4561.224130	4564.54014(68)	4565.77443
C	/ MHz	4148.248522(60)	4148.336622	4134.46273(64)	4135.28507
D_J	/ kHz	0.909645(28)	0.9054	0.95037(37)	0.9472
D_{JK}	/ kHz	-7.53100(98)	-7.5174	-7.589(12)	-7.4241
D_K	/ kHz	296.804(27)	286.9488	257.29(74)	243.0085
d_1	/ kHz	-0.107148(13)	-0.1094	-0.114863(46)	-0.1182
d_2	/ kHz	-0.0058627(15)	-0.0055	-0.006237(31)	-0.0059
H_J	/ mHz	0.21719[c]	0.21719	0.22243[c]	0.22243
H_{JK}	/ Hz	-0.00604(44)	-0.00306	-0.00723(54)	-0.0034
H_{KJ}	/ Hz	-0.2997(20)	-0.3809	-0.196(15)	-0.299
H_K	/ Hz	2.89(24)	4.55	3.61474[c]	3.61474
h_1	/ mHz	0.0667(43)	0.0762	0.08093[c]	0.08093
h_2	/ mHz	0.01095[c]	0.01095	0.01087[c]	0.01087
h_3	/ mHz	0.00157[c]	0.00157	0.00152[c]	0.00152
χ_{aa}	/ MHz	0.751(23)	0.731	-2.963(17)	-2.974
$\chi_{bb} - \chi_{cc}$	/ MHz	-6.985(19)	-6.906	-3.267(10)	-3.263
No. of lines		617		470	
σ_{wrms}		1.03		1.00	
σ_{rms}	/ kHz	103.8		64.2	

Notes. [a] Numbers in parentheses represent 1σ standard deviation in unit of the last digit. [b] Equilibrium constants at the CCSD(T)/CBS+CV level, vibrational corrections computed at the fc-CCSD(T)/cc-pVTZ level of theory. Quartic centrifugal distortion constants computed at the CCSD(T)/CBS+CV level. Sextic centrifugal distortion constants computed at the fc-CCSD(T)/pVTZ level of theory. Nuclear quadrupole coupling constants computed at ae-CCSD(T)/cc-pCVQZ level and including vibrational corrections at the ae-MP2/cc-pCVTZ level of theory. See Appendix A.1 for a detailed account. [c] Fixed at the computed value.

of the rotational constants A, B, and C is reduced by three orders of magnitude (a factor of ~ 350 for the *Ts* isomer). Additionally, a complete set of quartic centrifugal distortion constants (with a precision of $\sim 0.1\%$) plus four sextic terms (two for the *Ts* isomer) are provided for the first time. To give an example of the improvement accomplished, the $J_{Ka,Kc} = 20_{0,20} - 19_{0,19}$ transition,

Table 2.3: Partition function values and abundance ratios at different temperatures for allylimine isomers.

	Ta-allylimine			*Ts*-allylimine			isomer ratio
T/K	$Q_{\rm rot}$	$Q_{\rm HFS}$	$Q_{\rm vib}$	$Q_{\rm rot}$	$Q_{\rm HFS}$	$Q_{\rm vib}$	$[Ta]/[Ts]$
2.725	26.410	79.230	1.0000	27.044	93.507	1.0000	6×10^{64}
5.0	64.909	194.726	1.0000	66.470	199.410	1.0000	2×10^{35}
9.375	165.616	496.848	1.0000	169.603	508.809	1.0000	7×10^{18}
18.75	466.788	1400.365	1.0000	478.031	1434.093	1.0000	2×10^{9}
37.5	1318.032	3954.097	1.0000	1349.784	4049.354	1.0001	5×10^{4}
75.0	3725.194	11175.583	1.0436	3814.943	11444.829	1.0577	2×10^{2}
150	10534.861	31604.447	1.3245	10788.605	32365.815	1.3781	15
225	19356.422	58069.266	1.8714	19822.670	59468.011	1.9792	6.1
300	29807.537	89422.612	2.8263	30525.403	91576.209	3.0190	3.8
500	64168.784	192506.343	10.746	65709.506	197128.509	11.606	2.2
1000	180019.528	540056.184	504.77	184077.689	552230.592	546.52	1.5

expected to lie at 170.730 GHz with a logI of -3.82 nm^{2}MHz by Penn (1978), is now predicted at 170.726 GHz with a logI of -3.90 nm^{2}MHz, with an offset of 4 MHz between the two sets of data.

The comparison with the computed spectroscopic parameters (also reported in Table 2.2) points out a very good agreement for the rotational constants, which differ, on average, by only 0.07% from the experimental counterparts. The quartic centrifugal distortion constants, except for the D_{JK} of *Ta*, also compare well with the experimental values, showing an average relative deviation of 3% for the two isomers. It was also possible to constrain the sextic centrifugal distortion constants to a partial set of sextic parameters: H_{JK}, H_{KJ}, H_K, h_1 for the *Ta* isomer and H_{JK}, H_{KJ} for the *Ts* isomer, with the remaining sextic terms kept fixed at the computed values. For the quadrupole coupling constants the agreement is on average within 1.1%.

From the improved spectroscopic constants determined in the present work, two collections of rest frequencies were produced for each isomer, and are accessible at CDMS[3](Müller et al. 2005; Endres et al. 2016); the <X>allylimine.cat catalogue list of pure rotational transitions extends up to 300 GHz, whereas the hfs_<X>allylimine.cat catalogue is limited to the 3 mm band (ν < 120 GHz), but contains all hyperfine components. The symbol <X> in the file names reads as <Ta-> or <Ts-> for the corresponding isomers. The catalogues were generated with the SPCAT routine (Pickett 1991) and their format matches that of the CDMS and JPL (Pickett et al. 1998) catalogues, thus allowing their straightforward use in astronomic line-analysis tools, such as MADCUBA (Martín et al. 2019a), CASSIS (Vastel et al. 2015) and MADEX (Cernicharo, J. 2012).

[3]https://cdms.astro.uni-koeln.de/cdms/portal/

A selection of rotational (Q_{rot}), hyperfine (Q_{HFS}), and vibrational (Q_{vib}) partition functions for *Ta*- and *Ts*-allylimine is given in Table 2.3. The values were computed for the 3 – 1000 K temperature interval and were obtained by direct summation over the rotational or hyperfine levels, whose energies have been accurately determined from the spectral analysis. The vibrational partition functions Q_{vib} were computed using harmonic frequencies at the CCSD(T)/CBS+CV level, which were obtained as explained in Appendix A.1.

2.5 Interstellar search towards the G+0.693 molecular cloud

We searched for the *Ta* and *Ts* allylimine isomers towards the G+0.693 molecular cloud, which is located in the SgrB2 complex of the CMZ of our Galaxy. This region is thought to be affected by a cloud-cloud collision (Zeng et al. 2020a) that produced large-scale shocks that sputtered the interstellar dust grains, thus releasing into the gas phase multiple molecules formed on the dust surfaces. This explains the extremely rich chemistry of G+0.693, where many complex organic molecules have been detected.

We exploited a sensitive unbiased spectral survey performed with the Yebes 40m (Guadalajara, Spain) and the IRAM 30m (Granada, Spain) telescopes. In both surveys, we used the position switching mode pointed towards α(J2000.0)= $17^h47^m22^s$, δ(J2000.0)= $-28°21'27''$. We used Yebes 40m observations from 31.075 GHz to 50.424 GHz, and IRAM 30m observations for the 71.770−116.720 GHz, and 124.77−175.5 GHz frequency ranges. More detailed information of the observational survey, including noise levels and spectral resolutions, are available in Rivilla et al. (2021a,c).

We implemented the spectroscopy parameters presented in this work into the MADCUBA package[4]; version 11/03/2022; Martín et al. 2019a). Using the Spectral Line Identification and Modeling (SLIM) tool of MADCUBA, we generated synthetic spectra of the two lowest energy isomers of allylimine (*Ta* and *Ts*) under the assumption of local thermodynamic equilibrium (LTE) to be compared with the observed spectra.

Figure 2.4 shows the brightest transitions of the *Ta* form that, according to the LTE synthetic spectra, appear unblended or slightly blended with emission from other species already identified in this source, which contributes to well reproducing the observed spectra. The spectroscopic information for these *Ta*-allylimine transitions is shown in Table 2.4 and in Figure 2.4. We note that all the remaining transitions of *Ta*-allylimine predicted within the LTE approximation are heavily contaminated by stronger emission from other species, and that there are no missing lines in the data.

To derive the column density, we used the AUTOFIT tool of SLIM (see Martín et al. 2019a), which finds the best fit between the simulated LTE model and the observed spectra. We also considered the contribution to the emission from other molecules. The excitation temperature (T_{ex}) found for most of the molecules detected towards this molecular cloud is low, typically in the range 5-20 K (see e.g. Zeng et al. (2018)). This T_{ex} is significantly lower than the kinetic temperature of the cloud ($\sim$ 150K) because the molecules are sub-thermally excited, due to the

[4]Madrid Data Cube Analysis on ImageJ is a software developed at the Center of Astrobiology (CAB) in Madrid; http://cab.inta-csic.es/madcuba/

Table 2.4: Tentatively observed rotational transitions of both allylimine isomers.

Frequency (GHz)	Transition (J_{K_a,K_c})	log I (nm^2 MHz)	log A_{ul} (s^{-1})	g_u	E_u (K)
		Ta-allylimine			
34.005084	$4_{1,4}$ - $3_{1,3}$	-5.915	-6.61439	9	6.1
41.625114	$1_{1,0}$ - $1_{0,1}$	-5.798	-5.93554	3	2.4
42.670365	$3_{1,2}$ - $3_{0,3}$	-5.417	-5.91009	7	4.6
43.483824	$5_{0,5}$ - $4_{0,4}$	-5.577	-6.25570	11	6.3
45.920789	$6_{1,5}$ - $6_{0,6}$	-5.110	-5.82973	13	11.0
74.199397	$4_{1,4}$ - $3_{0,3}$	-5.075	-5.43533	9	6.1
89.402598	$6_{1,6}$ - $5_{0,5}$	-4.766	-5.19928	13	10.6
160.373509	$4_{2,2}$ - $3_{1,3}$	-4.552	-4.57186	9	12.1
		Ts-allylimine			
33.928717	$4_{1,4}$ - $3_{1,3}$	-5.277	-5.96658	9	6.0
34.760580	$4_{0,4}$ - $3_{0,3}$	-5.225	-5.90658	9	4.2
35.648859	$4_{1,3}$ - $3_{1,2}$	-5.234	-5.90309	9	6.2
42.404266	$5_{1,5}$ - $4_{1,4}$	-4.978	-5.65561	11	8.0
44.554160	$5_{1,4}$ - $4_{1,3}$	-4.936	-5.59007	11	8.3
76.255852	$9_{1,9}$ - $8_{1,8}$	-4.218	-4.86012	19	20.2
77.870388	$9_{0,9}$ - $8_{0,8}$	-4.192	-4.82681	19	18.7
80.117576	$9_{1,8}$ - $8_{1,7}$	-4.176	-4.79588	19	21.1

[-1.5ex]

Notes. The log I, with I the integrated intensity, is computed at 300 K; in the log A_{ul}, A refers to the absorption Einstein coefficients; g_u refers to the upper state degeneracy.

relatively low density of the cloud ($\sim 10^4 - 10^5$ cm^{-3}, Zeng et al. 2020a). For this reason, we used the T_{ex} value of 8K derived for a very similar species, propargylimine (Bizzocchi et al. 2020), with a FWHM of 20 km s^{-1} and velocity v_{LSR} = 69 km s^{-1}. We obtained N=(1.5±0.6)×10^{13} cm^{-2}, which implies a molecular abundance compared to molecular hydrogen of ∼4×10^{-11}, using $N(H_2)$=1.35×10^{23} cm^{-2} (Martín et al. 2008).

Similarly, several transitions of the *Ts* species are tentatively detected, as shown in Figure 2.5 (see Table 2.4 for their spectroscopic information). In this case the AUTOFIT algorithm did not converge, so we changed the value of N (leaving the other parameters fixed) until we found a good correspondence with the observed spectrum. We obtained $N \sim 0.5\times10^{13}$ cm^{-2}, a factor of ∼3 less abundant that the *Ta* isomer. This is in good agreement with the results found for other isomers, for which the most stable species is the most abundant, for example cyanomethanimine and propargylimmine (Rivilla et al. 2019; Bizzocchi et al. 2020, respectively).

The tentative detections of both forms of allylimine presented here confirm that these species are less abundant than others imines detected towards G+0.693. The *Ta* isomer is a factor of ∼36,

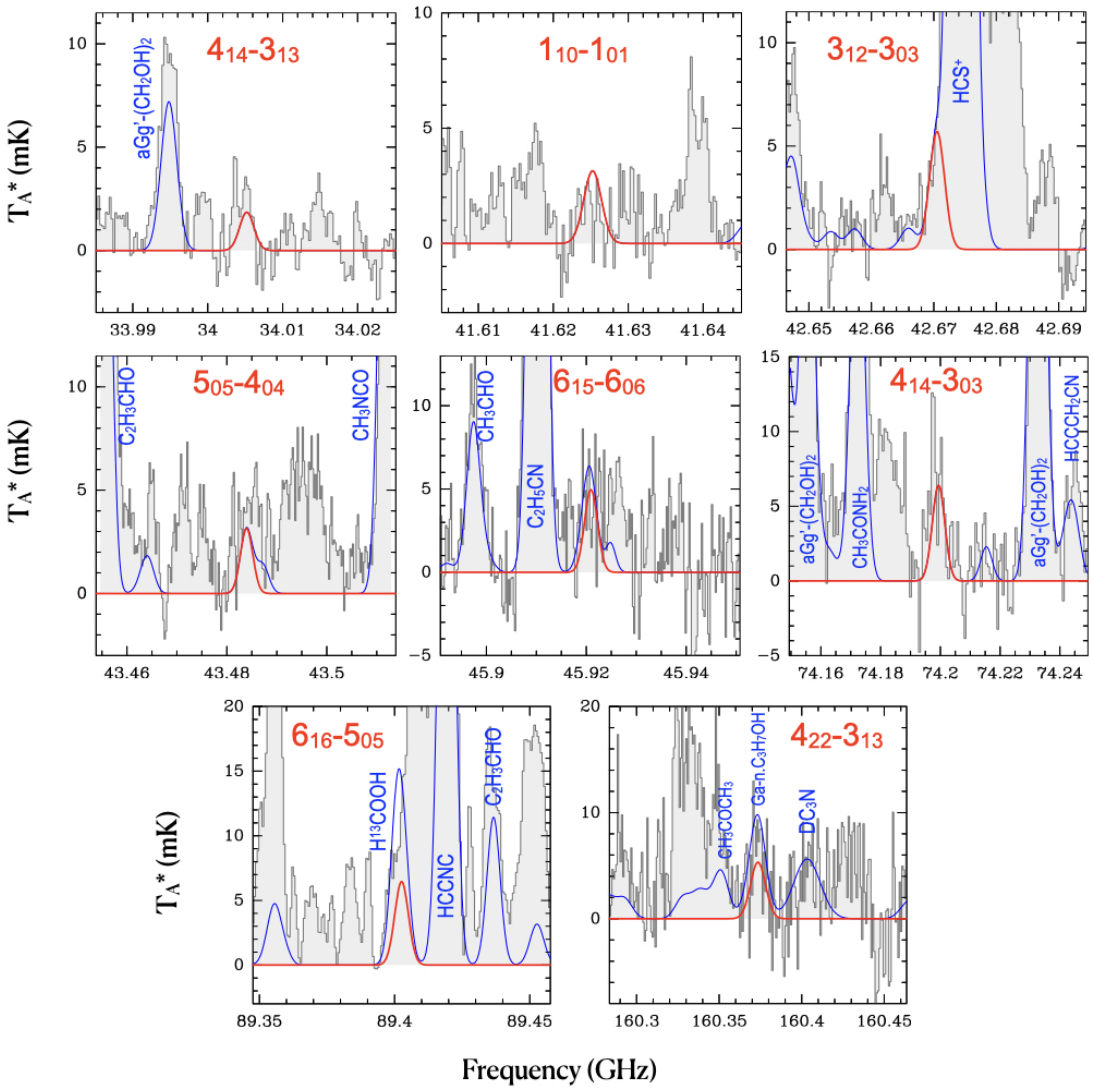

Figure 2.4: *Ta*-allylimine transitions tentatively detected towards G+0.693. The observed spectrum is shown in grey histograms. The simulated LTE spectrum of *Ta*-allylimine using the parameters explained in the text (Section 2.4) is indicated by the red curve. The blue curve denotes the contribution of all the species identified in G+0.693, including allylimine. The quantum numbers of the *Ta*-allylimine transitions are provided in each panel.

~13, and ~1.6 less abundant than methanimine (CH_2NH, Zeng et al. 2018), Z-cyanomethanimine (Z-HNCHCN, Rivilla et al. 2019), and Z-propargylimine (Z-HCCCHNH, Bizzocchi et al. 2020), respectively. This confirms a clear trend of decreasing molecular abundance with increasing imine complexity, similarly to what is found for other chemical families towards G+0.693, such as alcohols (Jiménez-Serra et al. 2022a), isocyanates (Rodríguez-Almeida et al. 2021b), aldehydes (Sanz-Novo et al. 2022), and thiols (Rodríguez-Almeida et al. 2021a).

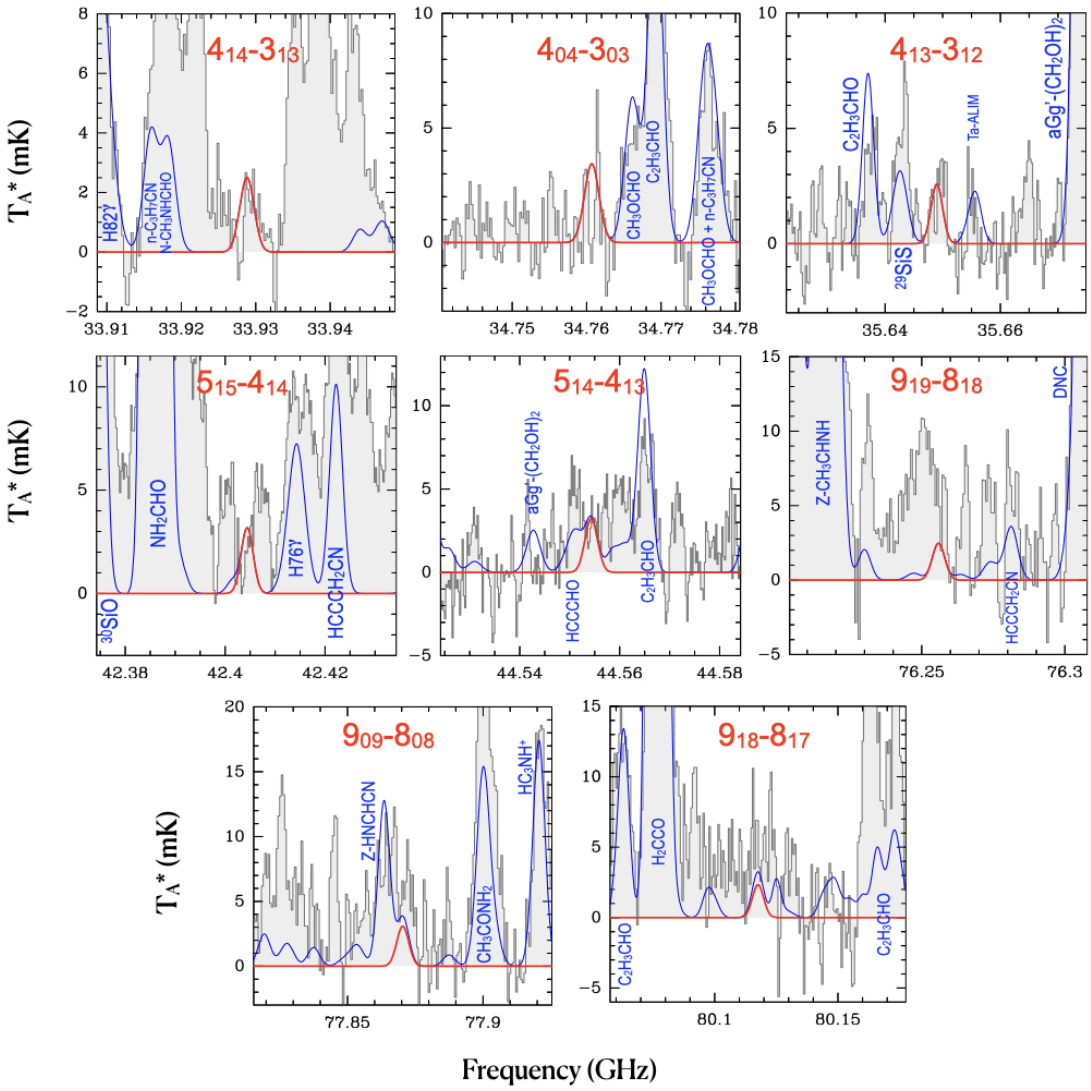

Figure 2.5: *Ts*-allylimine transitions tentatively detected towards G+0.693. The observed spectrum is shown in grey histograms. The simulated LTE spectrum of *Ts*-allylimine using the parameters explained in the text (Section 2.4) is indicated by the red curve. The blue curve denotes the contribution of all the species identified in G+0.693, including allylimine. The quantum numbers of the *Ts*-allylimine transitions are indicated in each panel.

2.6 Discussion

The analysis of the transitions tentatively assigned to allylimine in G+0.693 yielded a plausible estimate of its abundance, in line with the trend established by the other detected members of the same class. Starting from methanimine (RCH=NH, with R=H), an inverse relation between the observed abundance and the complexity of the R moiety is highlighted. Recent theoretical

investigations on imine formation routes suggest that methanimine may actually act as the main progenitor (Lupi et al. 2020; Puzzarini & Barone 2020), and the processes leading to the various species are substantially influenced by the abundances of the R radicals that take part in the relevant reaction. The column density of allylimine estimated in this work (0.15×10^{14} cm^{-2}, *Ta* isomer) is less than that derived for propargylimine (0.24×10^{14} cm^{-2}, *Z*-isomer, Bizzocchi et al. 2020), thus suggesting a consistent relationship between the CCH and CH_2=CH species. To date, no estimates of the vinyl radical column density are available, but the abundance ratio of the corresponding cyanides, $[HC_3N]/[CH_2=CHCN] \sim 8$ (Bizzocchi et al. 2020), points in that direction.

The $[E]/[Z]$ isomeric ratio of imines in the ISM is a topic that has recently attracted some attention (see e.g. Rivilla et al. 2019 and reference therein). Generally speaking, the observed geometrical isomer ratio can be attributed to the combined effects of formation and destruction processes (Vazart et al. 2015; Shingledecker et al. 2020). An alternative hypothesis, which has been recently put forth, suggests that the conversion from the least stable isomer to the most stable one is feasible even at very low temperatures via quantum tunnelling (García de la Concepción et al. 2021). In this framework, the isomeric abundances of imines are governed solely by thermodynamics, and the observed $[E]/[Z]$ ratios should be interpreted in terms of their relative stability. This scenario has had some success in reproducing the isomeric ratios observed in G+0.693 for cyanomethanimine ($[Z]/[E] \sim 6$), ethanimine ($[Z]/[E] = 10 - 15$), and propargylimine ($[Z]/[E] > 2$), when assuming a kinetic temperature $T_{\rm kin} = 150$ K. For allylimine, by inserting the energy difference between *Ts* and *Ta* isomers, $\Delta E/k = 403.5$ K, in Eq. (5) of García de la Concepción et al. (2021), one gets an isomeric ratio $[Ta/Ts] \sim 15$, which is higher than the (tentatively) observed value of ~ 3. This would suggest that there is an extra abundance of the less stable *Ts* isomer with respect to that predicted by thermochemistry. This would also be in contrast relative dipole principle (RDP) proposed by Shingledecker et al. (2020), which postulates an anti-correlation between the relative isomer abundance and the magnitude of their permanent dipole moments ($\mu_{Ta} = 2.05$ D and $\mu_{Ts} = 2.56$ D). Therefore, either the formation of *Ts*-allylimine is kinetically favoured or the two isomers originate from distinct chemical routes.

2.7 Conclusions

This paper reports on an extensive spectroscopic characterisation of allyllimine, CH_2=CH−CH=NH, a species that represents a higher level of in complexity compared to the previous members of the same chemical class already detected in the ISM. Measurements have been performed between 84 and 300 GHz, with the recording of 617 and 470 new rotational transitions for the two most stable *Ta* and *Ts* isomers, respectively. The resulting data sets were analysed using an *S*-reduced rotational Hamiltonian, yielding a very precise set of rotational constants, a full set of quartic coefficients, and some sextic centrifugal distortion coefficients. A number of lines showed resolvable hyperfine structure due to the quadrupole interaction of the ^{14}N nucleus with molecular rotation. For these transitions, each hyperfine component was accurately measured and analysed to determine the corresponding coupling coefficients. High-level theoretical calculations were performed to assist the spectral assignment and the analysis of the laboratory data. In particular,

ab initio values were used as suitable constraints for the Hamiltonian coefficients which could not be adjusted in the least-squares fit. Overall, the agreement between experimentally derived constants and the corresponding theoretical prediction is very good.

The new extensive set of spectroscopic parameters (see Table 2.2) was employed to generate catalogues of highly precise rest frequencies for the *Ta* and *Ts* isomers at millimetre wavelengths. These data were used to perform a search for allylimine emission lines in a spectral survey of the molecular cloud G+0.693 located in the CMZ. Eight transitions for each isomers have been tentatively assigned, leading to the derivation of the column densities $N = (1.5 \pm 0.6) \times 10^{13}\,\mathrm{cm}^{-2}$ for *Ta* and $N \sim 0.5 \times 10^{13}\,\mathrm{cm}^{-2}$ for *Ts*. These values are lower than those of the simpler related species cyanomethanimine and propargylimine, in agreement with the expected trend. The resulting [*Ta*]/[*Ts*] isomer ratio is ~ 3, much lower than the value of ~ 15 that can be estimated on the basis of thermodynamic considerations.

Chapter 3

A high-resolution spectroscopic analysis of aminoacrylonitrile and an interstellar search towards G+0.693

The contents of this chapter were published in *The Astrophysical Journal*.
Credit: Alberton et al., ApJ, 951, 108, 2023.

Abstract

Cyanides, ranging from three carbon atoms to PAHs, and alkenyl compounds are abundant in the interstellar medium (ISM). Aminoacrylonitrile (3-Amino-2-propenenitrile, $H_2N{-}CH{=}CH{-}C{\equiv}N$), an alkenyl cyanide, thus represents a promising candidate for new interstellar detection. A comprehensive spectroscopic laboratory investigation of Aminoacrylonitrile in its rotational ground vibrational state has been herein performed. The measurements carried out up to the THz regime made it possible to generate a precise set of reliable rest frequencies for its search in space up to sub-millimetre wavelengths. The *Z*-Aminoacrylonitrile (*Z*-APN) isomer spectrum has been recorded employing a source-modulated sub-millimetre spectrometer, from 80 GHz to 1 THz. A combination of Doppler and sub-Doppler regime measurements allowed to record 600 new lines. The collected data have enabled the characterisation of a set of spectroscopic parameters up to decic centrifugal distortion constants. The catalogue generated from the improved spectral data has been used for the search of *Z*-APN in the spectral survey of the G+0.693-0.027 molecular cloud located in the central molecular zone, in the proximity of the Galactic centre.

3.1 Introduction

Scientists have proposed many theories in order to explain the origin of life. According to one of the most widely accepted, it may have originated from the self-catalytic function of an RNA chain, an idea originally proposed by Gilbert 1986 and currently known as the RNA-world. How-

ever, how the RNA and subsequently life were formed still remains unknown. Among the various hypotheses, it is possible to distinguish two main lines of thought. Life could have emerged starting from precursors of biomolecular building blocks synthesised *in situ*, during our planet's cooling. Successive RNA polymerization could have then emerged in warm little ponds as a result of condensation of lightning synthesised abiotic precursors (Pearce et al. 2022), produced in a Urey-Miller experiment fashion (Miller 1953). Another hypothesis is that prebiotic compounds might have had an extraterrestrial origin. The prebiotic material could have been formed in the interstellar medium (ISM), and only successively delivered to Earth to give rise to more complex molecules (Oparin 1957, Chyba & Sagan 1992). Pristine building blocks synthesized in the ISM would have been inherited by interplanetary dust particles, comets, and meteorites that in later stages might have acted as carriers of those seeds essential for life ignition (Chyba et al. 1990, Altwegg et al. 2016b, Rivilla et al. 2020a). Only in the last stages, molecules might have started to self-organize and replicate.

Clues about prebiotic precursors' origin come from the composition of celestial bodies. Carbonaceous chondrites, considered among the youngest objects formed along with the formation of planetary systems, have been found rich in sugar-like compounds, long-chain monocarboxylic acids, amino acids, and nucleobases precursors, such as purines and pyrimidines (Stoks & Schwartz 1979, Pizzarello et al. 2006, Burton et al. 2012, Oba et al. 2022). Following the work by Bockelée-Morvan et al. (2000), further evidence of the partial inheritance of volatile composition from prestellar and protostellar evolution phases to cometesimals and planetesimals, came from the PILS[1] project. With the data therein obtained, Drozdovskaya et al. (2019) were able to outline the correlation existing among CHO-, N-, and S-bearing molecules between the low-mass protostar IRAS 16293-2422, a homologous of our protosolar system, and the bulk composition of the comet 67P/Churyumov-Gerasimenko. Analogously, Öberg et al. (2015) observed a correlation between abundances of interstellar Complex Organic Molecules (iCOMs) in comets and protoplanetary disks, and many detections of several key precursors of the RNA world sustain such an idea (e.g Zeng et al. 2019, Jiménez-Serra et al. 2020, Rivilla et al. 2022a).

Although the chemical processes of such systems are being studied extensively, our knowledge is still limited by what has been therein identified. Predictions of current abundances rely on observations, and since physical conditions are time-dependent we might still miss a large portion of information (Herbst & van Dishoeck 2009). The identification of new molecules can expand our chemical and physical insight of star-forming regions, and iCOMs have been proved to be excellent probes. Precise identification of ISM chemical species thus remains a crucial point to understand these environments.

In this study, we focused on 3-Amino-2-propenenitrile ($H_2N-CH=CH-C\equiv N$, Aminoacrylonitrile or APN, from here on), a promising candidate that could take part in the chemical network leading to amino-acids formation. Previous works (Miller & Orgel 1974; Sanchez et al. 1966; Kitadai & Maruyama 2018) suggested that in the liquid phase, this molecule might be one of the key steps leading to two α-amino acids Asparagine and Aspartic acid. APN is the adduct of ammonia to cyanoacetylene ($H-C\equiv C-CN$, firstly detected in space by Turner 1971), and is a member of the ISM well represented cyanide group. Cyanides represent one of the most

[1]Protostellar Interferometric Line Survey.

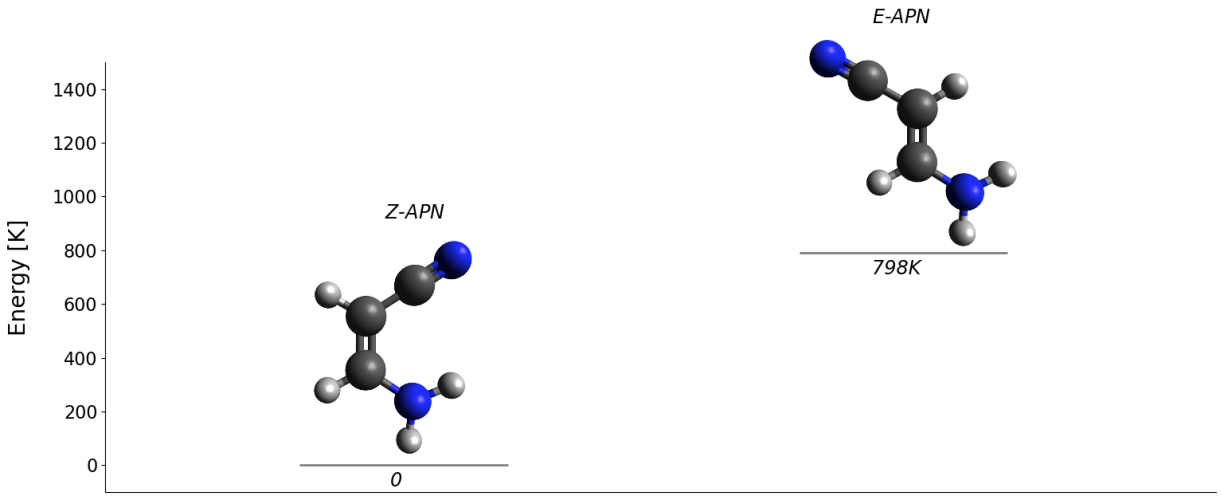

Figure 3.1: Energy level diagram of the two most stable isomers of 3-Amino-2-propenenitrile, *Z*-APN (left) and *E*-APN (right).

abundant families in the ISM, and a key molecular precursors of prebiotic chemistry (Rivilla et al. 2022c). In recent years several prebiotic species have been detected (e.g. cyanomethanimines by Zaleski et al. 2013b, Rivilla et al. 2019 and glyconitrile by Zeng et al. 2019). In 2021 alone, among closed shell molecules, 1-cyano-1,3-cyclopentadiene (c−C_5H_5CN, McCarthy et al. 2021), $HC_{11}N$ (Loomis et al. 2021), trans-cyanovinylacetylene and vinylcyanoacetylene (HC≡CCH=CHC≡N and H_2C=CHC_3N, respectively, Lee et al. 2021b), 2-cyanocyclopentadiene (C_5H_5CN, Lee et al. 2021a), cyano thioformaldehyde (HCSCN, Cernicharo et al. 2021) and cyanoacetyleneallene (H_2CCCHC_3N, Shingledecker et al. 2021) were detected; among open shell molecules, cyanomidyl radical (HNCN, Rivilla et al. 2021a), 3-cyano propargyl radical (CH_2CCCN, Cabezas et al. 2021) and Magnesium radicals (MgC_5N, Pardo et al. 2021) were detected.

The importance of APN comes also from its prochiral trait, i.e. it can be converted into new and different chiral molecules in a single chemical step. To date, only one chiral molecule has been detected in the ISM: propylene oxide (CH_3CHCH_2O, McGuire et al. 2016). Understanding the abundance of chiral molecules in space would make it possible also to explain the origin of enantiomeric abundance in meteorites (Pizzarello & Groy 2011; de Marcellus et al. 2011) and hopefully shed light on the emergence of l-amino acids abundance in living organisms.

The quiescent G+0.693-0.027 molecular clouds (hereafter G+0.693), located at the central molecular zone (CMZ) in the inner ~500pc of our Galaxy, has recently shown to be abundant in chemical species. Since 2019, it has been the subject of 13 new interstellar detections, including many cyanides (Rivilla et al. 2022c) and amines like NH_2OH (Rivilla et al. 2020b), ethanolamine (Rivilla et al. 2021c), vinyl and ethyl amine (Zeng et al. 2021). In a previous work carried out by Askeland et al. (2006), a low-frequency experiment characterised *Z*-APN isomer in the 4-80 GHz band. However, the excitation temperature (T_{ex}) found for most of the molecules in G+0.693 molecular cloud, is typically in the range 5-20 K (see e.g. Zeng et al. 2019). At a

temperature of 15 K, the *Z*-APN Planck function picks at almost 75 GHz, where one of the most intense transitions, the $34_{6-28} - 33_{6-27}$, has an uncertainty of almost 19 km s^{-1}. Not enough to guide an accurate search for this molecule in space. In the present work, we extended the spectroscopic characterisation of APN up to 1 THz. This frequency coverage and the accuracy of high resolution (43 kHz) spectroscopy measurements, allowed us to improve the precision of rotational and distortion constants producing a reliable catalogue for the search of this molecule not only in cold molecular clouds but in hotter ISM regions as well. It will therefore be possible to understand in which stages *Z*-APN might have formed and how chemical complexity can differ among the different phases of the star formation.

3.2 Experiment

The spectroscopic characterization of *Z*-APN, was conducted using the CASAC (Center for Astrochemical Studies Absorption Cell) spectrometer of the Center for Astrochemical Studies at the Max Planck Institute for Extraterrestrial Physics. The instrument has been described comprehensively in the introduction and only the distinctive features of the instrument are listed below.

The main radiation source of the CASAC spectrometer is a frequency synthesizer (Keysight E8257D) locked to a Rb atomic clock (Stanford Research Systems) operating at 10 MHz for accurate frequency and phase stabilisation. The radiation from the synthesizer is then coupled to a Virginia Diodes (VDI) solid-state active multiplier chain, providing continuous coverage across the 80–1600 GHz frequency range. The radiation is directed through a Pyrex tube of 3 m in length and 5 cm in diameter and is detected by a cryogenic-free magnetically enhanced InSb hot-electron bolometer (QMC Instruments Ltd.).

The frequency modulated signal is obtained by encoding the synthesizer radiation with a modulated sine-wave having a modulation width ranging from 100 to 600 kHz. A lock-in amplifier (SR830, Stanford Research Systems) is used for demodulating the detector output at twice the modulation frequency ($2f$) resulting in a second derivative profile of the absorption signal recorded by the computer-controlled acquisition system. *Z*-APN was measured letting its vapours directly flow through the absorption cell which was continuously pumped and kept at about 3-4 mTorr (0.5 Pa) and 300K.

3.3 Molecular properties

3-Amino-2-propenenitrile ($H_2N-CH=CH-C\equiv N$) is produced by the adduction of two ISM abundant molecules, ammonia (NH_3) and cyanoacetylene ($HC\equiv C-C\equiv N$). The reaction occurs both in solution (Xiang et al. 1994) or in gas phase (Guillemin et al. 1998), and leads in a yellow-brown mixture of *E* and *Z* isomers in a 1:1 ratio. After vacuum distillation at 63°C and 0.1 mbar, a colorless mixture of *E* and *Z* isomers was obtained in a 5:95 ratio (Benidar et al. 2005). APN is a disubstituted ethene ($H_2C=CH_2$), whose substituents are an amino ($-NH_2$) and a cyano group ($-CN$). Depending on the orientation of these two groups with respect to the sp^2 hybridized car-

bons, APN leads to two isomers. The most stable is denominated as *Z*-, and has the two sub-units oriented on the same side; *E*-APN, has the $-NH_2$ and $-CN$ moieties opposed to each other and is the less energetically favourable (Askeland et al. 2006). Figure 3.1 shows the energy diagram of the two isomers.

In order to estimate this energy difference, we herein conducted an all-electron ab-initio calculations at couple-cluster (CC) level of theory comprising a single, double, and a perturbed triple excitation treatment, i.e. CCSD(T). Employing a cc-pVTZ basis set, the estimated energy difference ΔE between *E* and *Z*-APN is $\Delta E = 6.63$ kJ mol $^{-1}$ (798K). These same ab-initio calculations allowed us to predict dipole moment components of *E*-APN, extending the contribution of Askeland et al. (2006) to *Z*-APN alone. The values of both isomers are reported in Table 3.1, and are expected to be $\mu_a = 5.92$ D, $\mu_b = 0.52$ D and $\mu_c = 0.82$ D and $\mu_a = 4.93(4)$ D and $\mu_b = 0.86(6)$ D, for *E*- and *Z*-APN, respectively. For all calculations we used CFOUR quantum chemistry package (Matthews et al. 2020). For the most energetically favoured isomer the inertial defect $\Delta = 0.0117$ is also presented, and indicates an almost molecular planarity, with Δ given by:

$$\Delta = I_c - I_b - I_a \tag{3.1}$$

Z- and *E*- isomers are both prolate symmetric top rotors and exhibit a Ray's asymmetry parameter $\kappa \approx -0.82$ and $\kappa \approx -0.99$, respectively (Ray 1932). In the current work, we will focus only on the *Z*- isomer, since this is the only species detected in our laboratory measurements.

3.4 Analysis

The high-resolution rotational spectrum of *Z*-APN was herein recorded from 80 GHz to 1.04 THz. 541 new lines were acquired, for a total of 687 components. 492 and 195 transitions belong to the *a*-type and *b*-type spectrum transitions, respectively. For the former, ${}^aR_{0,+1}$ branches were recorded, while for the latter both *R* and *Q* branches were observed. A summary of the different branches recorded is reported in Table 3.2. The principal quantum number *J* ranged from 12 to 117, and the first pseudo quantum number K_a from 0 up to 42.

Whether nitrogen is present in a molecule, quadrupole nuclear hyperfine splitting emerges due to the coupling between the ^{14}N nuclear quadrupole moment $I = 1$ and the end-over-end

Table 3.1: Relative energies and dipole moment components of the most stable APN isomers.

Parameter	Unit	*Z*	*E*
E	kJ/mol	0.0	6.63
μ_a	D	4.93	5.92
μ_b	D	0.86	0.52
μ_c	D	0.0	0.82
κ^1		0.82	0.99

Notes. [1] κ is the asymmetric rotor parameter, given by $(2B - A - C)/(A - C)$ (Gordy & Cook 1984). μ_x is the dipole moment with respect to the *x* inertia axis.

Table 3.2: Transitions and components recorded for Z-APN in this work.

Type	Branches[1]	No. of components	No. of lines
a-type	${}^{a}R_{0,+1}$	492	390
b-type	${}^{b}R_{+1,+1}$	46	35
	${}^{b}R_{+1,-1}$	32	15
	${}^{b}R_{-1,+1}$	7	7
	${}^{b}Q_{+1,-1}$	110	94

Notes. [1] The branch symbol ${}^{x}M_{\delta_{K_a},\delta_{K_c}}$ refers to the transition type of an asymmetric rotor. x stands for the component of the dipole moment, $M = P, Q, R$ for transitions with $\Delta J = -1, 0, +1$, respectively, and δK_a and δK_c for the (signed) change of the K_a and K_c pseudo-angular quantum numbers (Gordy & Cook 1984).

molecular rotation. The hyperfine splitting of a given transition goes with $\Delta_Q \sim -6K^2/J^3$ (Townes & Schawlow 1975). The transition with the lower principle quantum number recorded in the present work has $J = 12$, around 80 GHz, and no hyperfine features were present. Hyperfine parameters were hence not improved or affected by our measurements, therefore those determined by Askeland et al. (2006) were maintained.

Most of the transitions were recorded at a pressure of $\sim$ 4 mTorr at 300 K, but in a few cases, some lines were blended. Among the various contributions that affect line shape and line width[2], a substantial role is played by the Doppler broadening effect, a consequence of the Maxwellian distribution of molecular velocities. For electromagnetic radiation tuned at the molecular resonance ν_1, only those molecules having no velocity component along the line of incident radiation will resonate with such frequency. Instead, molecules having a non-zero velocity component along this same axis (in the case in which $v_z \ll c$, where c = speed of light), will resonate with frequencies given by

$$\nu = \nu_1\left(1 + \frac{v_z}{c}\right) \tag{3.2}$$

The radiation having frequency ν will then resonate with all those molecules having a velocity along the radiation pathway of

$$v_z = \left(\frac{\nu - \nu_1}{\nu_1}\right)c \tag{3.3}$$

As theoretically pointed out by Lamb (1964), a power saturation of a Doppler-broadened line can produce a sharp dip whenever other broadening factors are small in comparison with Doppler broadening and there is a radiation linearly passing in opposite direction of the gas flow (Winton & Gordy 1970). In the present work, the difference of one order of magnitude in pressure obtained passing from the routinely Doppler-limited conditions of few mTorr to 0.2-0.3 mTorr (sub-Doppler regime), allowed to reduce pressure-broadening effects, enabling the saturation of the transition that occurs at frequency ν_1. The subsequent interaction with the radiation reflected

[2] An important contribution arises due to pressure broadening, other minor ones for power effects, collisions between molecules and cell walls, and distortion introduced by modulators, detectors, and amplifiers.

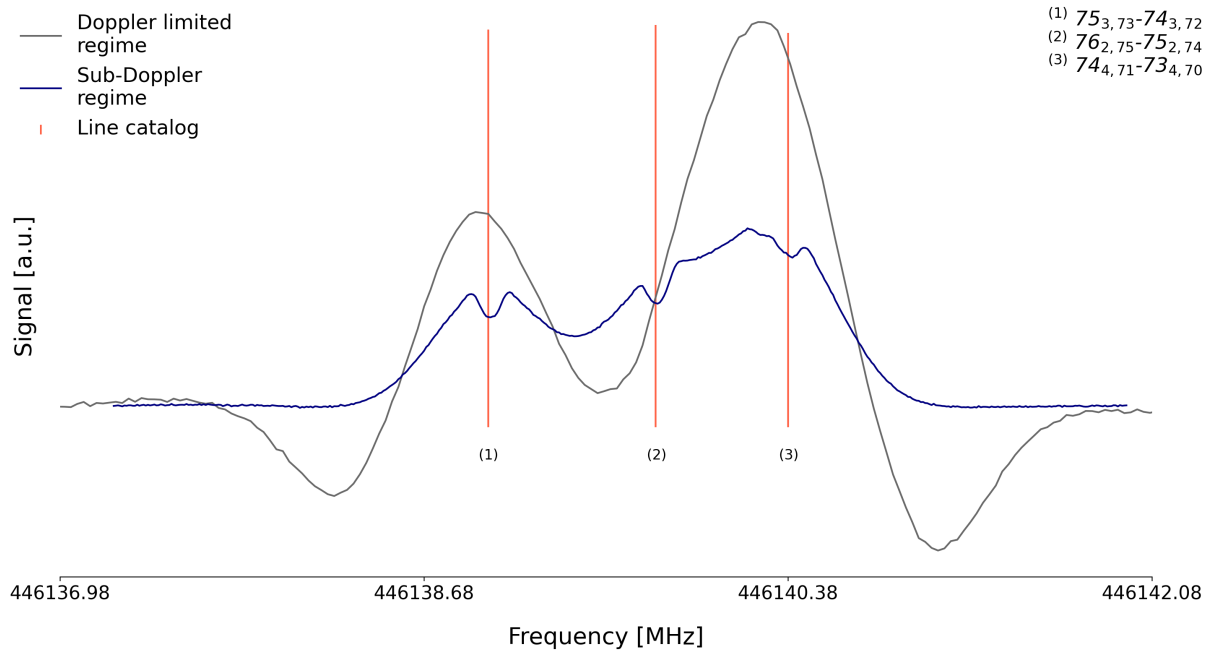

Figure 3.2: Doppler and Sub-Doppler measurements comparison for *a*-type *Z*-APN isomer transitions $J'_{K'_a,K'_c}$-J_{K_a,K_c} = 75_{3-73}-74_{3-72}, 76_{2-75}-75_{2-74} and 74_{4-71}-73_{4-70}. For the Sub-Doppler regime, modulation width: 100 kHz; modulation frequency: 15 kHz; total integration time: 555 s. For Doppler-limited conditions, modulation width: 600 kHz; modulation frequency: 40kHz total; total integration time: 88s.

by the bottom lens of the absorption cell results in a stimulated emission identifiable by the appearance of a dip in the absorption $2f$ profile, in correspondence of ν_1. Such low pressures are also important to induce an appreciable separation of the dips from the Doppler profile as well as to minimise possible pressure line shifts (Cazzoli et al. 2003).

In Fig. 3.2, the experimental data recorded under the sub-Doppler regime, are shown in blue. In the course of the analysis, the shape of the rightmost line led us to suspect that it was the result of multiple unresolved components, a fact also supported by the predictions obtained from the fit up to that point. By switching to a Lamb-dip regime (blue line), it was possible to resolve and assign both lines $J_{Ka,Kc}$ = $75_{3,73}$-$74_{3,72}$ and $76_{2,75}$-$75_{2,74}$, which were then included into the fit. The measured line widths at full width at half maximum (FWHM) of the transition 75_{3-73}-74_{3-72} passed from 640 kHz to 97 kHz. This same procedure was performed to deal with comparable situations, and in combination with sub-Doppler regime analysis allows us to record transitions up to 1 THz. Fig. 3.3 shows the transition obtained at the highest frequency, 1.04 THz. Residuals of this line fitting are in good agreement with the Voigt profile fitted using the line profile with our in-house analysis software, that implements the $2f$ Voigt profiles presented by Dore (2003).

The new lines were fitted including the ones recorded by Askeland et al. (2006), using the

Table 3.3: Spectroscopic constants determined for *Z*-APN[a].

This work			Askeland et al. (2006)	
S-Watson reduction[b]		unit	A-Watson reduction[b]	
A	12583.10077(34)	MHz	12583.056(35)	A
B	3766.112892(87)	MHz	3766.1252(31)	B
C	2896.390356(74)	MHz	2896.3784(28)	C
D_J	4.234231(24)	kHz	4.416(17)	Δ_J
D_{JK}	-30.07919(29)	kHz	-31.068(98)	Δ_{JK}
D_K	92.21050(82)	kHz	46.0(35)	Δ_K
d_1	-1.4546068(18)	kHz	1.4487(52)	δ_J
d_2	-0.098562(11)	kHz	6.4(14)	δ_K
H_J	0.0165114(44)	Hz		
H_{JK}	-0.111108(72)	Hz		
H_{KJ}	-0.41083(56)	Hz		
H_K	2.38799(72)	Hz		
h_1	8.5609(32)	mHz		
h_2	1.3110(27)	mHz		
h_3	0.3110(11)	mHz		
L_J	-0.05557(22)	μHz		
L_{JJK}	0.8048(33)	μHz		
L_{JK}	-6.399(32)	μHz		
L_{KKJ}	0.03051(27)	mHz		
L_K	-0.08425(26)	mHz		
l_1	-0.03135(16)	μHz		
l_2	5.24(15)	nHz		
l_3	-4.681(79)	nHz		
l_4	-0.942(21)	nHz		
χ_{aa} (NH_2)	1.7262	MHz	1.7262	
$\chi_{bb} - \chi_{cc}$ (NH_2)	6.3919	MHz	6.3919	
χ_{aa} (CN)	-1.4917	MHz	-1.4917	
$\chi_{bb} - \chi_{cc}$ (CN)	-1.6371	MHz	-1.6371	
$\sigma_{\rm rms}$	44	kHz		
$\sigma_{\rm w}$	1.18		2.22	
No. of lines	935		86	

Notes. [a] Numbers in parentheses represent the 1σ standard deviation of the constant in the unit of the last digit. Unitless weighted deviation $\sigma_{\rm rms}$ of the fit higher than 1 assigns an uncertainty greater than the 67% confidence level. [b] The parameters employed pertain to the I^r representation. For a direct comparison between S- and A- Watson's reduction, refer to Gordy & Cook (1984).

SPFIT/SPCAT software. Figures 3.4 shows the simulated spectra computed at 300 K and 10 K, obtained with the new rotational and distortion constants, presented in Table 3.3. In contrast to the latter work, we used the S Watson's reduction asymmetric Hamiltonian, maintaining the I^r

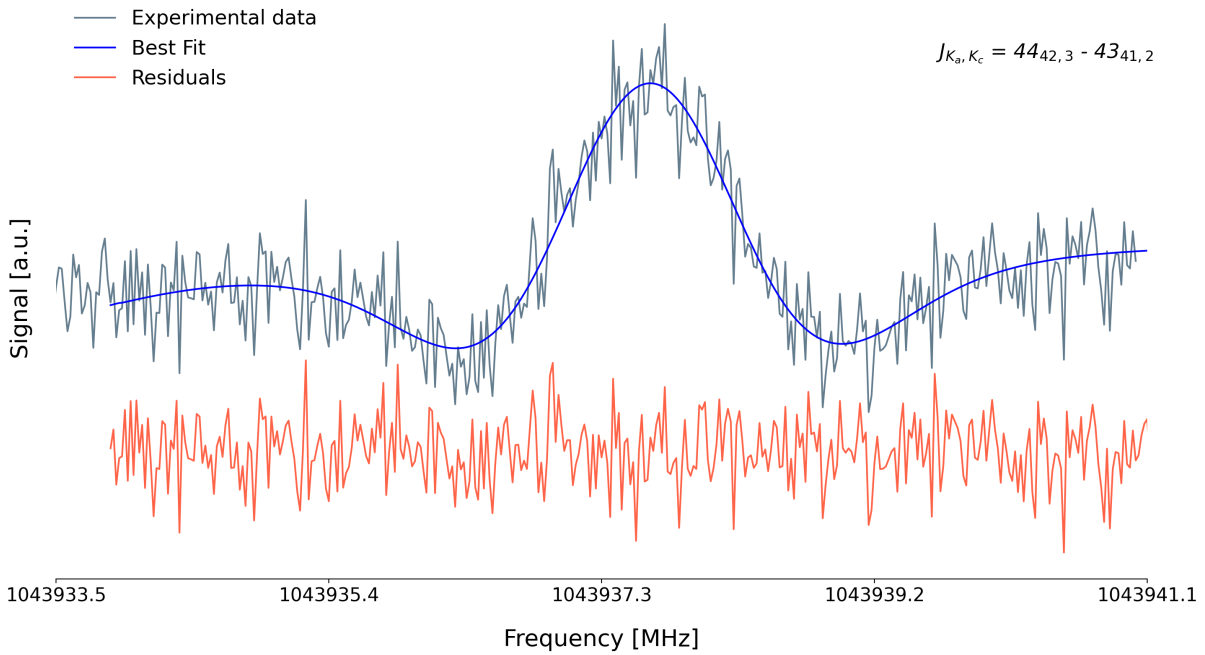

Figure 3.3: A detail of a *b*-type *Z*-APN transition recorded at 1.04 THz. The line profile is a Voigt profile. In grey is the experimental data, in blue is the best fit, and in red are the residuals. Integration time: 4 minutes; modulation width: 800 kHz; frequency step: 30 kHz.

Table 3.4: Transitions and components recorded for Z-APN in this work.

Parameter	unit	Value
Bz–Bx–By	MHz	18503.7
Bx–By	MHz	869.7
R5	kHz	4.726
R6	kHz	5.315
$s_{111}(A)$		0.024
$s_{111}(S)$		0.0005

Notes. List of parameters used to choose the Hamiltonian reduction type to employ in the fitting procedure. To have a straightforward comparison, nomenclature has been taken verbatim from (Margulès et al. 2010). For our purpose, B_z, B_x, and B_y correspond to the rotational constants A, B, and C, respectively; R_5 and R_6 are obtained with CFOUR software and are given by combinations of distortion constants and are used to compute the free s_{111} parameter. The latter take part in the Hamiltonian unitary transformation.

representation. This was done to keep the free parameter s_{111}, which takes part in the unitary transformation of the Hamiltonian, the lowest as possible, as suggested by Watson (1978a). This way, the convergence of the fit is sped up and additional terms in the Hamiltonian can be avoided (Margulès et al. 2010). In Table 3.4 the values used to determine the constants $s_{111}(A)$ and

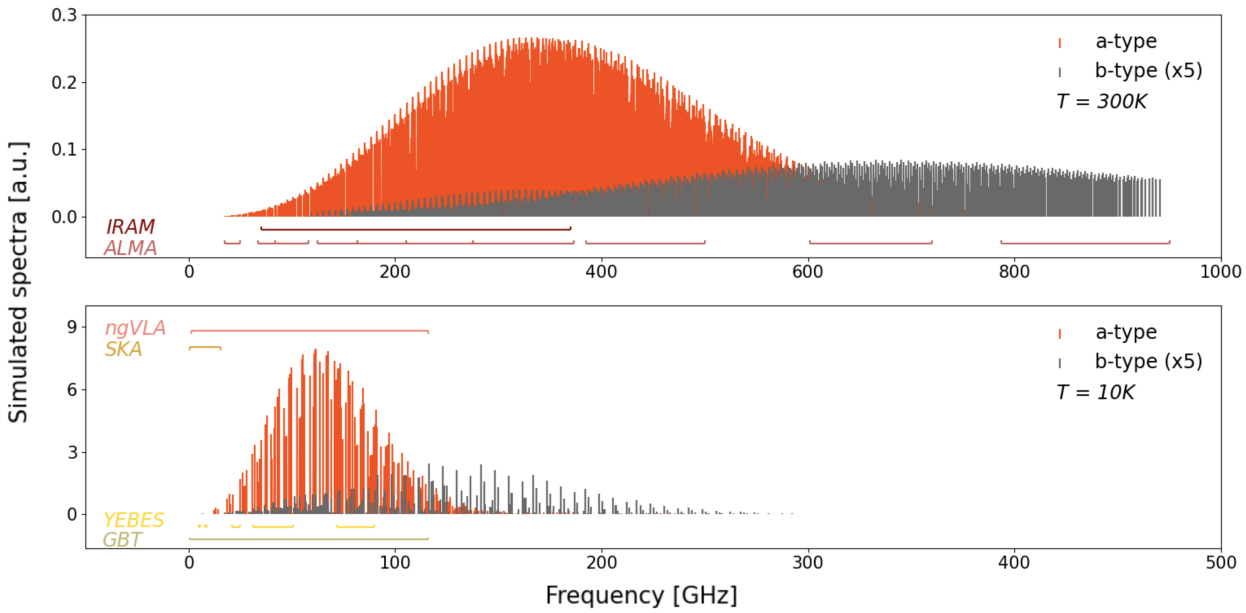

Figure 3.4: Simulated spectra of *Z*-APN. In red and gray, a-type and b-type transition spectra, respectively. The upper and lower panels are showing the spectra computed at 300 K and 10 K, respectively. The x- and y-axis values were chosen to take into account the shift in the Planck function. To note, the spectrum at 300 K has a frequency span of three times and an intensity of one-thirtieth compared to the spectrum at 10 K. [a.u.] stays for arbitrary units.

$s_{111}(S)$ are listed, showing a difference of 50 between the former and the latter, respectively. The fit was performed by assigning transitions with gradually increasing quantum numbers J and K_a. Distortion constants were added in the process in order to account for the divergence due to their increasing values and the corresponding frequencies.

All 687 rotational transitions, including the ones observed in the previous microwave experiment, were reproduced by our model with a final rms uncertainty of 44 kHz. The uncertainty of the new rotational constants has been decreased by a factor of 1000 for A, and more than 40 for both B and C. A full set of quartic, sextic and octic distortion constants[3] with an average uncertainty of 0.003%, 0.1% and 1%, respectively, were determined. For the old lines, the same experimental uncertainties attributed by the authors σ= 3 kHz and σ=50 kHz were used, for the hyperfine transitions recorded with the Fourier transform spectrometer and Stark spectrometer, respectively. Depending on experimental conditions, line-width and S/N ratio, σ ranging from 25 to 50 kHz, were assigned for the transitions recorded in this work.

Rotational (Q_{rot}) partition functions for *Z*-APN are provided in Table 3.5. The values have been computed for T = 2.725 – 1000 K and are obtained by direct summation over the rotational or hyperfine levels, whose energies have been accurately determined from the spectral analysis. The vibrational partition functions $Q_{\rm vib}$ have been computed using harmonic frequencies at the CCSD(T)/cc-pVTZ level of theory, calculated in this work using CFOUR software (Matthews

[3]Due to fit, the only excluded octic constants was l_2.

et al. 2020). Ab-initio calculation to assist the measurements to determine also the rotational constants of *E*-APN are planned.

Table 3.5: Rotational, hyperfine, and vibrational partition functions for *Z*-APN.

T [K]	Q_{rot}	Q_{HFS}	Q_{vib}
2.725	65.85	592.64	1.0000
5.0	162.39	1461.56	1.0000
9.375	415.16	3736.44	1.0000
18.75	1171.51	10543.61	1.0000
37.5	3310.39	29793.53	1.0059
75.0	9362.80	84265.20	1.0869
150	26502.93	238526.14	1.5175
225	48674.53	438064.39	2.4062
300	74545.76	670880.28	4.1258
500	152098.4	1368680.8	21.055
1000	328071.4	2951911.5	1381.5

3.5 Interstellar search towards the G+0.693-0.027 molecular cloud

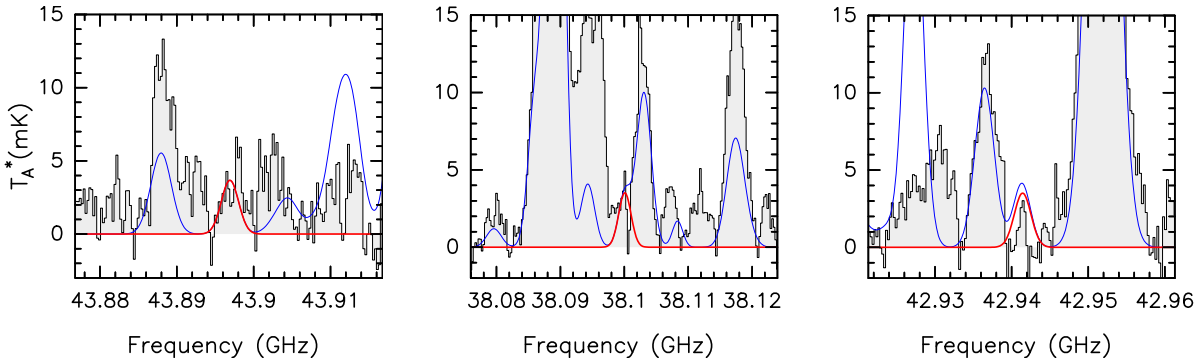

Figure 3.5: Transitions of *Z*-APN used to compute the column density upper limit towards G+0.693 (see text). The black line and gray histogram show the observed spectrum, the red curve is the LTE synthetic model of *Z*-APN using the column density upper limit derived toward G+0.693, and the blue curve indicates the emission of all the molecules previously identified towards the source.

We searched for *Z*-APN towards the G+0.693-0.027 molecular cloud, located in the Sgr B2 region of the Galactic Center. Several molecular species, including cyanides, have been recently

detected for the first time toward this cloud (see e.g. Rivilla et al. 2019; Rivilla et al. 2020b; Bizzocchi et al. 2020; Rivilla et al. 2021c,b, 2022a,b; Rodríguez-Almeida et al. 2021a,b; Zeng et al. 2021; Jiménez-Serra et al. 2022b). We used a sensitive unbiased spectral survey performed with the Yebes 40m (Guadalajara, Spain), and the IRAM 30m (Granada, Spain) telescopes. The position switching observations were centered at α(J2000.0)= $17^{h}47^{m}22^{s}$, δ(J2000.0)= $-28°21'27''$. The line intensity of the spectra was measured in units of T_{A}^{*} as the molecular emission toward G+0.693 is extended over the beam (Requena-Torres et al. 2006, 2008; Zeng et al. 2018, 2020b). For more detailed information of the observational survey we refer to Rivilla et al. (2021c) and Rivilla et al. (2022d).

We implemented the spectroscopic entry of *Z*-APN (without considering HFS) from this work into the MADCUBA package[4] (version 28/10/2022; Martín et al. 2019b). Using the SLIM (Spectral Line Identification and Modeling) tool of MADCUBA, we generated a synthetic spectra of *Z*-APN under the assumption of Local Thermodynamic Equilibrium (LTE), and compare with the observed spectra. We used typical values of the physical parameters found in G+0.693: T_{ex}=8 K, v_{LSR}=69 km s^{-1} and FWHM=18 km s^{-1}. We show in Figure 3.5 the brightest transitions according to the LTE model that fall in the spectral range covered by the survey[5]: $7_{0,7}-6_{0,6}$ at 43.896761 GHz, $6_{0,6}-5_{0,5}$ at 38.09996 GHz, and $7_{1,7}-6_{1,6}$ at 42.94129 GHz. Although the LTE model is compatible with the observed spectra, we did not detect clear unblended transitions that would allow a secure detection of the molecule. For this reason, we report here an upper limit for its molecular abundance. To derive it we have used the higher value of the column density (N) whose LTE model is compatible with the observed spectrum, as shown with a red curve in Figure 3.5). We obtained $N < 6.6\times10^{12}$ cm^{-2}, which means an abundance compared to H_2 of 4.9×10^{-11}, using $N(H_2)=1.35\times10^{23}$ cm^{-2} (Martín et al. 2008).

3.6 Discussion

In this work we focused on the ground vibrational state of the lowest energetic isomer *Z*-APN. As it was already seen in the cyanides detected in G+0.693, the isomers ratio is unfavourable for the highest energy isomer (look i.e. Rivilla et al. 2019). Therefore, the probabilities to detect the highest energy isomer *E*-APN, instead of the most stable *Z*- isomer, are scarce. Nevertheless, the additional spectroscopic characterisation of the most energetic isomer might help to shed light on the isomer ratio of this molecule in the ISM whether higher sensitivity measurements might be available. As far as rotational spectroscopy is concerned, any molecular system can be described by its angular momentum. The latter is inversely proportional to the rotational constants *A*, *B* and *C*, determined for *Z*-APN, and to be determined for *E*-APN. For spectroscopic complex molecules such as iCOMs, the associated high moment of inertia results in low rotational constants. In the case of *Z*-APN, the fundamental 1-0 transition, given as for all prolate asymmetric rotors by the sum of the rotational constants *B* and *C*, is at approximately 6 GHz. Due to the sim-

[4]Madrid Data Cube Analysis on ImageJ is a software developed at the Center of Astrobiology (CAB) in Madrid; http://cab.inta-csic.es/madcuba/

[5]We have excluded the transition $8_{0,8}-7_{0,7}$ at 49.621278 GHz, because it is completely blended with a brighter transition of Z-cyanomethanimine (Z-HNCHCN; Rivilla et al. 2019).

ilarity in geometry and atom compositions, one can expect a similar value for *E* isomer. Being the fundamental rotational level, it has no associated centrifugal distortion, and is the ideal target when beginning to assign a spectrum for which no prior experimental information is available. For *Z*-APN, it was possible to work nimbly with the CASAC at 300 K because we started from Askeland et al. (2006)'s work, but for *E*-APN, the same does not apply. The analysis would start from rotational constants obtained from ab-initio calculations, which always have an intrinsic uncertainty associated. On top of this, the effects of centrifugal distortions taking place in higher quantum number transitions make the identification very complex. Therefore, the Free-Unit Jet experiment is the ideal candidate to begin the assignment of complex molecules starting from ab-initio calculations, for molecules such as *E*-APN.

The upper limit of $N < 6.6\times10^{12}$ cm^{-2} herein obtained (abundance compared to H_2 of 4.9×10^{-11}, with $N(H_2)=1.35\times10^{23}$ cm^{-2}) can let us compare this upper limit of *Z*-APN with the molecular column densities of simpler cyanides and amines already detected towards G+0.693. Cyanides with two carbon atoms, such as vinylcyanide (C_2H_3CN) and ethylcyanide (C_2H_5CN), are more abundant than *Z*-APN by factors of $\gtrsim$14 and $\gtrsim$6, respectively (Zeng et al. 2018), while the two-carbon amines vinylamine ($C_2H_3NH_2$) and ethylamine ($C_2H_5NH_2$) are more abundant by factors of $\gtrsim$7 and $\gtrsim$4, respectively (Zeng et al. 2021). This indicates that the increase of molecular complexity that involves an additional carbon and nitrogen atom implies a drop in molecular abundance of at least one order of magnitude.

3.7 Conclusions

We herein characterized the high-resolution rotational spectrum of *Z*-APN from 80 GHz to 1.04 THz. In the experiment we employed both Doppler and sub-Doppler regime measurements, allowing us to record 541 new lines. With the new *Z*-APN catalogue produced making use of the new rotational constants we searched for this molecule in the G+0.693 molecular cloud. Under LTE condition, we report an upper limit for its column density of $N < 6.6\times10^{12}$ cm^{-2}, which means an abundance compared to H_2 of 4.9×10^{-11}. Further analysis might include the characterisation of the *E*-APN and the search for both isomers in colder sources as well, i.e. L1544 or L183, to help us to better understand the underlying astrochemical link existing between different phases of the star formation regions.

Chapter 4

Accurate ab initio spectroscopic studies of promising interstellar ethanolamine iminic precursors

The contents of this chapter are currently being published in the *Astronomy & Astrophysics* Journal. Credit: Alberton et al., A&A, forthcoming article.

Abstract

The detection of $NH_2CH_2CH_2OH$ (ethanolamine) in G+0.693-0.027 molecular cloud adds an additional player to the prebiotic molecules discovered so far in the interstellar medium (ISM). As this molecule might be formed through condensed-phase hydrogenation steps, detecting one or more of the molecules involved might help to elucidate the chemical pathway leading to its production. The chemical path involves the formation of four chemical species. In this work, we study the energies of the isomers involved, indicate the best candidates for detection purposes, and provide the distortion constants of the most energetically favoured isomers undetected so far. We used highly accurate CCSD(T)-F12/cc-pCVTZ-F12 computations to predict the lowest energy isomers as well as their spectroscopic constants, taking corrections for core electron correlation and scalar relativity into account. We studied 14 isomers. We find that the lowest energy isomer proposed in previous studies is not the actual minimum. We provide a set of rotational and distortion constants of the two new most stable isomers together with their fundamental vibrational frequencies in order to guide the search for these important astrochemical precursors of prebiotic molecules in the ISM.

4.1 Introduction

The desire to understand the molecular origins of life is one of the main drivers for contemporary astrochemical research. In the era of modern space telescopes such as JWST, the amount

of data being provided by such observations will undoubtedly enable new and unprecedented discoveries (Gardner et al. 2006). While this new telescope is bringing significant new insights for the infrared (IR) Universe, lower-frequency observations including stalwart ground-based radioastronomical rotational spectra will continue to contribute to the field. Radioastronomy provides insight into where complex chemistry emerges and begins to play its role in the evolution that spans from molecular clouds to habitable planets. Additionally, an increasing number of molecules are employed as molecular tracers, such as CO and N_2H^+, which are used to trace H_2 and N_2, respectively (Bergin et al. 2001), and many more tracers might be employed. Such observations are providing a wider picture of the physical evolution of star forming regions, but the chemical processes occurring along the steps that ultimately brought about life are less well understood.

The basic cellular functions for life as we know it are carried out by four classes of molecules. These classes consist of lipids, sugars, amino acids, and nucleic acids. These molecules are in turn mainly formed by hydrogen, carbon, oxygen, nitrogen, and sulphur. Other elements play crucial roles, but their abundances are minor when compared to these latter five. The idea that these molecules are inherited from the primordial stage of star formation of our Sun is supported by the correlation existing among CHO-, N-, and S-bearing prebiotic molecules detected in the low-mass protostar IRAS 16293-2422 and the bulk composition of the comet 67P/Churyumov-Gerasimenko [1] (Drozdovskaya et al. 2019). The relation that exists between the abundances of interstellar complex organic molecules (COMs, Herbst & van Dishoeck 2009) observed in comets and in protoplanetary discs (Öberg et al. 2015) further supports this idea.

The chemical complexity found in the Murchison and other meteorites (Burton et al. 2012; Pizzarello et al. 2006; Oba et al. 2022) also supports the formation of prebiotic molecules in space, but does not prove causation. As asteroids and planetesimals —from which meteorites originate— grew in size, they underwent secondary alteration events. Also known as post-accretion events, these latter provide additional opportunities for chemical reactions, either directly from thermal energy (thermal metamorphism; Huss et al. 2006) or from liquid water (aqueous alteration; Brearley 2006) resulting from melting water ices. However, the alteration of these bodies makes it difficult to decipher the exact point at which the prebiotic molecules were formed in the ISM, making direct detection the only effective way to determine their presence in space.

Many prebiotic molecules have been detected in the ISM, and both the number and complexity of those that are defined as COMs are sharply increasing (McGuire 2022). Precursors of sugars, such as (Z)-1,2-ethenediol (OHCH=CHOH, Rivilla et al. 2022a) and glycolaldehyde ($HOCH_2CHO$, Hollis et al. 2000, 2004); nucleobases such as hydroxylamine (NH_2OH, Rivilla et al. 2020b) and urea ($CO(NH_2)_2$, Belloche et al. 2019; Jiménez-Serra et al. 2020); and amino acid precursors such as acetonitrile (CH_3CN, Belloche et al. 2008), vinylamine, ethylamine ($H_2C{=}CHNH_2$ and $CH_3CH_2NH_2$, Zeng et al. 2021), and syn-glycolamide ($NH_2C(O)CH_2OH$, Rivilla et al. 2023) have been detected in various astronomical regions. Furthermore, n-propanol ($CH_3CH_2CH_2OH$, Jiménez-Serra et al. 2022a) and ethanolamine ($NH_2CH_2CH_2OH$, Rivilla et al. 2021c) were recently detected in the G+0.693-0.027 molecular cloud (hereafter referred to as

[1] IRAS 16293-2422 is a homologous to our protosolar system, while the comet 67P/Churyumov-Gerasimenko represents one of the most primitive material of our Solar System.

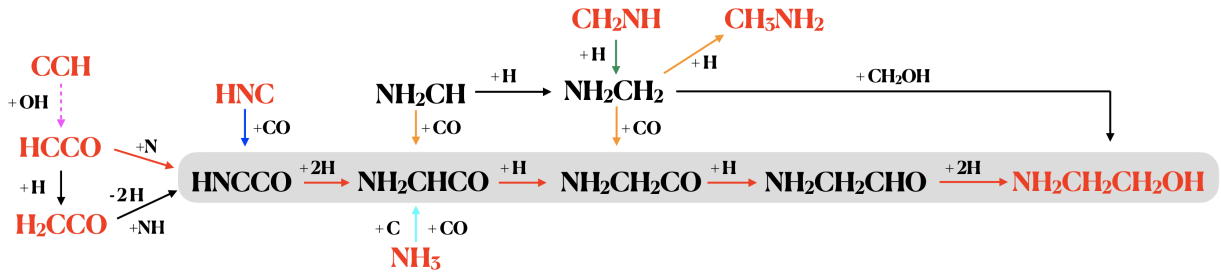

Figure 4.1: Figure taken from Rivilla et al. (2021c). The molecular species in red have been detected towards the G+0.693 molecular cloud. The grey-shaded area corresponds to a hydrogenation chain. The chemical reactions indicated with coloured arrows have been proposed in previous works: magenta (Wakelam et al. 2015), blue (Kameneva et al. 2017), orange (Suzuki et al. 2018), cyan (Krasnokutski 2021), and green (Suzuki et al. 2018; Ruaud et al. 2015). The formation routes proposed in Rivilla et al. (2021c) are shown in black. The solid arrows indicate surface chemistry reactions, dashed arrows denote gas phase chemistry.

G+0.693) and are considered to be key components in the formation of phospholipids.

While its origin is not known, ethanolamine (hereafter EtA) alone accounts for 25% of one of the two molecular subunits that form terrestrial phospholipids and has also been found in the Almahata Sitta meteorite (Glavin et al. 2010). Here, its original formation might be ascribed to thermal decomposition of amino acids due to unusual conditions to which the parent asteroid might have been exposed. Grain-surface chemistry already showed that this prebiotic molecule can be formed through UV irradiation of interstellar ice analogues (Ruaud et al. 2015) and Rivilla et al. (2021c) suggested that EtA might have formed through subsequent solid-phase hydrogenation steps. In this latter work, the authors mentioned that EtA formation might have involved the NH_2CH_2 radical, a result of NH_2CH hydrogenation. As extensively explained there, recent laboratory experiments (Fedoseev et al. 2015; Ioppolo et al. 2021) showed that the intermediate radicals NH_2CH_2 and hydroxymethyl CH_2OH, leading respectively to methylamine (CH_3NH_2) and methanol (CH_3OH), are efficiently formed in the hydrogenation reactions and have been proposed as viable routes to the formation of COMs Garrod & Herbst (2006); Garrod et al. (2008); Garrod (2013). CH_2OH has been shown to play a significant role in the cold surface hydrogenation of CO molecules without involvement of UV- or cosmic-ray energetic processing of interstellar ices at 15 K, leading to glycolaldehyde ($HC(O)CH_2OH$), ethylene glycol ($H_2C(OH)CH_2OH$) Fedoseev et al. (2015), and methyl formate ($HC(O)OCH_3$) Chuang et al. (2016). Non-diffusive reactions between NH_2CH_2 and CH_2OH might therefore lead to EtA on dust grains Rivilla et al. (2021c). Additionally, EtA might also be formed through the hydrogenation of NH_2CH_2CO, as a product of the reactions involving NH_2CH_2 and CO Suzuki et al. (2018). On the other hand, in order to extend our comprehension of the chemical pathways leading to EtA and reported in Figure 4.1, it would be helpful to also search the ISM for the intermediates highlighted in grey in that figure, specifically in regions where they might migrate from the dust particles to the gas phase. Until now, it appears that the fewer atoms there are in a given molecule, the higher the probability of its detection in space (McGuire 2022). It therefore seems reasonable to begin an

investigation of this proposed mechanism in ascending order of atoms involved.

Referring to Figure 4.1, HNCCO (iminoethenone) might be formed through solid-phase N-addition to the ketenyl radical (HCCO) (Charnley 2002), which is formed in the gas-phase reaction CCH + OH (Wakelam et al. 2015). Another route implies dust-grain surface reaction of ketene (H_2CCO) after two hydrogen abstractions, possibly reacting with the imine radical NH (Rivilla et al. 2021a). Nevertheless, Flammang et al. (1994) argue that the probability of detecting HNCCO in the gas phase is low given its tendency to easily decompose into HNC + CO. While this tendency to decompose might not be a problem in the ISM, it is in laboratory conditions, where the chemical production of HNCCO needs to be sufficiently stable in order to allow characterisation of its rotational spectrum.

Regarding NH_2CH_2CO, the number of atoms, the presence of nitrogen, and the fact that it presents an open-shell electronic configuration further weaken the rationale for it to be a primary target for rotational spectroscopic studies. Instead, the aldehyde analogue NH_2CH_2CHO, which is a closed-shell molecule, has an additional hydrogen atom that confers a more pliable molecular structure, increasing the number of internal rotations and consequently decreasing the partition function and its line intensities. Therefore, our first reasonable target should be NH_2CHCO.

Whether or not HNCCO is produced in the condensed phase, it might in fact lead to NH_2CHCO, which is also proposed to be the product occurring between the barrierless reaction of NH_3, CO, and atomic C (Krasnokutski 2021). As the abundance of free carbon atoms is around half that of CO (Tanaka et al. 2011) in the molecular clouds of the Galactic centre, this route could contribute to the formation of NH_2CHCO in G+0.693. Although three-body reactions are less efficient than two-body reactions in the ISM, the fact that carbon atoms are expected to be highly reactive favours this scenario. The barrierless NH_2CH + CO reaction proposed by Suzuki et al. (2018) might also contribute to the formation of NH_2CHCO in various astrophysical regions.

In recent years, the number of amines detected in space has been rapidly increasing, undermining the idea that imines are the most abundant N-bearing molecules after cyanides. So far, in addition to EtA, methylamine (CH_3NH_2, Kaifu et al. 1974), hydroxylamine (NH_2OH, Rivilla et al. 2020b), and vynilamine ($C_2H_3NH_2$, Zeng et al. 2021) have been detected and ethylamine ($C_2H_5NH_2$, Zeng et al. 2021) has been tentatively detected. Among imines, methanimine (CH_2NH, Godfrey et al. 1973), E-cyanomethanimine (HNCHCN, Zaleski et al. 2013), prapargylimine (HC_3HNH, Bizzocchi et al. 2020), and ethanimine (CH_3CHCN, Loomis et al. 2013b) have also been detected. Ketenimine (CH_2CNH, Lovas et al. 2006), aziridine (C_2H_5N, Dickens et al. 2001), and allylimine ($CH_2CHCHNH$, Alberton et al. 2023) have been tentatively detected, while an upper limit has been reported for propanimine (CH_3CH_2CHNH, Margulès et al. 2022). In a recent paper, Krasnokutski et al. (2022) tackled the formation pathway of NH_2CHCO and presented evidence for its formation in a 10K ice mixture in amine form.

Nevertheless, the information obtained with the level of theory previously employed (Krasnokutski et al. 2022) can be improved with higher level calculations. Additionally, this latter analysis (see also Krasnokutski 2021) does not explore the entire breadth of possible isomers for this molecule, most notably not reporting the iminic form. While NH_2CHCO may be required for the reactions as given in Figure 4.1, if this isomer easily breaks down into other forms, it will not be available to provide the chemistry as proposed. Therefore, this present work explores NH_2CHCO isomers and also provides theoretical spectral data for their characterisation in the

laboratory. This is the first step for possible analysis of their presence in space, providing insight into interstellar prebiotic chemistry.

4.2 Computational details

The theoretical computations performed in this work employ Gaussian09 (Frisch et al. 2009), MOLPRO (2015.1 version)[2] (Werner et al. 2015; Werner et al. 2020), CFOUR (2.1-serial version[3]) (Matthews et al. 2020), and SPECTRO (Gaw et al. 1991; Westbrook & Fortenberry 2023), this latter being a perturbational code to produce the final spectroscopic data. The scans of the potential energy surface (PES) of the NH_2CHCO isomers were performed employing Gaussian and MOLPRO. We employed the B3LYP (Lee et al. 1988; Becke 1993) hybrid functional theory and Møller–Plesset perturbation theory up to the second order (MP2, Møller & Plesset 1934) in conjunction with the 6-311+G(d,p) basis set (Andersson & Uvdal 2005) and the CCSD(T)-F12/UCCSD(T)-F12 level of theory (Knizia et al. 2009a; Adler et al. 2007) using the cc-pCVTZ-F12 basis set (Hill et al. 2010). All isomer geometries are optimised with CCSD(T)-F12/cc-pCVTZ-F12.

Spectroscopic constants are obtained using CFOUR and a MOLPRO-SPECTRO combination. CFOUR utilises the CCSD(T)/cc-pVXZ with X = D, T level of theory; harmonic and anharmonic terms are computed employing second-order perturbation theory (VPT2) after the full cubic and the semidiagonal part of the quartic force field treatments, which in turn generate all vibrational constants apart from those of the form ϕ_{ijkl} (Mills 1972b; Watson 1977; Papousek & Aliev 1982). Additionally, the so-called F12-TcCR quartic force field (QFF) is employed to provide VPT2 results via SPECTRO (Watrous et al. 2022; Fortenberry & Lee 2022). This composite energy is defined at each displaced point from the core-including CCSD(T)-F12/cc-pCVTZ-F12 optimised geometry; CCSD(T)-F12/cc-pCVTZ-F12 energies ('TcC') are computed and combined with CCSD(T)/cc-pVTZ-DK relativistic effects ('R'), a method known to produce accuracies on the order of 1.0 cm^{-1} compared to experiments (Watrous et al. 2022; Gardner et al. 2021). Subsequently, SPECTRO transforms the force constants from the QFF contributions to averaged and singly vibrationally excited principal rotational constants as well as the quartic and sextic centrifugal distortion constants (Inostroza et al. 2011, 2013).

For the specific case presented below, the rotational and distortion constants were obtained at CCSD(T)/cc-pXTZ level of theory only (with X = D, T). The CCSD(T)-F12-TcCR/cc-pCVTZ-F12 level was inferred using the scaling factors presented in Table B.1 in Appendix B.2. These scaling factors are obtained by computing the differences in rotational and distortion constants obtained at CCSD(T)-F12-TcCR/cc-pCVTZ-F12 and CCSD(T)/cc-pVTZ levels of theory for 10-HNCHCHO. These differences are applied to the constants obtained for 9-HNCHCHO at CCSD(T)/cc-pVTZ and comprise the effects given by the anharmonic corrections at the full QFF level and F12-TcCR contributions.

[2]For the current version of MOLPRO, see https://www.molpro.net.
[3]For the current version of CFOUR, see http://www.cfour.de.

4.3 Results and discussion

A successful laboratory or even interstellar gas phase detection of a molecule is a direct consequence of the precise characterisation of the rotational constants and the reaction kinetics involved. These, in turn, rely upon reference data of some variety. Typically, this is most readily provided by reliable quantum chemical computations as well as the identification of the lowest energy isomers of the molecular target (Puzzarini & Stanton 2023).

4.3.1 Isomers and relative energies

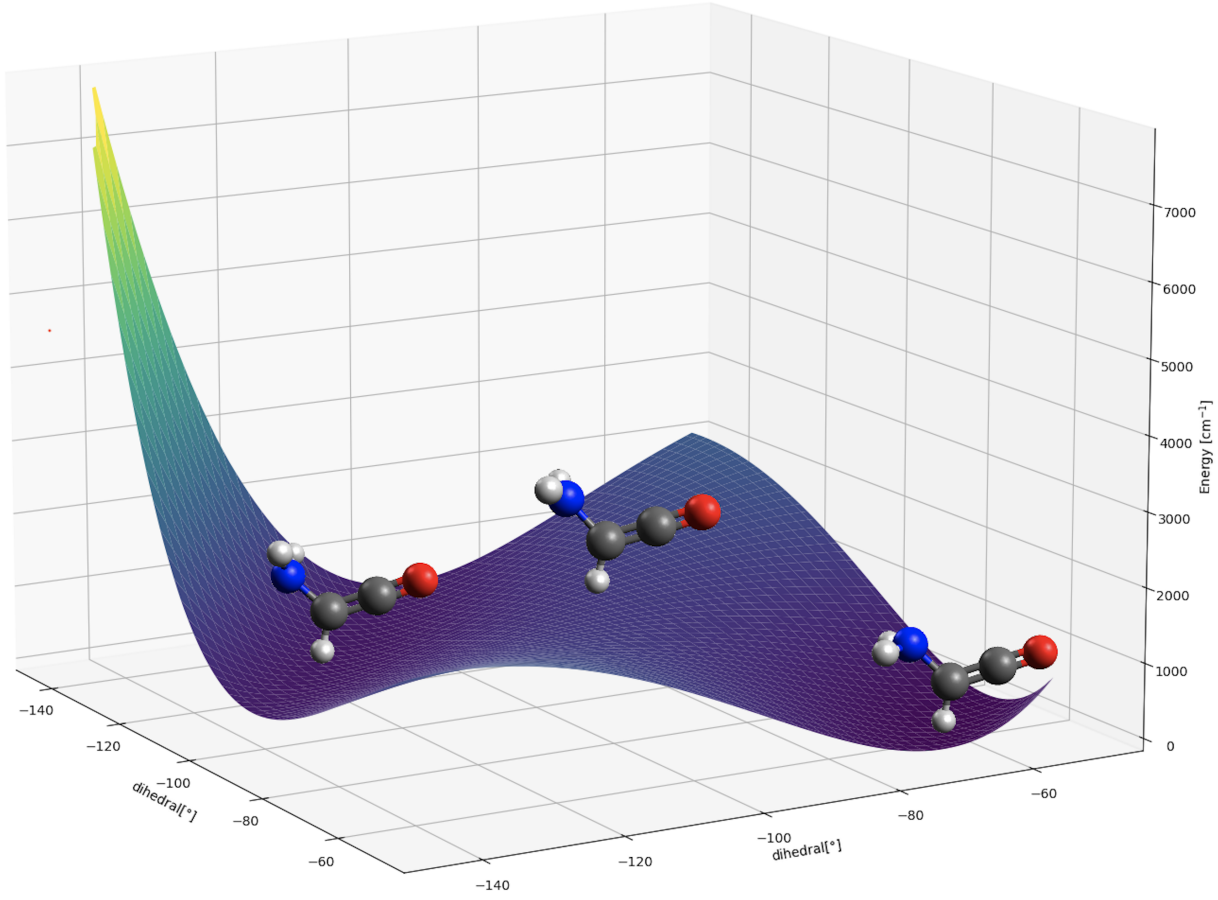

Figure 4.2: Potential energy surface scan of the NH_2CHCO conformer proposed by Krasnokutski (2021); Krasnokutski et al. (2022) at the CCSD(T)-F12/cc-pCVTZ-F12 level of theory. Resolution is of two degrees. Dihedral values refer to the angles lying between the hydrogen of the primary amine and the CN bond.

There is a trend seen in the COMs detected in the ISM in that they are the energetically most favoured isomers. However, it is important to note that kinetics can also play a significant role in determining the outcome of chemical reactions in the ISM, even when the most stable isomer is

not the kinetically most favoured product (e.g. CH_2CCO, Shingledecker et al. 2021; cis- formic acid HCOOH, Cuadrado et al. 2016; and trans- methyl formate CH_3OCHO, Neill et al. 2012). Consequently, it is possible to detect isomers with higher energies in the ISM, even if they are not

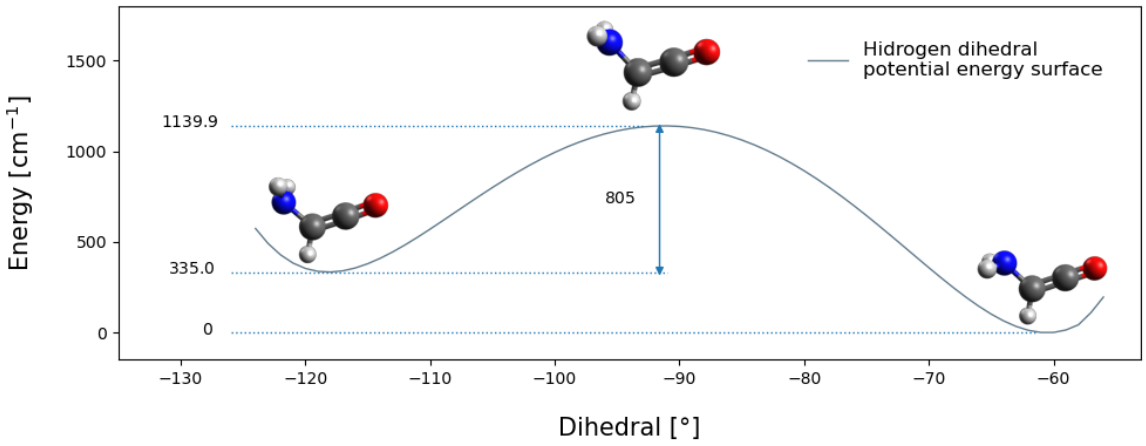

Figure 4.3: Energy profile of NH dihedral calculated at CCSD(T)-F12/cc-pCVTZ-F12 level of theory. The dihedral value refers to the angle lying between the hydrogen of the primary amine, and the CN bond. The second NH dihedral is kept constant with respect to the former.

the most stable isomers. In light of this, the isomer proposed by Krasnokutski (2021) and Krasnokutski et al. (2022) could be detected in the ISM, even though it is less energetically favoured than others. Nevertheless, understanding the EtA chemical network requires the detection of the relevant species that might be involved. Relative energies are an important consideration, but the molecular precursors and energetic environment will greatly inform the products that are formed regardless of the relative energies.

The first step in this work was to verify that the energy associated with the geometry of the NH_2CHCO conformer proposed by Krasnokutski et al. (2022) is indeed the energetic minimum of this chemical formula. After geometrical optimisation of this same isomer at the CCSD(T)-F12/cc-pCVTZ-F12 level of theory, a potential energy surface (PES) scan was performed to study an energy profile of the isomer as a function of the two HNH dihedral angles. Figure 4.2 reports the PES scan obtained through the scan at two-degree increments with CCSD(T)-F12/cc-pCVTZ-F12. The dihedral values refer to the angles lying between the hydrogen of the primary amine and the CN bond. Another isomer was determined to lie at a lower energy through this scan. This stability might be due to a more favourable steric arrangement of the amino hydrogens with respect to the nearby sp^2 carbon. Figure 4.3 shows the same analysis specifically along the coordinate for the equivalent hydrogens as the reflection of each other. The energy difference between these two conformers is clear at 335 cm^{-1}, and is equivalent to ~480 K. The two conformers are separated by an 805 cm^{-1} (~1150 K) energy barrier, constituting an impediment to free hydrogen movement.

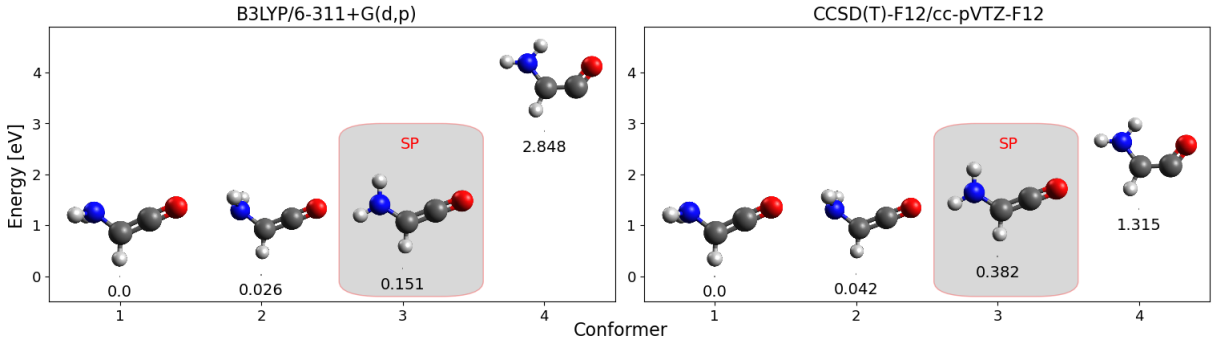

Figure 4.4: Comparison with the conformers proposed by Krasnokutski (2021). On the left, at B3LYP/6-311+G(d,p) level of calculation, and on the right at the CCSD(T)-F12/cc-pCVTZ-F12 level. These conformers are the product of the C + NH_3 + CO barrierless reaction. The SP connecting 2 and 3 NH_2CHCO conformers is reported in the grey box. For the isomer 4, the values were obtained employing UKS (spin-Unrestricted Kohn-Sham program) B3LYP/6-311+G(d,p) and UCCSD(T)-F12/cc-pCVTZ level of theory, for left and right plots, respectively.

Table 4.1: Energy of NH_2CHCO conformers herein found in respect to the work of Krasnokutski et al. 2021.

	Energy[a] [cm^{-1}]			Energy[a] [eV]		
	B3LYP	MP2	CCSD(T)-F12	B3LYP	MP2	CCSD(T)-F12
	6-311+G(d,p)		cc-pCVTZ-F12	6-311+G(d,p)		cc-pCVTZ-F12
1	0.0	0.0	0.0	0.000	0.000	0.000
2	212.7	687.1	334.8	0.026	0.085	0.042
3[b]	1220.0	3578.7	3078.1	0.151	0.444	0.382
4	22967.8[c]	-142014.7[d]	10604.8[e]	2.848[c]	-17.607[d]	1.315[e]

Notes. [a]The energies are normalised to that of the lowest energy isomer 1. [b]Saddle point connecting 2 and 3 NH_2CHCO conformers. [c,d,e]Values obtained employing UKS (spin-Unrestricted Kohn-Sham program) B3LYP/6-311+G(d,p), UPM2/6-311+G(d,p), and UCCSD(T)-F12/cc-pCVTZ level of theory, respectively. The difference in the significant digits existing between values in Hartree and eV is maintained to justify the Hartree-eV conversion factor (1 a.u = 27.2114 eV). We note that the CO+NH_3+C reaction lies approximately 1038, 1013, and 1060 eV above the 1-conformer for the three respective levels of theory.

While the studies mentioned earlier (Krasnokutski 2021; Krasnokutski et al. 2022) make use of two lower-level theoretical approaches, namely the B3LYP density functional theory (DFT) and MP2, both with the 6-311+G(d,p) Pople basis set, the present analysis of the isomers goes beyond this with coupled-cluster theory. In Table 4.1, the isomerisation energies obtained in this work are reported in cm^{-1} and eV. The results obtained at the same level of theory as the previous

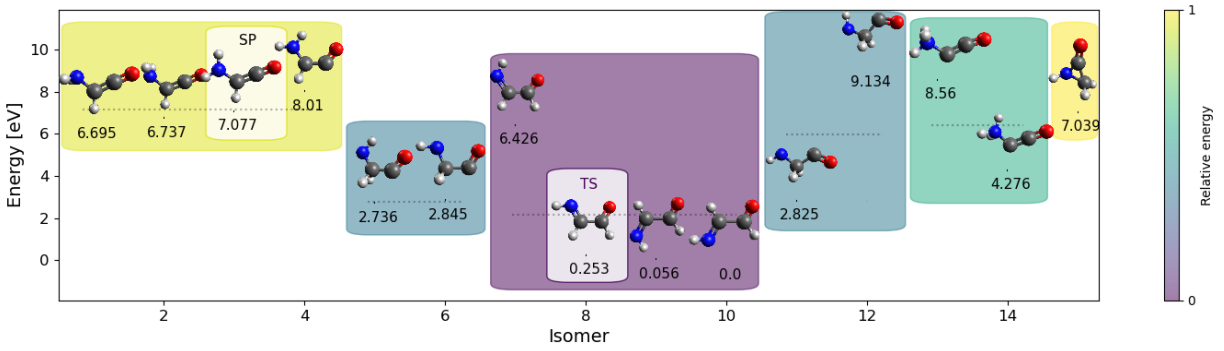

Figure 4.5: All new calculated conformers and isomers at CCSD(T)-F12/cc-pCVTZ-F12 level. Conformers of the same isomer are grouped in the same box. Each box is colour-coded according to the minimum energy of the relative conformer. From the most to the least favourable isomer, normalised colour scale ranges from violet to yellow, respectively. The SP and TS are both highlighted by lighter-coloured boxes. The average value of the isomer's conformers, which does not include TS and SP, and the values of each conformer are reported with a grey dotted line and a black solid line, respectively. The numerical value of the latter is also given.

studies are flanked by the present ones from CCSD(T)-F12/cc-pCVTZ-F12. Figure 4.4 shows a comparison between B3LYP/6-311+G(d,p) (previously used as reference in Krasnokutski (2021) and Krasnokutski et al. (2022)) and CCSD(T)-F12/cc-pCVTZ-F12 levels of theory. The isomers are named starting from the lowest energy in cardinal numbers: 1 and 2 are the lowest- and highest-energy NH_2CHCO conformers, respectively; 3 and 4 refer to the saddle point (SP) that connects the previous conformer to the next one and an additional conformer found to be higher in energy, respectively.

The higher-level CCSD(T)-F12 energy difference between conformer 1 and 2 is double the amount suggested by DFT. The gap between conformer 1 and SP 3 passes from 0.1513 eV (~1775 K) in B3LYP/6-311+G(d,p) to 0.3816 eV (~4428 K) in CCSD(T)-F12/cc-pCVTZ-F12; that is, it almost triples. Differences between 1 and 4 go from 2.8476 eV (~33046 K) to 1.3148 eV (~15258 K), reducing by roughly a factor of one-half when explicitly correlated coupled-cluster theory is utilised.

We conducted a wider PES isomer analysis in an attempt to understand whether the two NH_2CHCO conformers identified so far are effectively the most energetically favoured. For consistency, our analysis used the B3LYP/6-311+G(d,p), MP2/6-311+G(d,p), and CCSD(T)-F12/cc-pCVTZ-F12 levels of theory; the results are summarised in Table 4.2. The values are reported both in cm^{-1} and eV and are normalised with respect to the new energy minimum obtained at the highest level calculation. Figure 4.5 reports the isomerisation energies at the CCSD(T)-F12/cc-pCVTZ-F12 level of theory, which better constrain the energies of NH_2CHCO isomers and conformers (Adler et al. 2007; Rauhut et al. 2009; Knizia et al. 2009b). The molecules are grouped into distinct isomeric families. Within each of these, the analysed conformers are shown. The isomer families are colour-coded by taking the energy of the lowest-energy isomer

Table 4.2: Energy of all NH_2CHCO conformers and isomers.

	Energy[a] [cm^{-1}]			Energy[a] [eV]		
	B3LYP	MP2	CCSD(T)-F12	B3LYP	MP2	CCSD(T)-F12
	6-311+G(d,p)		cc-pCVTZ-F12	6-311+G(d,p)		cc-pCVTZ-F12
1	-20726.1	129305.2	54003.2	-2.567	16.032	6.695
2	-20513.4	129992.2	54338.0	-2.543	16.117	6.737
3[b]	-19506.0	132883.9	57081.3	-2.418	16.475	7.077
4	2241.8	-12709.6	64607.9	0.278	-1.576	8.010
5	1521.5	-15421.1	22066.0	0.189	-1.912	2.736
6	1610.0[c]	8336.7[d]	22944.2[e]	0.200[c]	1.034[d]	2.845[e]
7	802.3[c]	-14423.3[d]	51829.9[e]	0.099[c]	-1.788[d]	6.426[e]
8[f]	2069.6[c]	-13163.2[d]	2042.9[e]	0.257[c]	-1.632[d]	0.253[e]
9	581.0	-14524.0	450.8	0.072	-1.801	0.056
10	0.0	0.0	0.0	0.000	0.000	0.000
11	1471.5[c]	8276.0[d]	22782.5[e]	0.182[c]	1.026[d]	2.825[e]
12	2737.6	8034.2	73671.8	0.339	0.996	9.134
13	-5574.9	147548.4	69044.8	-0.691	18.293	8.560
14	17097.2	2722.2	34490.7	2.120	0.338	4.276
15	-19040.0	133322.8	56775.8	-2.361	16.530	7.039

Notes. [a]The energies are normalised to that of the lowest energy isomer, namely isomer 10. [b]Saddle point connecting 2 and 3 NH_2CHCO conformers. [c,d,e]Values obtained employing UKS (spin-Unrestricted Kohn-Sham program) B3LYP/6-311+G(d,p), UPM2/6-311+G(d,p), and UCCSD(T)-F12/cc-pCVTZ level of theory, respectively. [f]Transition state connecting 7 and 9 HNCHCHO conformers. The difference in the significant digits existing between values in Hartree [a.u.] and eV is maintained to justify the Hartree-eV conversion factor (1 a.u = 27.2114 eV). We note that the CO+NH_3+C reaction lies approximately 1036, 1029, and 1066 eV above the 10-isomer, for the three respective levels of theory.

as a reference, giving a total of six distinct isomers. Saddle points and transition states (TSs) are marked with lighter coloured boxes. This results in six distinct groups with colours ranging from yellow to violet for the highest to the lowest energies, respectively.

In Table 4.2, all of the isomers and conformers are normalised to the new minimum obtained at CCSD(T)-F12/cc-pCVTZ-F12 level of theory. The grey dotted line refers to the average value of the energy of the conformers in the relative coloured box [4], while the black solid line shows the energy value of the conformers themselves.

The names assigned to the additional isomers do not take into account the ascending order of

[4]SPs and TSs are not considered.

Table 4.3: Theoretical frequencies associated with the vibration modes of 1- and 10-HNCHCHO isomers.

	1-NH_2CHCO		10-HNCHCHO	
ZPT[a] [cm^{-1}]	10920.7		10886.3	
Mode	Harmonic [cm^{-1}]	Anharmonic[b] [cm^{-1}]	Harmonic [cm^{-1}]	Anharmonic[b] [cm^{-1}]
1	3611.4	3435.8	3474.9	3304.8
2	3530.4	3374.7	3096.8	2939.6
3	3171.4	3036.0	2990.9	2837.7
4	2192.3	2143.4	1773.6	1747.8
5	1671.2	1622.0	1672.5	1638.7
6	1437.7	1402.3	1405.0	1371.4
7	1224.1	1188.5	1369.2	1339.3
8	1182.0	1154.4	1228.9	1205.4
9	1033.8	1006.7	1119.9	1134.7
10	821.2	748.2	1040.5	1017.1
11	656.4	641.3	1033.5	1029.2
12	599.0	582.3	701.2	692.9
13	531.5	537.9	582.6	579.9
14	254.9	249.8	342.2	351.6
15	218.2	216.9	149.9	178.8

Notes. Frequencies are obtained at the CCSD(T)-F12-TcCR/cc-pCVTZ-F12 level of theory. [a]ZPT stands for zero point energy. [b]Anharmonic frequencies take into account Fermi-resonance corrections.

energy but instead refer to the order in which they were included in the analysis. The conformers calculated above were the least energetically favourable after the cyclic isomer. The iminic isomer (violet box) is the lowest-energy isomer, making it a primary target for spectroscopic exploration.

In contrast to two previous studies (Redondo et al. 2018; Drabkin et al. 2023), we identified three different minima for this iminoacetaldehyde, that in turn can be recognised as a tautomer of aminoketene. Excluding the highest-energy 7-HNCHCHO and the TS (considered a minimum in Redondo et al. (2018)), conformers 9- and 10-HNCHCHO lie fairly close in energy. The latter is the lowest-energy form of this molecular class but is only 0.056 eV (~650 K) lower than 9-HNCHCHO, which differs only in the spatial arrangement of the imine hydrogen. This difference was estimated to be of 1.12 eV (~13000 K) at CCSD(T)/aug-cc-pVQZ//CCSD/cc-pVTZ level of theory in Redondo et al. (2018). 7-HNCHCHO and 8-HNCHCHO (TS), in turn, are analogues of

Table 4.4: Theoretical spectroscopic constants determined for 1- and 10-HNCHCHO isomers.

	1-NH_2CHCO			10-HNCHCHO		
Rotational constants	CCSD(T)[a] cc-pVDZ	CCSD(T)[a] cc-pVTZ	F12-TcCR[b]	CCSD(T[a]) cc-pVDZ	CCSD(T[a]) cc-pVTZ	F12-TcCR[b]
A_0 /MHz	42829.8	43900.3	44201.2	51798.0	52843.6	53096.0
B_0 /MHz	4531.0	4592.4	4637.1	4638.9	4703.9	4749.0
C_0 /MHz	4183.2	4245.2	4286.8	4257.6	4319.7	4359.8
Δ_J /kHz	2.559	2.628	2.657	0.987	1.024	1.041
Δ_K /MHz	2.569	2.797	2.801	0.415	0.433	0.433
Δ_{JK} /kHz	-113.571	-120.140	0.0	-7.277	-7.174	0.0
δ_J /Hz	523.470	536.605	542.934	103.669	106.096	108.204
δ_K /kHz	13.238	12.821	11.969	5.111	5.300	5.401
Φ_J /mHz	9.280	10.057	10.156	0.196	0.200	0.204
Φ_{JK} /mHz	-95.168	-132.722	-136.102	-2.074	-2.376	-2.355
Φ_{KJ} /Hz	-14.904	-15.973	-15.961	-0.546	-0.563	-0.565
Φ_K /Hz	464.261	529.158	527.549	8.553	9.209	9.292
ϕ_J /mHz	3.228	3.484	3.519	0.072	0.074	0.076
ϕ_{JK} /mHz	152.277	173.907	184.522	2.942	2.963	2.978
ϕ_K /Hz	21.900	23.634	22.920	0.793	0.828	0.833

Notes. Geometries initially optimised at CCSD(T)-F12/cc-pCVTZ-F12 level of theory for the energy calculation were then optimised at the relative basis set. [a]Harmonic and anharmonic terms are computed employing VPT2 after full cubic and semidiagonal contribution estimations. [b]Harmonic and anharmonic corrections were calculated from VPT2 via the F12-TcCR QFF.

the 9 and 10 conformers, the difference being that they have the iminic nitrogen on the same side as the aldehyde group. The TS is 0.253 eV (∼2936 K) above, while 7-HNCHCHO lies higher in energy (6.426 eV, or ∼ 74500K).

Isomers 13 and 14, which are enclosed in the green box, are at a higher energy level than the global minimum. Because the N atom is formally positively charged and the adjacent C atom is negatively charged, the system can be stabilised by proton transfer to produce aminoketene as well (Krasnokutski et al. 2022). Thus, the proton transfer can occur from the NH_3-group present in isomer 13 to the adjacent negative carbon to lead to the formation of isomer 1 by an exothermic process (-1.8 eV). On the other hand, in the case of isomer 14, the proton transfer is from the NH_3-group of isomer 14 to the carbon to form isomer 1. This is an endothermic process with an energy barrier of about 2.4 eV. In the previous studies (Redondo et al. 2018; Drabkin et al. 2023), the energies obtained at CCSD(T)/aug-cc-pVQZ//CCSD/cc-pVTZ level for

Table 4.5: Vibrationally averaged dipole moments of 1-NH_2CHCO, 9- and 10-HNCHCHO isomers.

		Isomer		
Parameter	Unit	1-	9-	10-
R_5	kHz	6.64	-0.71	-0.58
R_6	Hz	-0.29	-4.62	-4.05
μ_a	D	2.04	0.51	1.94
μ_b	D	1.26	1.29	0.98
μ_c	D	0.0	0.0	0.0
κ^a		-0.98	-0.98	-0.98

Notes. $^a\kappa$ is the asymmetric rotor parameter given by $(2B - A - C)/(A - C)$ (Gordy & Cook 1984). μ_x is the dipole moment with respect to the x inertia axis.

the imine isomers are comparable with those obtained in this study at the B3LYP/6-311+G(d,p) level. In the former case, isomers 9, 8, and 7 have energies normalised to isomer 10 of 0.052 eV, 0.239 eV, and 0.085 eV, respectively. In the latter case, values are of 0.072 eV, 0.257 eV, and 0.099 eV for isomers 9, 8, and 7, respectively (Table 4.2). Interestingly, the energy value of isomer 7 differs substantially from the trends mentioned above, resulting in it lying much higher in energy than the other imines when the CCSD(T)-F12 method is employed. This difference has to be ascribed to the theoretical F12 treatment, whereby explicitly correlated effects are taken into account. This method includes the electron–electron interaction at all distances, rather than approximating it at long distances, allowing for improvement of the accuracy, especially for large molecules. Table 4.2 shows how the F12 treatment effects not only isomer 7 but also many others. This energy difference in isomer 7 is comparable to that found between the 10-HNCHCHO and 1-NH_2CHCO isomers at the B3LYP/6-311+G(d,p) level, namely of 6.695 eV. For a comparison with the level of theory employed in the previous studies, Figure B.1 in Appendix B.1 shows the drastic difference in energy that these same isomers exhibit with B3LYP/6-311+G(d,p).

4.3.2 Spectroscopic data

For interstellar identification purposes of this molecule, conformers 10-HNCHCHO and 9-HNCHCHO should be regarded as natural candidates for observations. This is in line with what Redondo et al. (2018) suggested, but these authors report rotational and distortion constants at CCSD/cc-pVTZ level of theory. This same idea is supported by the recent work of Drabkin et al. (2023), in which the authors were able to characterise the IR and UV-VIS spectrum of 10-HNCHCHO and 9-HNCHCHO employing a deposition of 2-azidoacetaldehyde as a precursor on a large excess of argon onto the cold matrix window. In order to be able to detect these molecules in molecular clouds, the next step would then be the characterisation of such molecules in the gas phase. In the present work, we provide state-of-the-art quantum chemical calculations in order to better

Table 4.6: Theoretical spectroscopic constants determined for 9-HNCHCHO isomer.

	9-HNCHCHO		
Rotational constants	CCSD(T)[a] cc-pVDZ	CCSD(T)[a] cc-pVTZ	F12-TcCR[b]
A_0 /MHz	49363.3	50035.8	50288.2
B_0 /MHz	4628.3	4707.1	4752.3
C_0 /MHz	4231.8	4303.2	4343.2
Δ_J /kHz	1.043	1.088	1.105
Δ_K /MHz	0.361	0.372	0.372
Δ_{JK} /kHz	-6.978	-6.800	-6.800
δ_J /Hz	114.123	118.658	120.766
δ_K /kHz	5.354	5.629	5.730
Φ_J /mHz	0.192	0.177	0.181
Φ_{JK} /mHz	1.160	2.524	2.503
Φ_{KJ} /Hz	-0.623	-0.681	-0.683
Φ_K /Hz	7.346	7.784	7.867
ϕ_J /mHz	0.076	0.075	0.077
ϕ_{JK} /mHz	3.525	3.644	3.658
ϕ_K /Hz	0.808	0.857	0.861

Notes. Geometries initially optimised at CCSD(T)-F12/cc-pCVTZ-F12 level of theory for the energy calculation were then optimised at the relative basis set. [a]Harmonic and anharmonic terms are computed employing VPT2 after full cubic and semidiagonal contribution estimations. [b]Harmonic and anharmonic corrections were calculated from VPT2 via the F12-TcCR QFF.

constrain the rotational and distortion constants of these promising candidates.

Both of the isomers are closed-shell molecules, easing the computational rotational analysis propaedeutic to the experimental characterisation of the rotational constants. The same cannot be said of isomers 5 and 6 as these are open-shell structures. Starting from the optimised geometry obtained at the CCSD(T)-F12/cc-pCVTZ-F12 level of theory, we computed the F12-TcCR QFF for isomers 1 and 10. Fundamental harmonic frequencies and Fermi-resonance corrected frequencies are reported in Table 4.3. Zero-point energy values are also provided.

We obtained sets of rotational and distortion constants at CCSD(T)/cc-pVXZ (X = D, T) and F12-TcCR levels of theory. Rotational and distortion constants of these two isomers are reported in Table 4.4 using the Watson A-reduced Hamiltonian. The choice of this Hamiltonian was based on parameters R_5 and R_6 reported in Table 4.5. The latter are used to determine the free parameters $s_{111}(S)$ and $s_{111}(A)$, whose formulae are given in the equations 4.1 and 4.2,

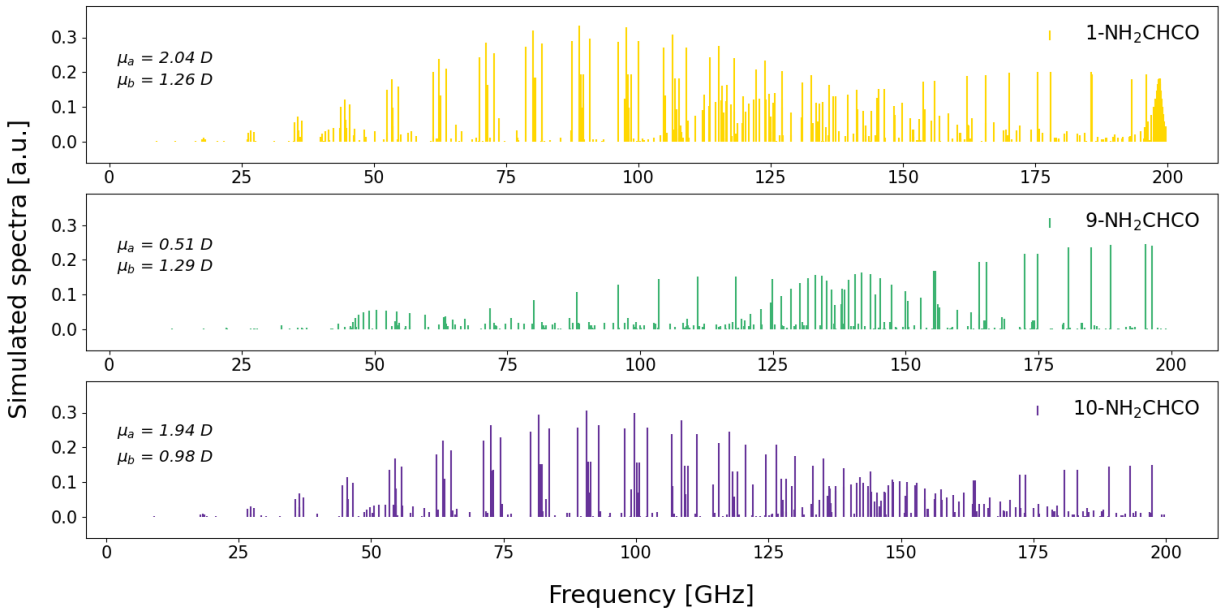

Figure 4.6: Simulated spectra at 15K of 1-, 9-, and 10-HNCHCHO employing the rotational constants presented in Tables 4.4 and 4.6. Theoretical spectra are produced using the highest level of calculation for each isomer, namely CCSD(T)-F12-TcCR QFF for 10- and 1-NH_2CHCO and the scaled CCSD(T)-F12-TcCR QFF for 9-HNCHCHO (for which more details are provided in Table B.1 of Appendix B.2).

respectively. B_z, B_x and B_y, in turn, correspond to the rotational constants A_0, B_0, and C_0.

$$s_{111}(S) = \frac{2R_5}{2B_z - B_x - B_y}, \tag{4.1}$$

$$s_{111}(A) = -\frac{4R_6}{B_x - B_y}. \tag{4.2}$$

The free parameter s_{111} takes part in the unitary transformation of the Hamiltonian, and as suggested by Watson (1978b), its value should be as low as possible. Historically, the S and A reductions were conceived to approach near-symmetric prolate or oblate rotors ($\kappa = -1/+1$) and asymmetric rotors ($\kappa = 0$), respectively. However, the increase in computational power in recent decades and the minimal differences found here in the s_{111} values mean that it is not strictly necessary to adopt one reduction over the other. For these reasons, as the values of $s_{111}(A)$ and $s_{111}(S)$ are both of the order of 10^{-7} or less, we adopted the Watson A-reduced Hamiltonian.

For isomer 9, the rotational and distortion constants are reported in Table 4.6, making use of the scaling factors presented in Table B.1 in Appendix B.2. This strategy was adopted in order to overcome the low isomerisation barrier existing between isomers 9 and 10, which might have prevented a VPT2 analysis.

The different geometrical configuration of the isomers analysed in this section is clear when comparing the rotational constants. Taking the highest level of theory as a reference, 10- and

9-HNCHCHO have similar A_0, B_0, and C_0 rotational constants from which 1-NH_2CHCO clearly deviates. Figure 4.6 shows the synthetic spectra obtained by computing the rotational and distortion constants at 15K, an excitation temperature (T_{ex}) found for most of the molecules in the G+0.693 molecular cloud (see e.g. Zeng et al. (2018)). At 15K, the Planck function peaks at around 90 GHz for 10-HNCHCHO and 1-NH_2CHCO, and at around 200 GHz for 9-HNCHCHO. The values of the dipole moments are μ_a = 2.04 D, 0.51 D, and 1.94 D and μ_b = 1.26 D, 1.29 D, and 1.29 D for 1-NH_2CHCO and 9- and 10-HNCHCHO, respectively. These values are provided in Table 4.5. As a consequence, the spectra of 10-HNCHCHO and 1-NH_2CHCO are dominated by *a*-type transitions, and that of 9-HNCHCHO is dominated by *b*-types.

The fundamental *a*-type transition $J_{K_a,K_c} = 1_{0,1} - 0_{0,0}$ is given by the sum of the two rotational constants B_0 and C_0. For assignment purposes, 1-NH_2CHCO and 10-HNCHCHO have fundamental frequencies at 9.108 GHz and 8.923 GHz, respectively. In the case of 9-HNCHCHO , the *b*-type fundamental rotational transition $J_{K_a,K_c} = 1_{1,1} - 0_{0,0}$ is instead given by the sum of A_0 and C_0 and falls at 4.594 GHz. In this case, all the isomers are prolate molecules, implying that the biggest rotational constant is A_0. As a result, the uncertainty over the *a*-type fundamental transitions will be significantly reduced compared to the *b*-type fundamental transition. Compared to previous studies (Redondo et al. 2018; Drabkin et al. 2023), the higher level of theory employed here includes the additional corrections of core electron correlation, explicit correlation along with its faster basis set convergence, scalar relativity, and the Coriolis resonances in addition to Fermi resonance polyads, and provides a whole set of new sextic distortion constants.

From a laboratory point of view, product formation being equal, 10-HNCHCHO remains the most promising isomer; not only because it is the most energetically favoured, but also because it should exhibit the most intense transitions. It therefore serves as the best observational target for this isomer family. Albeit to a lesser extent, isomer 9 remains a valid alternative, even if it presents critical problems. While it exhibits the second-most energetically favoured structure, it does not present lines as intense as those of 10-HNCHCHO at low frequencies (please refer to Figure 4.6). Instead, isomer 1, although exhibiting the strongest transitions, is only the ninth of the isomers analysed in this work in order of energy, making searches for it in space more complicated and its detection less straightforward.

4.4 Conclusions

Synthetic spectra computed employing very high-level ab initio calculation support the idea that 10-HNCHCHO is the most promising candidate for ISM observations among the molecules investigated here. 10-HNCHCHO is one of the isomers of NH_2CHCO currently thought to be a crucial step in the formation route leading to EtA, a prebiotic molecule recently detected in space (Rivilla et al. 2021c)). The chemical pathway leading to its formation is shown in Figure 4.1. 10-HNCHCHO might help to elucidate not only the chemical network involving EtA, but also other chemical routes of astrochemical relevance, broadening our understanding of the chemistry and physics of the ISM.

In this paper, expanding on the contributions of previous work (Krasnokutski 2021; Krasnokutski et al. 2022), we extended the study of NH_2CHCO to its different isomeric forms.

The isomer previously thought to be the lowest in energy and experimentally observed in a condensed-phase matrix (Krasnokutski 2021; Krasnokutski et al. 2022) is actually only the ninth most energetic out of 15 structural and conformational isomers that might be present in the gas-phase within the ISM. Of these 15 isomers, 13 were studied in this work; one is found to be a SP and another a TS, respectively. In contrast to previously reported findings, the most energetically favourable isomer of NH_2CHCO is not in the amine but rather the imine form HNCHCHO.

In contrast to what was observed by Redondo et al. (2018) and Drabkin et al. (2023), the latter includes three minima, two of which in particular exhibit the lowest isomer or conformational energies. The rotational and distortion constants of the two lowest-energy isomers 9-HNCHCHO and 10-HNCHCHO, correctly identified as such in the previous studies (Redondo et al. 2018; Drabkin et al. 2023), were herein obtained at a higher level of theory, taking into account core electron correlation, explicit correlation along with its faster basis set convergence, scalar relativity, and VPT2 resonances. These new results should help to guide the community towards spectroscopic analysis of and observational searches for the above-mentioned species, allowing us to determine whether or not and in what quantities these molecules might take part in the processes that ultimately lead to the emergence of life.

Chapter 5

Summary and future perspectives

5.1 Conclusions

During my PhD I have studied the ground-state rotational spectrum of allylimine ($CH_2CHCHNH$) and of 3-amino-2-propenitrile (APN, $H_2NCHCHCN$), two potential prebiotic precursors involved in the formation of amino acids in space. Their search in the G+0.693-0.027 molecular cloud led to the tentative assignment of several transitions of the former, allowing to its estimation of column density and relative isotopic abundances, and to the the identification of blended transitions of the latter, making it possible to estimate its upper limit abundance. The final study involved state-of-the-art quantum chemical calculations to study the energy of NH_2CHCO isomers, and to characterise the rotational and distortion constants of the most energetically favourable ones to assist their search in laboratory and consequently in space.

In chapter 2, supported by high-level theoretical calculations, we have studied the rotational spectra of the two isomers *Ta* and *Ts*-allyllimine, $CH_2CHCHNH$, from 84 to 300 GHz. About 617 and 470 new rotational transitions, some of which also presenting resolved hyperfine structural features due to the ^{14}N nucleus, allowed to obtain a set of very precise rotational constants, including a complete set of quartic and some sextic centrifugal distortion coefficients, and hyperfine splitting constants. The new catalogues of highly accurate rest frequencies were used to perform a spectral survey of the *Ta* and *Ts* allylimine isomers of the G+0.693 molecular cloud. Eight transitions have been tentatively assigned to each isomer, leading to the derivation of column densities $N = (1.5 \pm 0.6) \times 10^{13}$ cm^{-2} for *Ta* and $N \sim 0.5 \times 10^{13}$ cm^{-2} for *Ts*, resulting in an $[Ta]/[Ts]$ isomer ratio of ~ 3. These value, five times lower than the thermodynamic expected one, was found to be lower than those of the simpler related species cyanomethanimine and propargylimine, confirming the trend of decreasing abundance with increasing molecule size.

In chapter 3, we characterised the high-resolution ground rotational spectrum of the lowest-energy conformer *Z* of aminoacrylonitrile (3-amino-2-propenitrile, $H_2NCHCHCN$), from 80 GHz up to 1 THz. While the Doppler regime was sufficient to resolve most of the recorded lines, sub-Doppler measurements were used to resolve the blended components, increasing the number of lines analysed to produce an even more precise rest frequency catalogue. The latter was then used to perform a spectral survey of the G+0.693 molecular cloud, which, assuming LTE

conditions, allowed us to estimate an upper limit for its column density of $N < 6.6\times10^{12}$ cm^{-2}. Compared to smaller cyanides such as vinyl cyanide (C_2H_3CN) and ethyl cyanide (C_2H_5CN), *Z*-APN resulted to be 14 and 6 times lower in relative abundance, respectively; for amines, on the other hand, vinylamine ($C_2H_3NH_2$) and ethylamine ($C_2H_5NH_2$) were more abundant by factors of 7 and 4, respectively. This indicates that the increase in molecular complexity, involving additional carbon and nitrogen atoms, leads to a decrease in molecular abundance of at least one order of magnitude.

In chapter 4 we extended the very high level ab initio calculations employed to investigate 15 structural and conformational isomers of NH_2CHCO, a potentially key precursor of ethanolamine ($NH_2CH_2CH_2OH$), a prebiotic precursor recently detected in G+0.693-0.027 molecular cloud. We found that the most energetically favoured isomer is not in the amine but rather in the iminic form, suggesting that the chemistry leading to its formation may follow an alternative chemical route and indicating the potentially most promising candidate to be sought in the gas phase. We then calculated the rotational and distortion constants of the two lowest energy isomers, 9-HNCHCHO and 10-HNCHCHO, at the state-of-the-art level of theory, providing new results that should support experimental spectroscopic analysis propaedeutic to future observational searches of these molecules, thus furthering our knowledge of the processes leading to the origin of life.

5.2 Future perspectives

We have seen how the detection of different isomers of the same molecule allows us to study the relative isomeric abundances. The detection of the two most energetically favourable allylimine isomers lays the groundwork for attempting to extend this study to the two highest energy isomers, *Ca* and *Cs*. This would further enhance our understanding of allylimine chemistry by allowing us to verify non-equilibrium processes that might favour less energetically favourable isomers in G+0.693 molecular cloud, as in the case of CH_2CCO Shingledecker et al. (2021), cis-formic acid HCOOH Cuadrado et al. (2016) and trans-methyl formate CH_3OCHO Neill et al. (2012) in other sources. A similar argument can also be made for APN, whose spectroscopic characterisation of the *E*-isomer could, in the presence of further observational data, allow its abundance to be compared with that of the *Z*-isomer.

We have seen that astrochemistry is actually a discipline that combines several branches of knowledge, from physics to chemistry, and may one day include biology in a more systematic way. As with all frontier sciences, the difficulty of combining different approaches may take time and dedication, but the prospects remain bright. The increase in the number of molecules detected so far is just another indication of the richness and complexity of the interstellar medium. The main theme of this thesis has been the search for precursors of prebiotic molecules that led to the emergence of life, but in some respects the latter is merely the manifestation of a non-negligible statistical event, as can be said of the chemical complexity of the ISM (as suggested by García-Sánchez et al. 2022).

In order to find answers one has to imagine scenarios, and in order to understand them one has to make assumptions, thus leaving out elements that may instead be decisive. The number of

molecules detected in space will only increase, as Figure 1.4 seems to tell us already, expanding the statistics at our disposal. With this it will be possible to identify trends that will seem obvious to us, but are currently still too hidden to be seen, providing as many answers as new questions. Personally, one of the biggest open questions is how chirality, an element that goes hand in hand with life itself, came about. McGuire et al. 2016 already showed us, detecting propylene oxide (CH_3CHCH_2O), that hints might also come from space. Of the twenty amino acids that make up our bodies, only the levorotatory form exists, but the dextrorotatory form is anything but rare in chemistry. Why did DNA specialise in encoding only 22 of the 500 naturally occurring amino acids? What was the reason for the emergence of the L form in biological systems? And why do we find the right-handed form in biological sugars instead? The development of new technologies, limiting ourselves to the field of astrophysics, will lead to much more powerful facilities such as the Extremely Large Telescope (ELT), or the implementation of ALMA itself, continuing to increase our level of knowledge. Think of the JWST for example: in little more than two years, it is revolutionising our view of the cosmos and, consequently, our role in it. Perhaps one day we will be able to find some exoplanets bio-signatures, to scientifically prove that Giordano Bruno was right.

It will be the constant synergy and dialogue between the various disciplines to allow us to make the leap that no single discipline can make: dialogue and listening before prophesying. Surface chemistry, for example, is leading to a rethink of how organic molecules detected in space are formed. In the '70s it was thought that reactions took place in the gas-phase, but we now know that most of COMs and prebiotic molecules are formed on solid surfaces of ices and dusts, which make up only 1% of the total ISM mass. Or the recent introduction of Graphics Processing Units (GPUs), which are taking computing power to unprecedented levels, allowing artificial intelligence to develop so rapidly that today's virtual assistants leave us even more room for creativity. As long as curiosity remains free, the prospects remain bright.

Appendix A

Complementary Material for Chapter 3

A.1 Computational details

Table A.1: Harmonic vibrational frequencies.

Mode	Symm.	*Ta*	*Ts*	Mode	Symm.	*Ta*	*Ts*
ν_1	A'	3486.3	3436.9	ν_6	A'	1702.4	1697.9
ν_2	A'	3250.8	3252.2	ν_7	A'	1643.8	1640.3
ν_3	A'	3193.1	3165.6	ν_8	A'	1455.8	1454.6
ν_4	A'	3154.6	3154.2	ν_9	A'	1401.3	1409.6
ν_5	A'	3052.3	3108.4	ν_{10}	A'	1304.4	1312.3

As mentioned in the main text, equilibrium geometries (and the corresponding energies) were evaluated using the CCSD(T)/CBS+CV composite scheme. The extrapolation to the CBS limit was performed considering Hartree-Fock Self Consistent Field (HF-SCF) and CCSD(T) correlation energy separately. For HF-SCF, the three-point exponential extrapolation formula by Feller (1992) was used in conjunction with the cc-pVnZ basis sets, with n=T,Q,5. For CCSD(T), the n^{-3} formula by Helgaker et al. (1997) and the cc-pVTZ and cc-pVQZ basis sets were employed. The CV contribution was computed as the difference between the all-electron (ae) computation and the corresponding frozen-core (fc) computation at the CCSD(T)/cc-pCVTZ level (Woon & Dunning 1995). Equilibrium geometries straightforwardly provided equilibrium rotational constants that were corrected for vibrational effects. The corresponding corrections were determined within vibrational perturbation theory to second order (VPT2) (Mills 1972a) and required anharmonic force field calculations, which were performed at the fc-CCSD(T)/cc-pVTZ level. These computations also provided, as a by-product, sextic centrifugal distortion constants. The CCSD(T)/CBS+CV composite scheme has also been employed for harmonic force field calculations, which led to the determination of the harmonic vibrational frequencies collected in Table A.1 and, as a by-product, the quartic centrifugal distortion constants. Nuclear quadrupole

coupling constants were computed at the CCSD(T)/cc-pCVQZ level correlating all electrons because, as is well known from the literature (Puzzarini et al. 2010), they require a basis set of at least quadruple-zeta quality and the correlation of core electrons. Furthermore, for quantitative predictions, vibrational corrections need to be incorporated (Puzzarini et al. 2009), that were evaluated using second-order Møller-Plesset perturbation theory (MP2; Møller & Plesset 1934) in conjunction with the cc-pCVTZ basis set. The CFOUR quantum chemistry package (Matthews et al. 2020) was employed for all CCSD(T) calculations, while the Gaussian16 software (Frisch et al. 2016) was used for MP2 computations. Sextic centrifugal distortion constants were obtained with an in-house program (Pietropolli Charmet & Cornaton 2018).

Appendix B

Complementary Material for Chapter 4

B.1 B3LYP/6-311+G(d,p) energy diagram

To have a direct comparison with Figure 4.5, in Figure B.1 we provide the results obtained at the B3LYP level of theory. We note how at this level of calculation the energy order of the isomer families is completely reversed. Amines are found to be the most energetically favoured, while in turn imines are considerably high in energy.

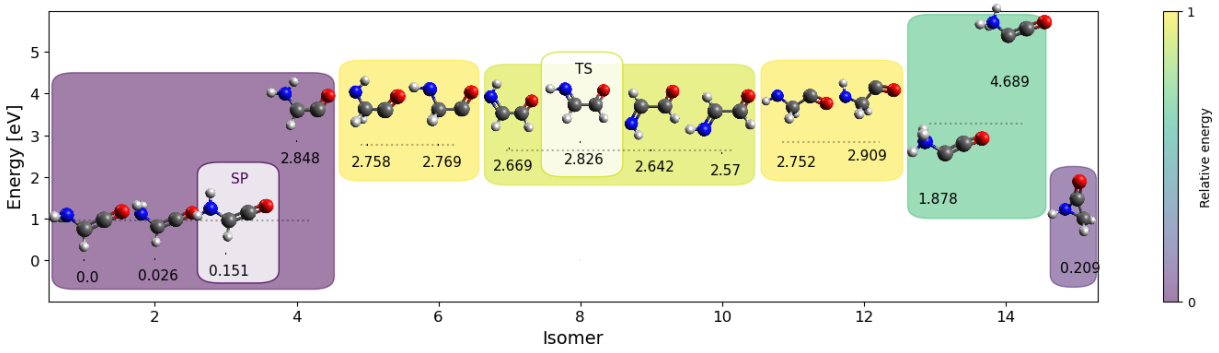

Figure B.1: All new calculated conformers and isomers at B3LYP/6-311+G(d,p) level, normalised to the 1-NH_2CHCO minimum. Conformers of the same isomer are grouped in the same box. Each box is colour-coded according to the minimum energy of the relative conformer. From the most to the least favourable isomer, normalised colour scale ranges from violet to yellow, respectively. SP (saddle point) and TS (transition state) are both highlighted by lighter-coloured boxes. The average value of the isomer's conformers, which does not include TS and SP, and the values of each conformer are reported with the grey dotted line and the black solid line, respectively. The numerical value of the latter is also given.

B.2 Details of the theoretical calculations

Table B.1: Theoretical scaling factors obtained from 1- and 10-HNCHCHO isomers

	Diff. relative to NH_2CHCO isomers	
Rotational constants	Δ^a 1-NH_2CHCO	10-HNCHCHO
A_0 /MHz	300.9	252.4
B_0 /MHz	44.7	45.1
C_0 /MHz	41.6	40.0
Δ_J /kHz	0.029	0.017
Δ_K /MHz	0.004	-0.000
Δ_{JK} /kHz	0.0[b]	0.0[b]
δ_J /Hz	6.329	2.108
δ_K /kHz	-0.852	0.101
Φ_J /mHz	0.099	0.004
Φ_{JK} /mHz	3.380	-0.021
Φ_{KJ} /Hz	-0.012	-0.002
Φ_K /Hz	-1.609	0.083
ϕ_J /mHz	0.035	0.002
ϕ_{JK} /mHz	10.614	0.015
ϕ_K /Hz	-0.714	0.005

Notes. The scaling factors were obtained by computing the difference between the constants calculated at CCSD(T)-F12/cc-pCVTZ-F12 QFF F12-TcCR level of theory and those calculated at CCSD(T)/cc-pVTZ VPT2 level of theory. Values are given for the isomer 1- and 10-HNCHCHO. [a]Δ refers to the difference found for the constant concerned between CCSD(T)-F12-TcCR/cc-pCVTZ-F12 and CCSD(T)/cc-pVTZ level of theories. [b]For Δ_{JK} differences, values were not considered due to the values obtained for both isomers in table 4.4.

We obtained the rotational and distortion constants of 9-HNCHCHO using two approaches. The first comprises the CCSD(T)/cc-pVXZ level of theory, with X = D and T, for which harmonics and anharmonics terms were calculated employing the second-order perturbation theory (VPT2) after the full cubic and the semidiagonal part of the quartic force field treatments, that in turn generate all vibrational constants except those in the form ϕ_{ijkl} (Mills 1972b; Watson 1977; Papousek & Aliev 1982). The second involved the use of a scaling factor obtained from the differences in the values of the CCSD(T)-F12-TcCR/cc-pCVTZ-F12 and CCSD(T)/cc-pVTZ

level of theory constants for 10-HNCHCHO, to be applied at constants obtained at the highest 9-HNCHCHO level of theory. These scaling factors comprise the effects given by the anharmonic corrections at the full quartic force field (QFF) level, taking into account F12-Triples Consistent Correlation analysis, core electron Correlation (cC), and relativistic effect (R) contributions (F12-TcCR contributions). Also, VPT2 stands for Vibrational Perturbation Theory to second order force fields (VPT2). Scaling factors obtained from Isomer 1 were not employed because of its geometrically dissimilarity in comparison with isomer 10, which in turn is the closest conformer. Table B.1 reports the scaling factors obtained from 1- and 10-HNCHCHO, and the rotational and distortion constants obtained for 9-HNCHCHO.

Bibliography

Adler, T. B., Knizia, G., & Werner, H.-J. 2007, J. Chem. Phys., 127, 221106

Agúndez, M., Cabezas, C., Tercero, B., et al. 2021, A&A, 647, L10

Alberton, D., Bizzocchi, L., Jiang, N., et al. 2023, A&A, 669, A93

ALMA. 2021, ALMA, https://www.almaobservatory.org/en/about-alma/how-alma-works/how-does-alma-see/

Altwegg, K., Balsiger, H., Bar-Nun, A., et al. 2016a, Science Advances, 2, e1600285

Altwegg, K., Balsiger, H., Bar-Nun, A., et al. 2016b, Science Advances, 2, e1600285

Anderson, L. D., Bania, T. M., Jackson, J. M., et al. 2009, ApJS, 181, 255

Andersson, M. P. & Uvdal, P. 2005, Journal of Physical Chemistry A, 109, 2937

Andre, P., Ward-Thompson, D., & Barsony, M. 1993, ApJ, 406, 122

Aponte, J. C., Elsila, J. E., Glavin, D. P., et al. 2017, ACS Earth and Space Chemistry, 1, 3

Aponte, J. C., Elsila, J. E., Hein, J. E., & Dworkin, J. P. 2020, Meteoritics & Planetary Science, 55, 2422

Askeland, E., Møllendal, H., Uggerud, E., et al. 2006, The Journal of Physical Chemistry A, 110, 12572

Baraban, J., Martin-Drumel, M. A., Changala, P. B., et al. 2018, Angewandte Chemie International Edition, 57, 1821

Becke, A. D. 1993, J. Chem. Phys., 98, 5648

Belloche, A., Garrod, R. T., Müller, H. S. P., et al. 2019, A&A, 628, A10

Belloche, A., Menten, K., Comito, C., et al. 2008, A&A, 492, 769

Benidar, A., Guillemin, J.-C., Mó, O., & Yáñez, M. 2005, Journal of Physical Chemistry A, 109, 4705

Bergin, E. A., Ciardi, D. R., Lada, C. J., Alves, J., & Lada, E. A. 2001, ApJ, 557, 209

Bizzocchi, L., Prudenzano, D., Rivilla, V. M., et al. 2020, A&A, 640, A98

Bockelée-Morvan, D., Lis, D. C., Wink, J. E., et al. 2000, A&A, 353, 1101

Bossa, J. B., Theule, P., Duvernay, F., & Chiavassa, T. 2009, ApJ, 707, 1524

Brearley, A. J. 2006, in Meteorites and the Early Solar System II, ed. D. S. Lauretta & H. Y. McSween (University of Arizona Press), 584

Brown, R. D., Godfrey, P. D., & Winkler, D. A. 1981, Chemical Physics, 59, 243

Burton, A. S., Stern, J. C., Elsila, J. E., Glavin, D. P., & Dworkin, J. P. 2012, Chem. Soc. Rev., 41, 5459

Cabezas, C., Agúndez, M., Marcelino, N., et al. 2021, A&A, 654, L9

Cazzoli, G., Puzzarini, C., & Lapinov, A. V. 2003, The Astrophysical Journal, 592, L95

Cernicharo, J., Agúndez, M., & Cabezas. 2021, A&A, 647, L2

Cernicharo, J., Cabezas, C., Endo, Y., et al. 2021, A&A, 650, L14

Cernicharo, J. 2012, EAS Publications Series, 58, 251

Chantzos, J. 2020, PhD thesis, Ludwig-Maximilians University of Munich, Germany

Charnley, S. 2002, in 34th COSPAR Scientific Assembly, Vol. 34, 667

Chuang, K. J., Fedoseev, G., Ioppolo, S., van Dishoeck, E. F., & Linnartz, H. 2016, MNRAS, 455, 1702

Chyba, C. & Sagan, C. 1992, Nature, 355, 125

Chyba, C. F., Thomas, P. J., Brookshaw, L., & Sagan, C. 1990, Science, 249, 366

Colzi, L., Martín-Pintado, J., Rivilla, V. M., et al. 2022, ApJ, 926, L22

Crapsi, A., Caselli, P., Walmsley, M. C., & Tafalla, M. 2007, A&A, 470, 221

Cuadrado, S., Goicoechea, J. R., Roncero, O., et al. 2016, A&A, 596, L1

Curl, R. F., Oka, T., & Smith, D. S. 1973, Journal of Molecular Spectroscopy, 46, 518

Danger, G., Bossa, J.-B., de Marcellus, P., et al. 2011, A&A, 525, A30

de Marcellus, P., Meinert, C., Nuevo, M., et al. 2011, ApJ, 727, L27

Dickens, J. E., Irvine, W. M., Nummelin, A., et al. 2001, Spectrochimica Acta Part A: Molecular Spectroscopy, 57, 643

Dore, L. 2003, Journal of Molecular Spectroscopy, 221, 93

Drabkin, V. D., Paczelt, V., & Eckhardt, A. K. 2023, Chem. Commun., 59, 12715

Drozdovskaya, M. N., van Dishoeck, E. F., Rubin, M., Jørgensen, J. K., & Altwegg, K. 2019, MNRAS, 490, 50

Dunham, M. M., Stutz, A. M., Allen, L. E., et al. 2014, in Protostars and Planets VI, ed. H. Beuther, R. S. Klessen, C. P. Dullemond, & T. Henning, 195–218

Endres, C. P., Schlemmer, S., Schilke, P., Stutzki, J., & Müller, H. S. P. 2016, Journal of Molecular Spectroscopy, 327, 95

Fedoseev, G., Cuppen, H. M., Ioppolo, S., Lamberts, T., & Linnartz, H. 2015, MNRAS, 448, 1288

Feller, D. 1992, Journal of Chemical Physics; (United States), 96, 8

Field, G. B., Goldsmith, D. W., & Habing, H. J. 1969, ApJ, 155, L149

Flammang, R., Van Haverbeke, Y., Laurent, S., et al. 1994, The Journal of Physical Chemistry, 98, 5801

Fortenberry, R. C. & Lee, T. J. 2022, in Vibrational Dynamics of Molecules, ed. J. M. Bowman (Singapore: World Scientific), 235–295

Frisch, A. et al. 2009, Wallingford, USA, 25p, 470

Frisch, M. J., Trucks, G. W., Schlegel, H. B., et al. 2016, Gaussian~16 Revision C.01, gaussian Inc. Wallingford CT

García de la Concepción, J., Jiménez-Serra, I., Carlos Corchado, J., Rivilla, V. M., & Martín-Pintado, J. 2021, ApJ, 912, L6

García-Sánchez, M., Jiménez-Serra, I., Puente-Sánchez, F., & Aguirre, J. 2022, Proceedings of the National Academy of Science, 119, e2119734119

Gardner, F. F.; Winnewisser, G. 1975, Astrophysical Journal, 195, L127

Gardner, J. P., Mather, J. C., Clampin, M., et al. 2006, Space Sci. Rev., 123, 485

Gardner, M. B., Westbrook, B. R., Fortenberry, R. C., & Lee, T. J. 2021, Spectrochim. Acta A, 248, 119184

Garrod, R. T. 2013, ApJ, 765, 60

Garrod, R. T. & Herbst, E. 2006, A&A, 457, 927

Garrod, R. T., Widicus Weaver, S. L., & Herbst, E. 2008, ApJ, 682, 283

Gaw, J. F., Willetts, A., Green, W. H., & Handy, N. C. 1991, Advances in molecular vibrations and collision dynamics, 1, 169

Gilbert, W. 1986, Nature, 319, 618

Glavin, D. P., Aubrey, A. D., Callahan, M. P., et al. 2010, Meteorit. Planet. Sci., 45, 1695

Godfrey, P., Brown, R., Robinson, B., & Sinclair, M. 1973, Astrophys. Lett., 13, 119

Godfrey, P. D., Brown, R. D., Robinson, B. J., & Sinclair, M. W. 1973, Astrophys. Lett., 13, 119

Gordy, W. & Cook, R. L. 1984, Microwave molecular spectra / Walter Gordy, Robert L. Cook, 3rd edn. (Wiley New York), xiv, 929 p. :

Guillemin, J.-C., Breneman, C. M., Joseph, J. C., & Ferris, J. P. 1998, Chem. Eur. J., 4, 1074

Güsten, R., Wiesemeyer, H., Neufeld, D., et al. 2019, Nature, 568, 357

Hagan, L. 1974, in Bulletin of the Astronomical Society, Vol. 6, p. 140-144, Vol. 6, 140–144

Heckert, M., Kállay, M., & Gauss, J. 2005, Molecular Physics, 103, 2109

Heckert, M., Kállay, M., Tew, D. P., Klopper, W., & Gauss, J. 2006, J. Chem. Phys., 125, 044108

Helgaker, T., Klopper, W., Koch, H., & Noga, J. 1997, J. Chem. Phys., 106, 9639

Herbst, E. & van Dishoeck, E. F. 2009, ARA&A, 47, 427

Hill, C. 2019, The Morse oscillator

Hill, J. G., Mazumder, S., & Peterson, K. A. 2010, J. Chem. Phys., 132, 054108

Hollis, J. M., Jewell, P. R., Lovas, F. J., & Remijan, A. 2004, ApJ, 613, L45

Hollis, J. M., Lovas, F. J., & Jewell, P. R. 2000, ApJ, 540, L107

Huss, G. R., Rubin, A. E., & Grossman, J. N. 2006, in Meteorites and the Early Solar System II, ed. D. S. Lauretta & H. Y. McSween (University of Arizona Press), 567

Inostroza, N., Fortenberry, R. C., Huang, X., & Lee, T. J. 2013, The Astrophysical Journal, 778, 160

Inostroza, N., Huang, X., & Lee, T. J. 2011, The Journal of Chemical Physics, 135, 244310

Ioppolo, S., Fedoseev, G., Chuang, K. J., et al. 2021, Nature Astronomy, 5, 197

IRAM. 2024, NOEMA, https://iram-institute.org/observatories/noema/

Jiang, N., Melosso, M., Bizzocchi, L., et al. 2022, The Journal of Physical Chemistry A, 126, 1881, pMID: 35275628

Jiang, N., Melosso, M., Tamassia, F., et al. 2021, Front. Astron. Space Sci., 8, 29

Jiménez-Serra, I., Martín-Pintado, J., Rivilla, V. M., et al. 2020, Astrobiology, 20, 1048

Jiménez-Serra, I., Rodríguez-Almeida, L. F., Martín-Pintado, J., et al. 2022a, A&A, 663, A181

Jiménez-Serra, I., Rodríguez-Almeida, L. F., Martín-Pintado, J., et al. 2022b, A&A, 663, A181

Jiménez-Serra, I., Martín-Pintado, J., Rivilla, V. M., et al. 2020, Astrobiology, 20, 1048, pMID: 32283036

Kaifu, N., Morimoto, M., Nagane, K., et al. 1974, ApJ, 191, L135

Kameneva, S. V., Tyurin, D. A., & Feldman, V. I. 2017, Physical Chemistry Chemical Physics (Incorporating Faraday Transactions), 19, 24348

Kitadai, N. & Maruyama, S. 2018, Geoscience Frontiers, 9, 1117

Knizia, G., Adler, T. B., & Werner, H.-J. 2009a, J. Chem. Phys., 130, 054104

Knizia, G., Adler, T. B., & Werner, H.-J. 2009b, J. Chem. Phys., 130, 054104

Koch, D. M., Toubin, C., Peslherbe, G. H., & Hynes, J. T. 2008, The Journal of Physical Chemistry C, 112, 2972

Krasnokutski, S. A. 2021, Low Temperature Physics, 47, 199

Krasnokutski, S. A., Chuang, K. J., Jäger, C., Ueberschaar, N., & Henning, T. 2022, Nature Astronomy, 6, 381

Krim, L., Guillemin, J.-C., & Woon, D. E. 2019, MNRAS, 485, 5210

Kroto, H. W. 1992, Molecular Rotation Spectra (Dover Pubblication)

Kutner, M. L. & Ulich, B. L. 1981, ApJ, 250, 341

Lada, C. J. 1987, in Star Forming Regions, ed. M. Peimbert & J. Jugaku, Vol. 115, 1

Lamb, W. E. 1964, Phys. Rev., 134, A1429

Lee, C., Yang, W., & Parr, R. G. 1988, Phys. Rev. B, 37, 785

Lee, K. L. K., Changala, P. B., Loomis, R. A., et al. 2021a, ApJ, 910, L2

Lee, K. L. K., Loomis, R. A., Burkhardt, A. M., et al. 2021b, ApJ, 908, L11

Loomis, R. A., Burkhardt, A. M., Shingledecker, C. N., et al. 2021, Nature Astronomy, 5, 188

Loomis, R. A., Zaleski, D. P., Steber, A. L., et al. 2013a, ApJ, 765, L9

Loomis, R. A., Zaleski, D. P., Steber, A. L., et al. 2013b, ApJ, 765, L9

Lovas, F. J., Hollis, J., Remijan, A. J., & Jewell, P. 2006, ApJL, 645, L137

Lovas, F. J., Hollis, J. M., Remijan, A. J., & Jewell, P. R. 2006, ApJ, 645, L137

Lupi, J., Puzzarini, C., & Barone, V. 2020, ApJ, 903, L35

Mangum, J. G. & Shirley, Y. L. 2015, PASP, 127, 266

Margulès, L., Motiyenko, R. A., Alekseev, E. A., & Demaison, J. 2010, Journal of Molecular Spectroscopy, 260, 23

Margulès, L., Remijan, A., Belloche, A., et al. 2022, A&A, 663, A132

Martín, S., Martín-Pintado, J., Blanco-Sánchez, C., et al. 2019a, A&A, 631, A159

Martín, S., Martín-Pintado, J., Blanco-Sánchez, C., et al. 2019b, A&A, 631, A159

Martín, S., Requena-Torres, M. A., Martín-Pintado, J., & Mauersberger, R. 2008, The Astrophysical Journal, 678, 245, arXiv: 0801.3614

Matthews, D. A., Cheng, L., Harding, M. E., et al. 2020, J. Chem. Phys., 152, 214108

McCarthy, M. C., Lee, K. L. K., Loomis, R. A., et al. 2021, Nature Astronomy, 5, 176

McGuire, B. A. 2022, The Astrophysical Journal Supplement Series, 259, 30

McGuire, B. A., Carroll, P. B., Loomis, R. A., et al. 2016, Science, 352, 1449

McGuire, B. A., Carroll, P. B., Loomis, R. A., et al. 2016, Science, 352, 1449

McGuire, B. A. & mcguiregroup. 2021, bmcguir2 astromol: Added n-methyl formamide detection

McKee, C. F. & Ostriker, J. P. 1977, ApJ, 218, 148

Melli, A., Melosso, M., Tasinato, N., et al. 2018, ApJ, 855, 123

Melli, A., Potenti, S., Melosso, M., et al. 2020, Chem. Eur. J., 26, 15016

Melosso, M., Achilli, A., Tamassia, F., et al. 2020a, J. Quant. Spectrosc. Ra., 248, 106982

Melosso, M., Bizzocchi, L., Tamassia, F., et al. 2019a, Phys. Chem. Chem. Phys., 21, 3564

Melosso, M., Conversazioni, B., Degli Esposti, C., et al. 2019b, J. Quant. Spectrosc. Ra., 222, 186

Melosso, M., Dore, L., Gauss, J., & Puzzarini, C. 2020b, J. Mol. Spectrosc., 111291

Melosso, M., Melli, A., Puzzarini, C., et al. 2018, A&A, 609, A121

Miller, S. L. 1953, Science, 117, 528

Miller, S. L. & Orgel, L. E. 1974, The origins of life on the earth (Englewood Cliffs, N.J., Prentice-Hall)

Mills, I. 1972a, in Molecular spectroscopy: modern research, ed. K. N. Rao & C. W. Matthews (Academic Press), 115–140

Mills, I. M. 1972b, in Molecular Spectroscopy - Modern Research, ed. K. N. Rao & C. W. Mathews (New York: Academic Press), 115–140

Møller, C. & Plesset, M. S. 1934, Phys. Rev., 46, 618

Møller, C. & Plesset, M. S. 1934, Physical Review, 46, 618

Müller, H. S. P., Schlöder, F., Stutzki, J., & Winnewisser, G. 2005, Journal of Molecular Structure, 742, 215

Neill, J. L., Muckle, M. T., Zaleski, D. P., et al. 2012, The Astrophysical Journal, 755, 153

Oba, Y., Takano, Y., Furukawa, Y., et al. 2022, Nature Communications, 13, 2008

Oparin, A. I. Synge, A. 1957, The Origin of Life on the Earth (Pergamon)

Papousek, D. & Aliev, M. R. 1982, Molecular Vibration-Rotation Spectra (Amsterdam: Elsevier)

Pardo, J. R., Cabezas, C., Fonfría, J. P., et al. 2021, A&A, 652, L13

Pardo, J. R., Cernicharo, J., & Serabyn, E. 2001, IEEE Transactions on Antennas and Propagation, 49, 1683

Pearce, B. K. D., Molaverdikhani, K., Pudritz, R. E., Henning, T., & Cerrillo, K. E. 2022, ApJ, 932, 9

Penn, R. E. 1978, Journal of Molecular Spectroscopy, 69, 373

Pickett, H. M. 1991, Journal of Molecular Spectroscopy, 148, 371

Pickett, H. M., Poynter, R. L., & Cohen, E. A. 1998, Journal of Quantitative Spectroscopy and Radiative Transfer, 60, 883

Piel, A. 2017, Plasma Physics: An Introduction to Laboratory, Space, and Fusion Plasmas (Springer)

Pietropolli Charmet, A. & Cornaton, Y. 2018, Journal of Molecular Structure, 1160, 455

Pineda, J. E., Segura-Cox, D., Caselli, P., et al. 2020, Nature Astronomy, 4, 1158

Pizzarello, S., Cooper, G. W., & Flynn, G. J. 2006, in Meteorites and the Early Solar System II, ed. D. S. Lauretta & H. Y. McSween (University of Arizona Press), 625

Pizzarello, S. & Groy, T. L. 2011, Geochimica et Cosmochimica Acta, 75, 645

Prudenzano, D. 2020, PhD thesis, Ludwig-Maximilians University of Munich, Germany

Puzzarini, C. 2022, Frontiers in Astronomy and Space Sciences, 8, 811342

Puzzarini, C. & Barone, V. 2020, Phys. Chem. Chem. Phys., 22, 6507

Puzzarini, C., Cazzoli, G., Harding, M. E., Vázquez, J., & Gauss, J. 2009, J. Chem. Phys., 131, 234304

Puzzarini, C. & Stanton, J. F. 2023, Physical Chemistry Chemical Physics (Incorporating Faraday Transactions), 25, 1421

Puzzarini, C., Stanton, J. F., & Gauss, J. 2010, International Reviews in Physical Chemistry, 29, 273

Raghavachari, K., Trucks, G. W., Pople, J. A., & Head-Gordon, M. 2013, Chemical Physics Letters, 589, 37

Rauhut, G., Knizia, G., & Werner, H.-J. 2009, J. Chem. Phys., 130, 054105

Ray, B. S. 1932, Zeitschrift fur Physik, 78, 74

Redaelli, E. 2020, PhD thesis, Ludwig-Maximilians University of Munich, Germany

Redondo, P., Largo, A., & Barrientos, C. 2018, MNRAS, 478, 3042

Requena-Torres, M. A., Martín-Pintado, J., Martín, S., & Morris, M. R. 2008, The Astrophysical Journal, 672, 352, arXiv: 0709.0542

Requena-Torres, M. A., Martín-Pintado, J., Rodríguez-Franco, A., et al. 2006, Astronomy & Astrophysics, 455, 971, arXiv: astro-ph/0605031

Rimola, A., Sodupe, M., & Ugliengo, P. 2010, Physical Chemistry Chemical Physics, 12, 5285

Rivilla, V., Martín-Pintado, J., Jiménez-Serra, I., et al. 2019, MNRAS Lett., 483, L114

Rivilla, V. M., Colzi, L., Jiménez-Serra, I., et al. 2022a, ApJ, 929, L11

Rivilla, V. M., Drozdovskaya, M. N., Altwegg, K., et al. 2020a, MNRAS, 492, 1180

Rivilla, V. M., García De La Concepción, J., Jiménez-Serra, I., et al. 2022b, Frontiers in Astronomy and Space Sciences, 9, 829288

Rivilla, V. M., Jiménez-Serra, I., García de la Concepción, J., et al. 2021a, MNRAS, 506, L79

Rivilla, V. M., Jiménez-Serra, I., García de la Concepción, J., et al. 2021b, MNRAS, 506, L79

Rivilla, V. M., Jiménez-Serra, I., Martín-Pintado, J., et al. 2021c, Proceedings of the National Academy of Science, 118, 2101314118

Rivilla, V. M., Jiménez-Serra, I., Martín-Pintado, J., et al. 2022c, Frontiers in Astronomy and Space Sciences, 9, 876870

Rivilla, V. M., Jiménez-Serra, I., Martín-Pintado, J., et al. 2022d, Frontiers in Astronomy and Space Sciences, 9, 876870

Rivilla, V. M., Martín-Pintado, J., Jiménez-Serra, I., et al. 2020b, ApJ, 899, L28

Rivilla, V. M., Sanz-Novo, M., Jiménez-Serra, I., et al. 2023, ApJ, 953, L20

Robitaille, T. P. & Whitney, B. A. 2010, ApJ, 710, L11

Robitaille, T. P., Whitney, B. A., Indebetouw, R., Wood, K., & Denzmore, P. 2006, ApJS, 167, 256

Rodríguez-Almeida, L. F., Jiménez-Serra, I., Rivilla, V. M., et al. 2021a, ApJ, 912, L11

Rodríguez-Almeida, L. F., Jiménez-Serra, I., Rivilla, V. M., et al. 2021a, ApJ, 912, L11

Rodríguez-Almeida, L. F., Rivilla, V. M., Jiménez-Serra, I., et al. 2021b, A&A, 654, L1

Rodríguez-Almeida, L. F., Rivilla, V. M., Jiménez-Serra, I., et al. 2021b, A&A, 654, L1

Rose, M. E. 1957, Elementary Theory of Angular Momentum (Dover Publications Inc.)

Ruaud, M., Loison, J. C., Hickson, K. M., et al. 2015, MNRAS, 447, 4004

Sanchez, R. A., Ferris, J. P., & Orgel, L. E. 1966, Science, 154, 784

Sanz-Novo, M., Belloche, A., Rivilla, V. M., et al. 2022, arXiv e-prints, arXiv:2203.07334

Shingledecker, C. N., Lee, K. L. K., Wandishin, J. T., et al. 2021, A&A, 652, L12

Shingledecker, C. N., Molpeceres, G., Rivilla, V. M., Majumdar, L., & Kästner, J. 2020, ApJ, 897, 158

Snyder, L. E., Lovas, F. J., Hollis, J. M., et al. 2005, ApJ, 619, 914

Stahler, S. W. & Palla, F. 2004, The Formation of Stars (John Wiley & Sons, 2008)

Stoks, P. G. & Schwartz, A. W. 1979, Nature, 282, 709

Suzuki, T., Majumdar, L., Ohishi, M., et al. 2018, ApJ, 863, 51

Tanaka, K., Oka, T., Matsumura, S., Nagai, M., & Kamegai, K. 2011, ApJ, 743, L39

Theule, P., Borget, F., Mispelaer, F., et al. 2011, A&A, 534, A64

Tielens, A. 2021, Molecular Astrophysics (Cambridge University Press)

Townes, C. H. & Schawlow, A. L. 1975, Microwave spectroscopy (Dover Publications, New York)

Tüllmann, R., Gaetz, T. J., Plucinsky, P. P., et al. 2008, ApJ, 685, 919

Turner, B. E. 1971, ApJ, 163, L35

Vastel, C., Bottinelli, S., Caux, E., et al. 2015, SF2A-2015: Proceedings of the Annual meeting of the French Society of Astronomy and Astrophysics

Vazart, F., Latouche, C., Skouteris, D., Balucani, N., & Barone, V. 2015, ApJ, 810, 111

Wakelam, V., Loison, J. C., Hickson, K. M., & Ruaud, M. 2015, MNRAS, 453, L48

Walch, S. P., Bauschlicher, C. W., Ricca, A., & Bakes, E. L. O. 2001, Chemical Physics Letters, 333, 1524

Watrous, A. G., Westbrook, B. R., & Fortenberry, R. C. 2022, J. Phys. Chem. A, 125, 10532

Watson, J. K. G. 1967, J Chem. Phys., 46

Watson, J. K. G. 1971, Journal of Molecular Spectroscopy, 40, 536

Watson, J. K. G. 1977, in Vibrational Spectra and Structure, ed. J. Durig, Vol. 6 (Elsevier, Amsterdam), 1–89

Watson, J. K. G. 1978a, Journal of Molecular Structure, 44, 263

Watson, J. K. G. 1978b, Journal of Molecular Structure, 44, 263

Werner, H., Knowles, P., Knizia, G., et al. 2015, University of Cardiff Chemistry Consultants (UC3): Cardiff, Wales, UK

Werner, H.-J., Knowles, P. J., Manby, F. R., et al. 2020, J. Chem. Phys., 152, 144107

Westbrook, B. R. & Fortenberry, R. C. 2023, J. Chem. Theory Comput., 19, 2606

Winton, R. & Gordy, W. 1970, Physics Letters A, 32, 219

Woon, D. E. 2002, ApJ, 571, L177

Woon, D. E. & Dunning, Thom H., J. 1995, J. Chem. Phys., 103, 4572

Xiang, Y.-B., Drenkard, S., Baumann, K., Hickey, D., & Eschenmoser, A. 1994, Hel. Chim. Acta, 77, 2209

Yamada, K. & Winnewisser, M. 1975, Zeitschrift Naturforschung Teil A

Yamamoto, S. 2017, Introduction to Astrochemistry: Chemical Evolution from Interstellar Clouds to Star and Planet Formation (Springer Tokyo)

Zaleski, D. P., Seifert, N. A., Steber, A. L., et al. 2013, ApJ, 765, L10

Zaleski, D. P., Seifert, N. A., Steber, A. L., et al. 2013a, The Astrophysical Journal Letters, 765, L10

Zaleski, D. P., Seifert, N. A., Steber, A. L., et al. 2013b, ApJL, 765, L10

Zeng, S., Jiménez-Serra, I., Rivilla, V. M., et al. 2018, MNRAS, 478, 2962

Zeng, S., Jiménez-Serra, I., Rivilla, V. M., et al. 2021, ApJ, 920, L27

Zeng, S., Jiménez-Serra, I., Rivilla, V. M., et al. 2018, Monthly Notices of the Royal Astronomical Society, 478, 2962

Zeng, S., Quénard, D., Jiménez-Serra, I., et al. 2019, MNRAS: Letters, 484, L43

Zeng, S., Zhang, Q., Jiménez-Serra, I., et al. 2020a, MNRAS, 497, 4896

Zeng, S., Zhang, Q., Jiménez-Serra, I., et al. 2020b, MNRAS, 497, 4896

Öberg, K. I., Guzmán, V. V., Furuya, K., et al. 2015, Nature, 520, 198–201

Acknowledgements

In these final lines, I would like to express my gratitude to all those who have contributed to making this trip unforgettable, and to thank those who will surely be forgotten due to my poor memory.

I would like to start with the members of the CAS group, all of you, for giving me the opportunity to learn what I did not know, for stimulating me with the Journal Clubs and Group Meetings, for cheering me up between lunches and making me laugh with your jokes. Among others, I would like to thank Paola for giving me the opportunity to spend this time here and for always being patient with my disorganisation; the others will follow in no particular order because there is too much to say. I would like to thank Cote, Elena, Felipe, my office mate Katha, Michela, Judit, Farideh, Angie and all those whose names would take too long to list. Thanks to the whole CAS group.

I must also thank all the scientists I have had the opportunity to work with. Among them, I owe a special thanks to Ryan and Natalia for the experiences I had with them and for being such wonderful people.

I owe a special thanks to the one who welcomed me, took me in when it was not his responsibility, guided me between manometers and BNC cables, and proved to be not only the one who guided my scientific progress, but also a friend. Vale, I was lucky to have met you.

I must also thank those I met in Garching, but who have become my Munich friends: Tien, Joaquin, Jay, Simon, Fran and Laz. Life takes us in different directions, but I hope this bond will never fade. I have shared some wonderful moments with you.

I also owe a special thanks to my private banker and friend, Ale. I hope your knee gets better soon! I'll wait for you by the pool. And of course Anirudth, for coffee, biscuits and his sincere friendship.

I also have to thank the one who, without being physically close to me, was always there for me in my soul or behind the phone screen, with whom I lived through four years of a sometimes painful but always joyful long-distance relationship, a shoulder to lean on. It was not only love that kept us together, it was also the will, and yours proved to be stronger than mine. I am lucky to have you, Silvia.

Finally, I must thank my family for standing by me when I should have been the one to do it for you. I don't know what to write here, and maybe it's better if I don't. I will pick up the phone and call you, because it's the best way to express my gratitude. Or even better, I'll come and see you this weekend! And with you, Silvia.